université PARIS-SACLAY

école normale supérieure paris-saclay

NNT : 2019SACLN017

Thèse de doctorat

On the use of isogeometric analysis in linear or nonlinear structural mechanics: certification of the simulations and coupling with PGD model reduction

Thèse de doctorat de l'Université Paris-Saclay
préparée à l'Ecole normale supérieure de Paris-Saclay

Ecole doctorale n°579 sciences mécaniques et énergétiques, matériaux et géosciences (SMEMAG)
Spécialité de doctorat : génie mécanique

Thèse présentée et soutenue à Cachan, le 17/06/2019, par

HOANG PHUONG THAI

Composition du Jury :

M. Eric FLORENTIN Professeur INSA Centre Val de Loire	Rapporteur
M. Gianluigi ROZZA Professeur SISSA, International School for Advanced Studies	Rapporteur
M. Robin BOUCLIER Maître de Conférences INSA Toulouse	Examinateur
M. Martin VOHRALIK Directeur de Recherche INRIA Paris	President
Mme Bing TIE Chargée de Recherche CNRS	Examinateur
M. Ludovic CHAMOIN Professeur ENS Paris-Saclay	Directeur de thèse
M. Cuong HA MINH Maître de Conférences ENS Paris-Saclay	Co-directeur de thèse

Titre : Sur l'utilisation de l'analyse isogéométrique en mécanique linéaire ou non-linéaire des structures : certification des calculs et couplage avec la réduction de modèle PGD

Mots clés : analyse isogeométrique, vérification des modèles, réduction de modèle

Résumé : Le sujet de la thèse porte sur la mise en place d'approches numériques avancées pour la simulation et l'optimisation de structures mécaniques présentant une géométrie complexe. Il se focalise sur l'analyse isogéométrique (IGA) qui a reçu beaucoup d'intérêt cette dernière décennie dû à sa grande flexibilité, précision, et robustesse dans de nombreux contextes industriels en comparaison avec à la méthode des éléments finis (FEA) classique.
La première partie du travail aborde la construction d'une méthode de vérification basée sur la dualité et le concept d'erreur en relation de comportement (ERC). Il permet d'obtenir des estimateurs d'erreur a posteriori à la fois garantis et entièrement calculables pour les solutions numériques issues de simulation par IGA. Un intérêt particulier est porté sur la construction de champs équilibrés, qui est un point clé du concept ERC, et qui jusqu'à présent était essentiellement développé dans le cadre de la méthode des éléments finis. Le concept ERC est aussi mis en oeuvre avec les techniques d'adjoint pour faire de l'estimation d'erreur sur des quantités d'intérêt.
Dans une seconde partie du travail, la technologie IGA est couplée avec une procédure de réduction de modèle pour obtenir des solutions certifiées, et en temps réel, de problèmes avec une géométrie paramétrée. Après avoir défini le paramétrage sur la transformation permettant de passer de l'espace paramétrique IGA à l'espace physique, un modèle réduit basé sur la technique PGD (Proper Generalized Decomposition) est introduit pour résoudre le problème multi-dimensionnel. L'estimation a posteriori des diverses sources d'erreur venant de la discrétisation et de la réduction de modèle PGD est menée à partir du concept ERC. Cela permet de contrôler la qualité de la solution PGD approchée (globalement ou sur des quantités d'intérêt), pour toute configuration géométrique, et de nourrir un algorithme adaptatif qui optimise l'effort de calcul pour une tolérance d'erreur donnée. Les performances des divers outils mis en place pendant la thèse sont analysées à travers différentes expériences numériques, et dans le cadre de problèmes linéaires ou non-linéaires.

Title : On the use of isogeometric analysis in linear or nonlinear structural mechanics : certification of the simulations and coupling with PGD model reduction

Keywords : isogeometric analysis, model verification, model reduction

Abstract : The topic of the PhD thesis deals with the construction of advanced numerical approaches for the simulation and optimization of mechanical structures with complex geometry. The PhD thesis focuses on the Isogeometric Analysis (IGA) technology that received a large interest during the last decade due to its increased flexibility, accuracy, and robustness in many engineering simulations compared to classical Finite Element Analysis (FEA).
The first part of the work addresses the construction of a verification method based on duality and the concept of Constitutive Relation Error (CRE). The focus here is on the construction of equilibrated flux fields, which is key ingredient of the CRE concept, and which was until now almost exclusively developed in the FEA framework alone. The CRE concept is also implemented together with adjoint techniques in order to perform goal-oriented error estimation.
In a second part, IGA is coupled with model reduction in order to get certified real-time solutions to problems with parameterized geometry. After defining the parametrization on the mapping from the IGA parametric space to the physical space, a reduced model based on the Proper Generalized Decomposition (PGD) is introduced to solve the multi-dimensional problem. A posteriori estimation of the various error sources inheriting from discretization and PGD model reduction is performed from the CRE concept. It enables to control the quality of the approximate PGD solution (globally or on outputs of interest), for any geometry configuration, and to feed a robust greedy algorithm that optimizes the computational effort for a prescribed error tolerance. Performances of the various tools which were elaborated during the PhD are analyzed on several numerical experiments, and in the framework of linear or nonlinear problems.

Université Paris-Saclay
Espace Technologique / Immeuble Discovery
Route de l'Orme aux Merisiers RD 128 / 91190 Saint-Aubin, France

Contents

Table of contents vi

1 Introduction 1

1.1 Motivation . . . 1
1.2 IGA computational framework for complex geometries . . . 3
1.2.1 Introduction of IGA . . . 3
1.2.2 Controlling the quality of IGA by error estimation . . . 4
1.2.3 Advantages of using IGA in shape optimization . . . 5
1.3 Coupling model reduction and IGA . . . 5
1.4 Outline . . . 7

2 Bibliography 9

2.1 Isogeometric Analysis (IGA): A state-of-the-art . . . 9
2.1.1 Applications of IGA . . . 11
2.1.2 Drawbacks and challenges of IGA . . . 19
2.2 Up-to-date error estimation techniques for IGA . . . 20
2.2.1 Error estimation based on equilibrium residuals for IGA . . . 21
2.2.2 Error estimation based on based on a smoothing of the stresses for IGA . . . 24
2.2.3 Proposing error estimation based on the concept of error in constitutive relation for IGA . . . 29
2.3 Reduced order modelling for parametrized geometry . . . 30
2.3.1 IGA-based reduced order modelling . . . 30
2.3.2 PGD for parametrized geometry . . . 31

3 Fundamentals of IGA **33**
3.1 B-spline . . . 34
3.1.1 Knot vector . . . 34
3.1.2 B-spline basis functions . . . 35
3.1.3 B-spline geometry . . . 40
3.1.4 Non-Uniform Rational B-spline . . . 44
3.2 B-spline refinement . . . 46
3.2.1 Knot insertion . . . 48
3.2.2 Order elevation . . . 51
3.2.3 k-refinement . . . 53
3.3 The IGA framework . . . 53
3.3.1 Model problem . . . 53
3.3.2 IGA code architecture . . . 57
3.3.3 Similarities and differences between IGA and FEA . . . 58
3.4 Mapping in IGA . . . 58
3.4.1 Index space . . . 60
3.4.2 Parametric space . . . 60
3.4.3 Physical space . . . 61
3.4.4 Control mesh . . . 62

4 Error estimation in the IGA using the concept of CRE for linear mechanics problems **63**
4.1 Introduction of the CRE concept . . . 64
4.1.1 Definition of CRE . . . 64
4.1.2 CRE properties . . . 66
4.1.3 Goal-oriented error estimation . . . 67
4.2 Construction of an admissible flux field . . . 69
4.2.1 General hybrid-flux technique . . . 69
4.2.2 Technical implementation on a 2D example . . . 72
4.3 Numerical examples . . . 78
4.3.1 Example 1: thermal problem on a quarter of an annulus . . . 78
4.3.2 Example 2: elasticity problem on a L-shape domain . . . 89
4.3.3 Example 3: elasticity problem on a 3D structure . . . 92
4.4 Conclusion . . . 94

5 Coupling PGD with IGA **95**
5.1 Introduction . . . 95

5.2 Parametrized IGA formulation . . . 98
5.2.1 Model problem with parametrized geometry . . . 98
5.2.2 IGA formulation . . . 98
5.2.3 Parametrized mapping . . . 100
5.3 PGD model reduction: computation and post-processing . . . 101
5.3.1 Approximate PGD solution . . . 101
5.3.2 Post-processing of the PGD solution . . . 104
5.4 Error estimation and adaptive process . . . 105
5.4.1 Recovery of equilibrated fields . . . 106
5.4.2 Adaptive algorithm . . . 107
5.5 Numerical results . . . 110
5.5.1 Computation of the torsion stiffness of a parametrized NACA profile 110
5.5.2 Parametrized 3D geometry . . . 117
5.6 Conclusion . . . 119

6 Extension to damage phenomena inside structures with parametrized geometry 121
6.1 Introduction . . . 121
6.2 CRE functional for nonlinear material behaviors . . . 122
6.3 CRE for damage problems . . . 125
6.3.1 Example : damage problem on a plate with circular hole . . . 127
6.4 Parametrized reference model with damage behavior . . . 128
6.4.1 The model problem . . . 128
6.5 Procedure for reference model with damage behaviour . . . 130
6.5.1 Step 1: non-damage stage . . . 130
6.5.2 Step 2: Newton method . . . 130
6.5.3 Example : nonlinear problem on a plate with circular hole using PGD . . . 131

7 Conclusions and prospects 135
7.1 General conclusions . . . 135
7.2 Prospects . . . 136

Bibliography 138

Chapter 1

Introduction

Contents

1.1 Motivation **1**
1.2 IGA computational framework for complex geometries . . . **3**
1.2.1 Introduction of IGA 3
1.2.2 Controlling the quality of IGA by error estimation 4
1.2.3 Advantages of using IGA in shape optimization 5
1.3 Coupling model reduction and IGA **5**
1.4 Outline **7**

1.1 Motivation

In order to explain physical situations and provide reliable tools for computer-aided design-analysis, numerical simulations have an important role in science and engineering. In particular, the continuous improvement of computer power in recent years has supported a growing interest in numerical simulations with more and more complex geometries. It is well-known that the more complex geometries are now created by Computer Aided Design (CAD) software as a standard throughout the industry. As an illustration, Figure 1.1 illustrates the results of shape optimization of a wheel rim using the MSC Nastran software. In this example, numerous parameters control the shape of the wheel rim such as the internal and external diameters, the thickness of the rim, spoke, hub, etc. Even though the simulation and optimization of such a part is feasible with classical numerical tools, the calculation process from the initial geometry to the optimized geometry is very time-consuming. A numerical solution is indeed needed for

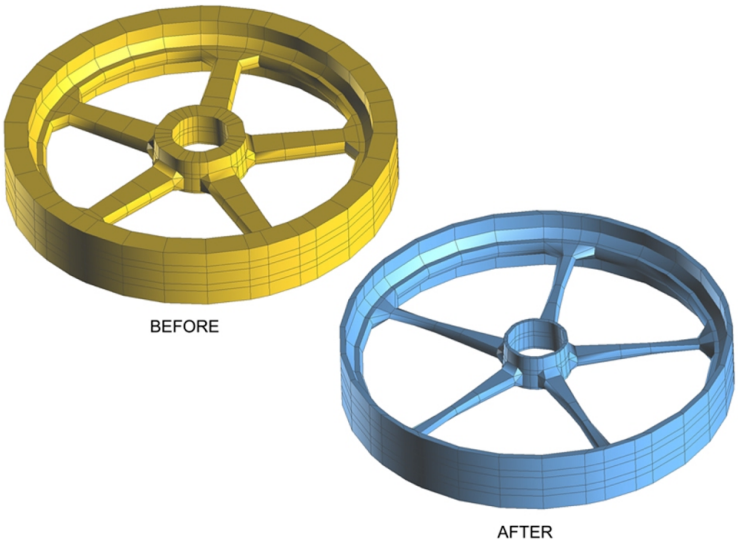

Figure 1.1: Shape optimization of a wheel rim.

each choice of parameters and it affects the computing time. Furthermore, meshing complex structures is a very time-consuming process that can be much longer than the analysis itself. The main challenge here is to design a suitable computational framework for complex geometries. This framework should have ability to perform analysis on complex CAD geometries with reduced meshing time.

Performing analysis on complex CAD geometries is difficult because there is a gap between the Finite Element Analysis (FEA) geometry and CAD geometry. According to Figure 1.2, the same geometry representation is produced by two different mathematical functions. The gap between FEA and CAD comes from the difference in initial aims. FEA was developed from the 1940s to improve engineering analyses, while CAD was applied to increase the productivity of design around the mid-1970s. Due to this difference, the traditional FEA softwares need to approximate the problem geometry by meshing to simulate the problem. Facing this issue, a computational framework that can overcome this gap was introduced in [HCB05, BBDVC+06, CHB09] and denoted as Isogeometric Analysis (IGA). IGA operates the B-spline or Non-uniform rational B-spline (NURBS) [PT95, DB01] functions as the basis to build CAD geometry and compute the approximate solution.

In the present work, we wish to develop IGA as a useful and practical numerical simulation tool for robust shape optimization in problems with complex geometries. To achieve the development, some issues need to be overcome. From a mathematical and

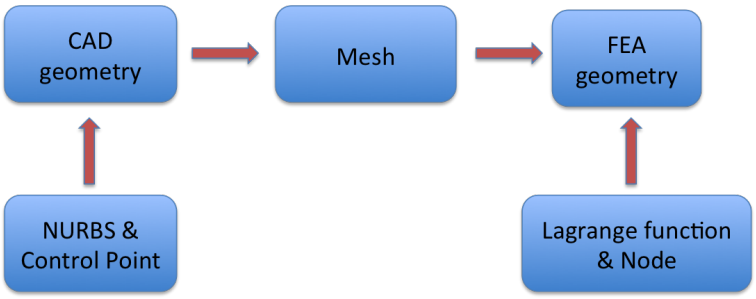

Figure 1.2: Relationship between CAD geometry and FEM geometry. CAD geometry uses NURBS functions and control points while FEM geometry uses Lagrange functions and nodes to represent the same shape.

robustness point of view, a key issue is controlling the quality of the IGA approximation solution by means of error estimation. From a practical point of view, the IGA approach needs to efficiently determine the solution for any value of the design variables. Indeed, despite the continuous progress in computer speeds and hardware capabilities, optimization problems may remain intractable using brute force approaches because of the curse of dimensionality. We choose here to use model reduction as an attractive and advanced numerical approach to deal with this issue.

1.2 IGA computational framework for complex geometries

1.2.1 Introduction of IGA

The key idea of IGA is displayed in Figure 1.3. The main idea is to use NURBS as basis functions in both design and in analysis. It aims at reducing the time for generating the mesh of designed geometry for analysis, by directly employing the CAD representation in the analysis step. The NURBS basis functions have numerous different features compared with Lagrange basis functions which are used in FEM [BS01].

IGA with exact representation of the geometry may be crucial in numerical simulations, as for shell structures which can be very sensitive to imperfections in the geometry. IGA provides very simple mesh refinement by eliminating the need for communication with the CAD geometry. Furthermore, NURBS basis functions possess a higher degree of continuity, so that the computation of stresses can be vastly improved. IGA has received much attention over the last decade in both research and industry and was successfully employed in many contexts [BCHZ08, EBCH08, BBHH10, GJS+12, KBLW09, BEC15, CRBH06] including shape optimization [WFC08, LQ11, FSV15]

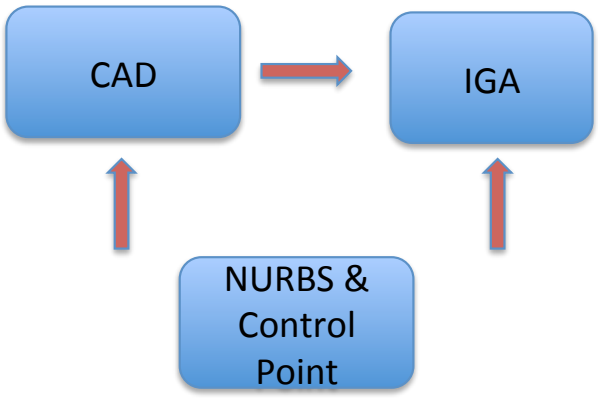

Figure 1.3: The idea of Isogeometric Analysis. NURBS functions are used as the basis to build CAD geometry and IGA approximation.

1.2.2 Controlling the quality of IGA by error estimation

Similarly to traditional numerical methods of many engineering problems in solid mechanics, IGA is associated with discretization error. A better approximate solution can be obtained using a finer mesh. Nevertheless, the computation cost and time will rise exponentially to create the new mesh and solve with an increased number of degrees of freedom. Therefore, the proper mesh for a numerical model should be chosen based on the computational cost and the simulation accuracy. This reason leads to a verification step for controlling the quality of the approximation by a posteriori error estimation. In contrast to the wide literature available for FEA, very few a posteriori error estimates are currently available for IGA. The reliability and efficiency of the proposed approaches often depend on undetermined constants, which is not suitable for quantitative assessment purposes.

In the present work, we develop a robust, guaranteed, and fully computable (i.e. with no unknown constants) *a posteriori* error estimate for IGA computations. For that purpose, we propose to use the Constitutive Relation Error (CRE) concept which has been extensively employed for FEA over the last 40 years (see [LP05, LC15] for an overview). It provides for a general framework that enables to obtain such robust, guaranteed, accurate, and fully computable error bounds. In particular, and compared to the approach proposed in [KT15], it can be applied with irregular meshes, geometries, or solutions, still providing with accurate local estimates for mesh adaptation and avoiding large overestimations. Furthermore, a suitable advantage of this concept is that it naturally extends to nonlinear evolution problems such as viscoplasticity, contact, or damage,

using thermodynamical considerations and convexity properties [LMD99, Lad01]. In addition, it can be used for goal-oriented error estimation when employed in conjunction with classical adjoint techniques [CL07, Lad08, WCLZ16]. The CRE concept is based on duality and requires to recover fully equilibrated fields as all error estimation techniques providing for guaranteed and computable bounds [DM99, MMP00, Zie01, BPS09, AM17]. Hence, this thesis applies CRE as a principal tool for a posteriori error estimation in the IGA framework in order to certify computations and to ensure robustness and reliability of the numerical simulation.

1.2.3 Advantages of using IGA in shape optimization

In general, the process of shape optimization consists of three modules: geometrical representation, structural analysis, and optimization algorithm. In the IGA context, the parametrization of the geometry may be naturally implemented using a parametrized mapping from the IGA parametric space to the physical space with design variables associated to coordinates of control points. This mapping, which is defined as a function of a finite number of parameters, is therefore simplified compared to the FEA context in which alternative techniques have been investigated in order to address evolving geometries [Can07, NCS11, NP18]. Here, the admissible shapes are taken to be images of a fixed reference shape under a smooth, invertible mapping using IGA functions. The state equations are then mapped back to the reference domain and become parameter-dependent PDEs on a fixed domain. Consequently, difficulties related to geometric variability are removed, and time-consuming re-meshing procedures are avoided. The geometry changes when the control points (red points in Figure 1.4) move.

In the traditional shape optimization using FEA, there are two different geometric models: the CAD model and the FEA model. Two different approaches for shape optimization have thus been developed: the CAD-based methods and the FE-based methods. CAD-based methods have a huge problem in meshing. On the other hand, FE-based shape optimization can lead to very irregular shapes. With automatic meshing and smooth geometry variations, IGA shape optimization can eliminate these disadvantages.

1.3 Coupling model reduction and IGA

Model reduction is an attractive and advanced numerical approach that has been widely developed during the last decade [CHRW17]. When dealing with a parametrized geometry, several works using IGA already introduced model reduction techniques [MSH15, ZDQ17]. They are mainly based on POD [CKL14] or reduced basis approaches [LR10,

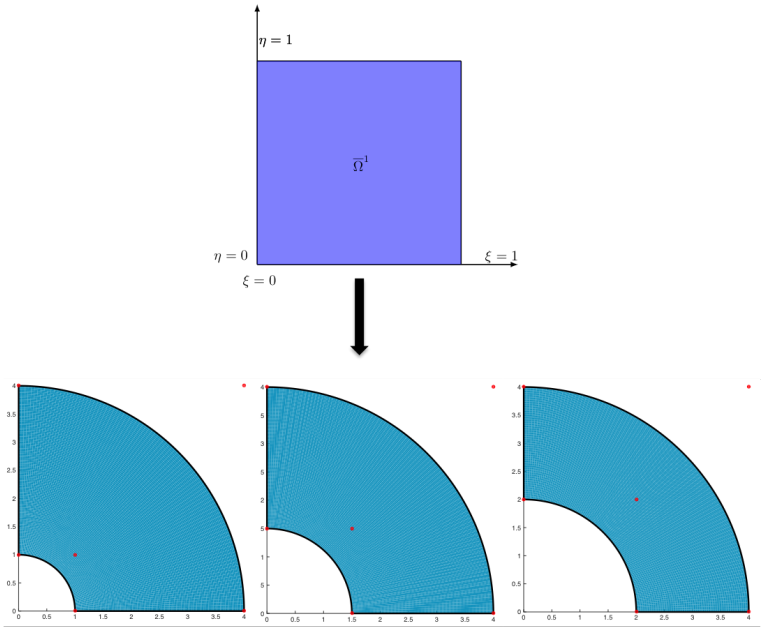

Figure 1.4: Parametric and physical space with control points.

Boy08]. The Proper Generalized Decomposition (PGD) [CL14, AMCK06] technique has not been applied yet with IGA. Nevertheless, the PGD technique was successfully implemented for many applications with parametric analyses, including parametrized geometry [ZDMH15, AHC+14, SZD17, CNLB16]. PGD addresses the geometry parameters as new coordinates of the model. Consequently, the results for all geometries can be easily handled. Together with the exactness of the geometrical representation, we believe that the use of IGA may be significantly beneficial for PGD both in terms of accuracy and efficiency.

PGD operates in an iterative strategy in which a representation of the solution is defined as a linear combination of separated variables functions (called modes), after defining all model parameters as extra-coordinates of the problem. Modes are computed on the fly in an *offline* step, by solving eigenvalue problems and without any knowledge on the solution (snapshot) compared to POD. An approximate solution of the model can then be obtained for any value of the parameters and be used in an *online* phase, with cheap and fast computations on light computing platforms, in order to perform real-time parametric or sensitivity analysis for optimization, inverse identification, or optimal control purposes. Here, we go one step further by coupling PGD with IGA. PGD extra-coordinates are then related to the coordinates and weights of control points

(at the coarsest mesh level, see Figure 1.4), and separation of variables is introduced between space and geometry variables. This enables to obtain virtual charts for shape optimization, with explicit and continuous dependency of the solution to design variables. Shape sensitivities can also be performed in a straightforward manner, without resorting to classical adjoint state methods [LT03].

1.4 Outline

To sum up, the thesis answers three essential tasks that are connected with the IGA framework.

- Constructing robust a posteriori error estimation for IGA using the concept of CRE.
- Computing solution of problems with parametrized geometry in 2D and 3D problems using PGD and certified model reduction-based IGA.
- Extending the two previous tasks to nonlinear structural mechanics problems.

The thesis is organized as follows:

1. In Chapter 2, the bibliography part introduces IGA and a state-of-art on methods involved with IGA to determine the research direction of this thesis. On the one hand, the description of the current a posteriori estimation methods for IGA are presented to highlight the drawbacks of these methods. On the other hand, ROM applications for IGA are presented, in particular those based on POD and reduced bases which are common in current research studies and applications.
2. In Chapter 3, the main aspects of the IGA framework are recalled. First, the properties of B-splines and NURBS are presented to explain the attractive features of IGA. Next, we specify the considered model problems to detail the IGA framework in its matrix form.
3. In Chapter 4, we focus on operating CRE for IGA. The procedure and the main features of CRE are illustrated. Due to the properties of IGA shape functions, the difficulties of applying CRE for IGA are highlighted. Technical details for the extension of the CRE concept to IGA are described for 2D and 3D problems in this chapter. Next, several examples with heat, elasticity and damage problems are considered to show how the proposed CRE error estimate performs with IGA in general mechanical problems. Eventually, mesh refinement and goal-oriented error estimation are addressed.

4. In Chapter 5, the coupling between IGA and PGD for parametrized geometry is presented. In a first part the PGD framework is introduced, then the IGA-PGD coupling is defined. The separation of geometry parameters and space coordinates is a key point in this coupling. It allows to control the geometry by means of control points instead of the mesh as in conventional numerical methods. Moreover, this feature allows to decrease the computational complexity as only the coarsest geometry level is considered in the parameter separation step. In addition, error estimation for the IGA-PGD coupling is developed.

5. In Chapter 6, we extend the IGA-PGD coupling for nonlinear damage problems which constitute a major engineering application. We first perform the separation of damage, geometry, and space coordinates, and we apply this separation in the PGD framework together with a Newton-Raphson method to compute the parametrized solution.

6. In Chapter 7, we summarize the works and discuss some further applications and prospects of the overall approach proposed in the thesis.

Chapter 2

Bibliography

Contents

2.1 Isogeometric Analysis (IGA): A state-of-the-art 9

2.1.1 Applications of IGA 11

2.1.2 Drawbacks and challenges of IGA 19

2.2 Up-to-date error estimation techniques for IGA 20

2.2.1 Error estimation based on equilibrium residuals for IGA . . . 21

2.2.2 Error estimation based on based on a smoothing of the stresses for IGA 24

2.2.3 Proposing error estimation based on the concept of error in constitutive relation for IGA 29

2.3 Reduced order modelling for parametrized geometry 30

2.3.1 IGA-based reduced order modelling 30

2.3.2 PGD for parametrized geometry 31

2.1 Isogeometric Analysis (IGA): A state-of-the-art

The section describes a global state-of-the-art on the Isogeometric Analysis (IGA) technology with its applications and actual challenges in computational engineering in order to clarify the objective of this thesis. This technology has received much attention over the last decade due to its increased flexibility, accuracy, and robustness in many engineering simulations compared to classical FEA.

Focusing on structural mechanics applications, the finite element method has been widely used as a classical framework to address such simulations, leading to the so-called

FEA. However, a major drawback and practical issue of FEA is that it intrinsically suffers from a complex link with Computer-Aided-Design (CAD) softwares which are employed to generate and design the geometry of mechanical structures. On the one hand, the geometry representation which is involved in FEA is based on piece-wise low-order polynomial functions (i.e. Lagrange polynomials, supported by polygonal meshes); it is dictated by the finite dimensional subspace considered to compute an approximate solution of the problem. On the other hand, the exact structural geometry generated by CAD is classically built from splines or NURBS functions which are smooth functions that enable to represent complex objects. Due to this difference in the geometry representation, the transfer from a CAD model to a FEA model requires powerful mesh generation tools and is in practice a very time-consuming process. In addition, when dealing with the approximate solution itself, it is well-known that low-order FEA requires a very fine mesh size to produce accurate results in high gradients regions (e.g. in the case of singular solution with stress concentration phenomena) whereas high-order FEA has some restrictions on element topologies and continuity, so that it is hardly implemented in commercial FEA software.

After pioneering attempts [KFB98] to foster the link between CAD and FEA, and therefore facilitate numerical simulations with domains generated by CAD, a general computational framework proposing a direct link and referred as IGA was introduced in [HCB05,CHB09]. The idea consists of constructing the approximation basis, still using a standard isoparametric formulation, from the B-Spline or NURBS functions representing the CAD geometry. IGA thus aims at directly using the CAD representation of the geometry in the analysis step. It enables the simple use of smooth functions with high-order continuity (compared with C^0-continuity associated with Lagrange polynomials), so that fewer dofs are necessary compared to FEA to represent solutions of PDEs with high-order derivatives. Furthermore, it simplifies mesh refinement as the geometry is represented precisely at the lowest level of discretization and is unchanged throughout the refinement process so that no further communication with CAD is required. In fact, IGA was thoroughly studied and analyzed in the last decade [BBDVC+06,EBBH09,HRS10,LEB+10, BdVBRS11,ACH+12,SDS+12,NABR15], and successful applications were demonstrated to a wide range of structural mechanics problems [CRBH06,BCHZ08,EBCH08,GCBH08, KBLW09,BSV10,TWH11,DLWZ12,BEC15,NXHN14,DKYB15,HRVB15,KNTDLH15].

2.1.1 Applications of IGA

IGA has also shown advantages over traditional approaches in the context of **optimization problems** [WFC08,LQ11,FSV15] where the tight coupling with CAD models offers an extremely attractive approach for industrial applications [NABR15]. IGA permits to correct drawbacks of FEA due to the use of different mathematical languages in design or geometric modeling and numerical analysis: spline basis functions are used in design and geometric modeling, whereas Lagrangian and Hermitian polynomials are used in analysis [SKY10]. Isogeometric analysis is hence a very attractive and promising alternative to overcome the limitations resulting from the use of the conventional FEM in structural optimization. In isogeometric analysis, the same spline information such as control points and spline basis functions which represent geometries in CAD systems are also used in numerical analysis. Such a unification of the mathematical languages in CAD, analysis and design optimization can resolve the issues encountered with FEM. Figure 2.1 shows that with IGA, the geometrical optimization process is associated only with position variation of control points without constraints. The analysis optimizes a description that is already expressed in the language of computer aided geometric design (CAGD) [TWH11]. This helps avoiding mesh regeneration with classical approaches using FEM. In particular, with isogeometric boundary element methods that can require only a boundary discretization, creating a truly direct coupling with CAD, it was proved for elastostatic analysis in [SBTR12,SSE+13] that mesh regeneration can be completely circumvented by using CAD discretizations for analysis.

Moreover, in **contact formulations** using conventional geometry discretizations, the presence of faceted surfaces can lead to jumps and oscillations in traction responses unless very fine meshes are used. The benefits of using NURBS over such an approach are obvious, since smooth contact surfaces are obtained, leading to more physically accurate contact stresses [NABR15].

In order to alleviate the problems associated with non-smooth contact surface discretizations, various surface smoothing algorithms have been developed in the literature. These are based on either Hermite, spline or Bézier discretizations of the master surface defining the normal and tangent vector fields. This leads to a C^1- or even C^2-continuous representation of the surface. A summary on related works can be found for two- and three-dimensional discretizations of deformable solids being in contact in [TWH11]. These procedures lead in general to a more robust behavior of the iterative solution algorithms for contact since normal and tangent fields are continuous. However, they do not increase the order of convergence since the higher order approximations involve

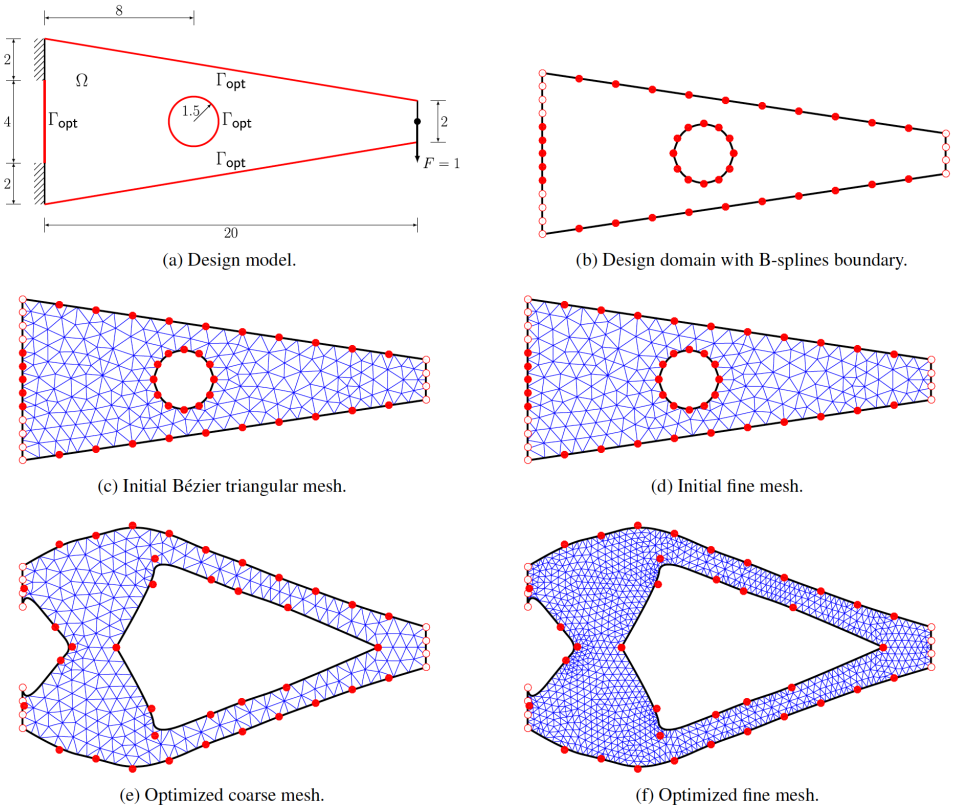

(a) Design model.

(b) Design domain with B-splines boundary.

(c) Initial Bézier triangular mesh.

(d) Initial fine mesh.

(e) Optimized coarse mesh.

(f) Optimized fine mesh.

Figure 2.1: Geometrical optimisation of a cantilever with three holes using IGA [WXWQ18].

only the surface but not the bulk behavior of the solids. With the isogeometric analysis framework, the continuous smooth surface approximation can now be combined with the corresponding higher-order discretization for the solids in contact. To do this, for the special case of the contact of a body with a rigid obstacle, various C^1-continuous surfaces can be defined directly from CAD models of the rigid obstacle.

The comparison on accuracy between C^0-continuous finite elements and NURBS is quantitatively examined in the context of the classical Hertz problem of a cylinder in contact with a rigid planar surface. It is found that a mortar-based knot-to-surface (KTS) approach behaves better than the standard KTS approach [TWH11]. The comparison studies indicate that NURBS provide better contact pressures than C^0-continuous Lagrange finite elements of the same order. In all cases, the NURBS contact pressures were pointwise-positive whereas C^0-continuous Lagrange finite element results exhibited non-physical negative values.

Shell and plate problems or rotationless thin shell formulations are another field where IGA has demonstrated compelling benefits over conventional approaches [BHB+13, KBLW09, BBHH11, BdVBL+12, EOB13, TWH11] (Figure 2.3). The smoothness of the NURBS basis functions allows for a straightforward construction of plate/shell elements. Particularly for thin shells, rotation-free formulations can be easily constructed [KBLW09]. Note that for multi-patch NURBS surfaces, rotation-free IGA elements require special treatment at patch boundaries where the basis functions are found to be C^0-continuous. Furthermore, isogeometric plate/shell elements exhibit much less pronounced shear-locking compared to standard FE plate/shell elements. Elements with smooth boundaries such as circular and cylindrical elements were successfully constructed using the IGA concept.

The smoothness of NURBS basis functions is also useful for the analysis of **fluids** [KNTDLH15,JKK] and **fluid–structure interaction** problems [BCHZ08,NABR15] (Figure 2.5). In fact, in the context of electromagnetic and incompressible fluids flow simulations, numerical discretizations have to preserve the geometric structure of underlying PDEs in order to avoid spurious behaviors, instability or non-physical solution. The numerical discretizations thus have to be related through a discrete De Rham complex [JKK].

General compatible spaces for finite element approximations were introduced by Arnold et al. [BBHH10], and more recently in isogeometric analysis context the smooth RT pair of spline based FE spaces provides divergence-free discrete solutions. Later us-

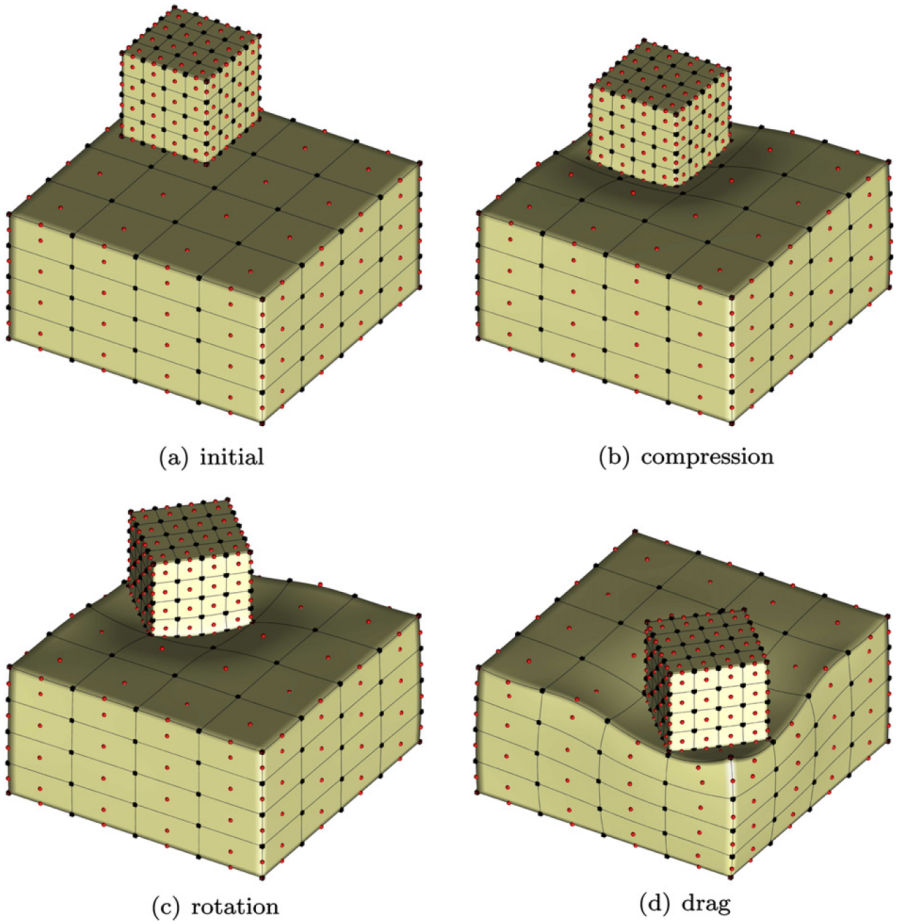

Figure 2.2: Three-dimensional contact of two deformable bodies based on NUBRS degree 2 discretization. The red dots are the control points, the black dots are the positions of the unique knot entries and the lines denote the element boundaries [TWH11].

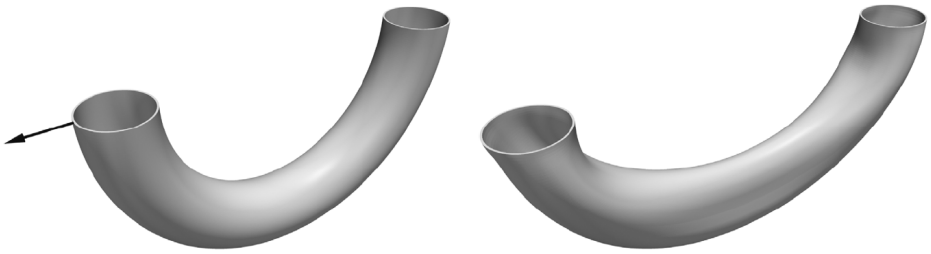

(a) Undeformed tube. (b) Deformed tube.

Figure 2.3: Hyper-elastic material model in the context of large deformations, applied to a cylindrical tube [DCV+16].

ing the idea of div-compatible spline spaces presented in the setting of discrete differential forms [BSEH11], a series of isogeometric divergence conforming spline discretizations were derived to solve Stokes and Brinkman equations, steady and unsteady Navier–Stokes equations by Evans in [BPS09]. These initial developments showed that isogeometric analysis is a highly accurate and efficient methodology to solve incompressible flow problems (Figure 2.4).

In addition, due to the ease of constructing high-order continuous basis functions, IGA has been used with great success in solving PDEs that incorporate fourth order (or higher) derivatives of the field variable such as the Cahn-Hilliard equation, explicit gradient damage models and gradient elasticity. The high-order NURBS basis has also found potential applications in the Kohn–Sham equation for electronic structure modeling of semiconducting materials.

The basis of IGA is also well-suited to solving higher-order partial differential equations, such as the ones related to phase-field problems [DCV+16] or large deformation shell formulations [BCHZ08, BR01, BdVBRS11]. The smoothness improves the accuracy per degree of freedom and allows the direct approximation of higher order PDEs [JKK]. Indeed, classical finite element spaces use basis functions which are C^0-continuous across element boundaries, making them unsuitable for higher-order problems using a primal Galerkin formulation. The NURBS-based spaces may be constructed to possess arbitrary degrees of inter-element continuity for any spatial dimension. These higher-order continuous basis functions have been numerically [BBHH10, BSEH11, BEC15] and theoretically [BSV10, CL12] observed to possess superior approximability per degree of freedom when compared to their C^0 counterparts. However, when used to discretize a

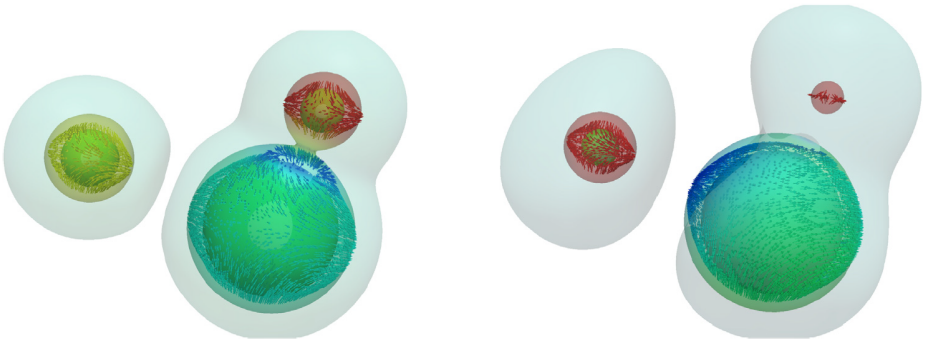

(a) Near the beginning of the simulation.

(b) Prior to the collapse of a bubble.

Figure 2.4: Three-dimensional version of the three bubble problem for the Navier–Stokes–Korteweg equation (a phase-field model for water and water vapor two-phase flows). Iso-contour surfaces reflect density values $\rho = \{0.15, 0.55\}$ revealing the location of the three bubbles. Velocity vectors are shown on each iso-contour and are colored by the velocity magnitude [DCV+16]

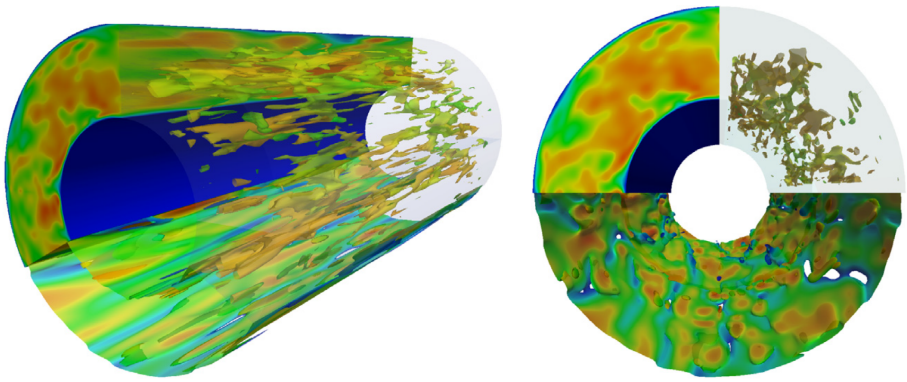

(a) Perspective view.

(b) Front view.

Figure 2.5: Turbulent flow through concentric cylinders. The top-left quadrant is a pseudocolor plot of the streamwise velocity. The top-right quadrant shows iso-contours of the vorticity magnitude for smaller values. The bottom quadrants show iso-contours of the vorticity magnitude for larger values. Both sets of contours are colored by the streamwise velocity with number of elements = 64^3 used [DCV+16]

Galerkin weak form, the higher-order continuous basis functions have also been shown to result in linear systems which are more expensive to solve with multifrontal direct solvers [CL08, LC15] and iterative solvers [CEG15]. These results motivate the development of efficient, scalable software frameworks which can mitigate the increase of cost.

In [CRBH06] , the research is able to determine a priori the error in frequency for a particular mode from a single function, no matter how many degrees-of-freedom are present in the model. These elementary results are very useful in determining the vibration characteristics of isogeometric models and provide a basis for comparison with standard finite element discretizations. It is well known that, in the case of higher-order finite elements, "optical" branches are present in the spectra and that these are responsible for the large errors in the high-frequency part of the spectrum and contribute to the oscillations (i.e., "Gibbs phenomena") that appear about discontinuities in wave propagation problems. The accurate branch, the so-called "acoustic" branch, corresponds to the low-frequency part of the spectrum. In finite element analysis, both acoustic and optical branches are continuous, and the optical branches vitiate a significant portion of the spectrum. In isogeometric analysis, when a linear parameterization of the geometrical mapping from the patch to its image in physical space is employed, only a finite number of frequencies constitute the optical branch. The number of modes comprising the optical branch is constant once the order of approximation is set, independent of the number of elements, but increases with order. In this case, almost the entire spectrum corresponds to the acoustic branch. A linear parameterization of the mapping requires a non-uniform distribution of control points. An algorithm which locates control points was proposed [CRBH06] to attain a linear parameterization. Spacing control points uniformly produces a nonlinear parameterization of the mapping. In this case, remarkably, the optical branch is entirely eliminated! The convergence rates of higher-order finite elements and isogeometric elements constructed by k-refinement are the same for the same order basis, but the overall accuracy of the spectrum is much greater for isogeometric elements. These observations corroborate the speculation that the k-method would be a more accurate and economical procedure than p-method finite elements in vibration analysis of structural members. Studies of membranes and thin plates provide additional corroboration. As a numerical example, a generalized eigenproblem is solved in [CRBH06] with both finite elements and isogeometric analysis using quadratic basis functions. The resulting natural frequencies, are presented in Figure 2.6, normalized with respect to the exact solution, and plotted versus the mode number, n, normalized by the total number of degrees of-freedom, N. To produce the spectra of Figure 2.6,

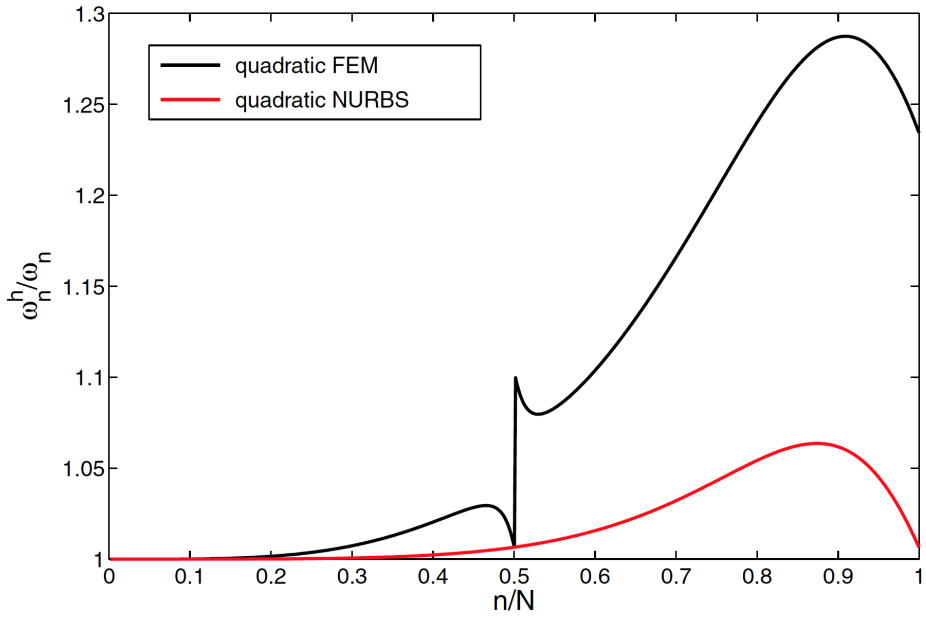

Figure 2.6: Fixed–fixed rod. Normalized discrete spectra using quadratic finite elements and NURBS [CRBH06].

$N = 999$ but the results are in fact independent of N. Figure 2.6 illustrates the superior behavior of NURBS basis functions compared with finite elements. In this case, the finite element results depict an acoustical branch for $n/N < 0.5$ and an optical branch for $n/N > 0.5$.

The IGA concept can be easily incorporated into existing FE codes by using the Bezier extraction [BSEH11]. Several open source IGA codes are available nowadays, such as PetIGA, and IGA implementations in commercial simulation software exist such as in Abaqus or LS-Dyna. Let us also quote a related method, proposed, and widely developed in literature and denoted NURBS enhanced FEM (NEFEM), that involves NURBS functions to construct the boundary of the mechanical structure alone while the interior remains discretized using FEA Lagrange basis functions [SFH11].

Besides the application of the IGA technology to the above-mentioned fields, this technique can also be applied to specific problems which have been solved with FE technology to attain the improved solution, e.g. in evaluating ballistic impact behavior of soft body projectiles, failure analysis of delaminated rotating composite conical shell, Numerical simulation of 3D thermo-elastic fatigue crack growth problems, etc. [AG19].

2.1.2 Drawbacks and challenges of IGA

Non-uniform rational B-splines (NURBS) is the dominant geometric representation format for CAD [JKK]. The construction of NURBS is based on a tensor product structure and, as a consequence, knot insertion is a global operation. From an analysis perspective, the tensor product structure of NURBS proves to be inefficient, caused by the global nature of refinement operations. In turn, this leads to inefficient error estimation and adaptivity algorithms. To remedy this a local refinement can be achieved by breaking the global tensor product structure of multivariate splines and NURBS. Several techniques have been proposed to address this point, among others are T-splines, Hierarchical B-splines, Truncated Hierarchical B-splines and Locally Refined (LR) B-splines [JKK]. However, which method is the best is a topic for researchers in the field.

The advantages of IGA for the solution of challenging contact problems are quite evident, and stem from the favorable properties of isogeometric basis functions [LWH14], most notably, the higher and controllable continuity at the inter-element boundary achieved for the geometry but also, within an isoparametric approach, for the unknown displacement field, and the convex hull and variation diminishing properties. These advantages have not yet been fully explored and exploited. A few open issues and possible directions for further research, as directly emerging from the above review, are summarized as follows:

- the efficiency and robustness of isogeometric mortar contact formulations is strongly influenced by the strategy used for the computation and storage of the mortar integrals. The development of accurate and yet efficient integration schemes would thus represent a significant advancement, as would the development of dual mortar formulations for the condensation of the additional degrees of freedom arising in a Lagrange multiplier approach;

- the local refinement capability of T-spline interpolations and the ability to represent a complex geometry of arbitrary topology as a single watertight parameterization have recently been proved to provide significant advantages for contact modeling when compared to NURBS interpolations. To fully exploit these advantages, error-controlled adaptive refinement procedures are needed. For the same purpose, alternative basis functions such as hierarchical B-splines or isogeometric spline forests could also prove interesting. Moreover, mortar-based contact formulations have never been applied to isogeometric discretizations capable of local

refinement;

- the higher smoothness of isogeometric basis functions leads to inaccuracies at the boundaries between contact and no-contact regions, i.e. where the exact contact pressure distribution features C^0-continuity possibly within an element. While not leading to oscillatory behavior (differently from what is observed in FEM), these situations may compromise optimal convergence and could be tackled using ad-hoc strategies such as local lowering of continuity, local knot relocation, and local partition of unity approaches. This issue has not yet been addressed; as isogeometric collocation emerges as a competitive technology in computational mechanics, further investigations should be conducted on contact within the collocation framework, where the first steps have recently been taken and have shown very promising results.

2.2 Up-to-date error estimation techniques for IGA

Once a numerical solution has been computed, it is important to ensure the quality of this solution. Since, typically, the exact solution is not known, it is not possible to compute the exact error. Hence, it is necessary to find computable bounds for the unknown error in order to quantify the accuracy of the numerical solution. Despite the importance of this issue, a posteriori error estimation in IGA is still in an infancy stage.

On the one hand, some a priori error estimates were first developed in parallel with the IGA framework in order to evaluate its convergence properties and show that they are similar to those obtained in a classical FEA setting [BBDVC+06, BdVBRS11]. On the other hand, and contrary to the wide literature available for FEA (see e.g. [Ver94, BSU+94, AO97, LP05, LC15] for an overview), very few a posteriori error estimates are currently available for IGA in order to estimate the distance between the unknown exact solution and the numerical solution. However, they would represent useful tools to quantitatively indicate on the error distribution, to identify areas where further refinement is needed, and thus to drive adaptive algorithms efficiently. The Zienkiewicz–Zhu estimation is used on error estimator based local refinement using LR B-splines [GYVL+18]. The local refinement is implemented by the structured mesh refinement strategy according to the a posteriori error estimator (Figure 2.7).

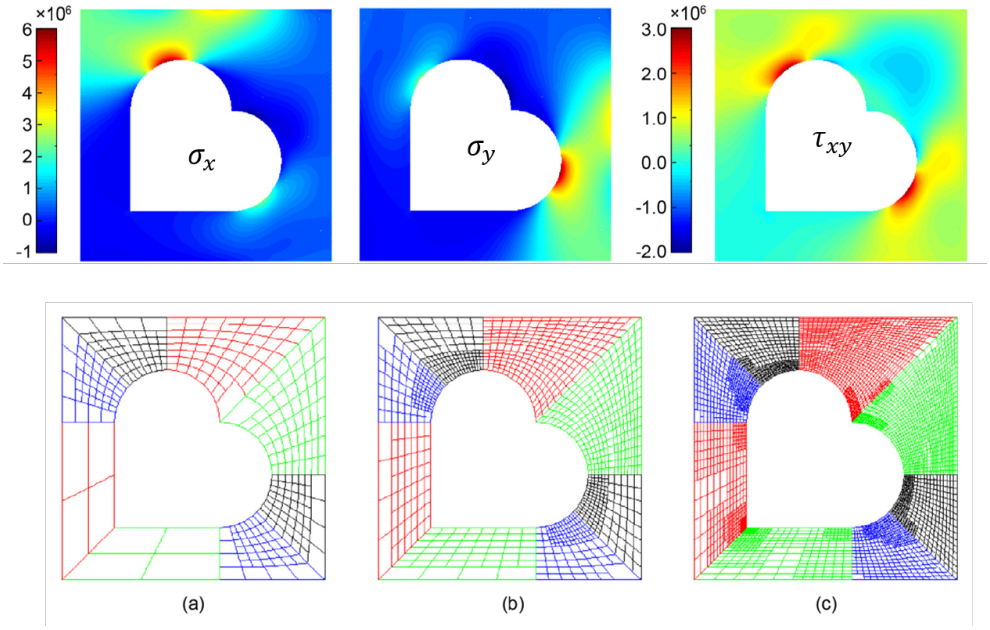

Figure 2.7: Distribution of stresses (top) corresponding to the map of errors and associated steps of refinement (bottom) [GYVL+18].

2.2.1 Error estimation based on equilibrium residuals for IGA

Explicit estimators

In the IGA framework, most available tools are essentially dedicated to linear elliptic problems. For instance, explicit residual-based a posteriori error estimates are developed in [XMDG11]:

$$\|e_h\|^2_{E(\Omega)} \leq C \sum_{K \in \sigma} h_K^2 \|R_K\|^2_{L^2(K)} \tag{2.1}$$

where K is the sub-patch in the B-spline parameterization $\sigma(\xi, \eta)$ of Ω with respect to the knot elements in the parametric domain P; C is a constant and h_K is the diameter of patch $K \in \sigma$; $R_K(x) = f(x) + \Delta U_h(x)$ in K is the interior sub-patch residual of the IGA solution U_h of a second order elliptic PDE, for example: $\Delta U(x) = f(x)$ in a domain Ω with homogeneous Dirichlet boundary condition $U(x) = 0$ on $\delta\Omega$.

In fact, this approach was originally developed in FEA. The approximate FE solution does not satisfy the governing partial differential equation. This lack of fulfillment is called the residual and the error can be estimated by solving local problems where the load functions are given by the local residuals. Therefore, the main idea can be extended

for IGA solutions. These error estimates can be then optimized by a parametrization technique based on control points coordinators (Figure 2.8).

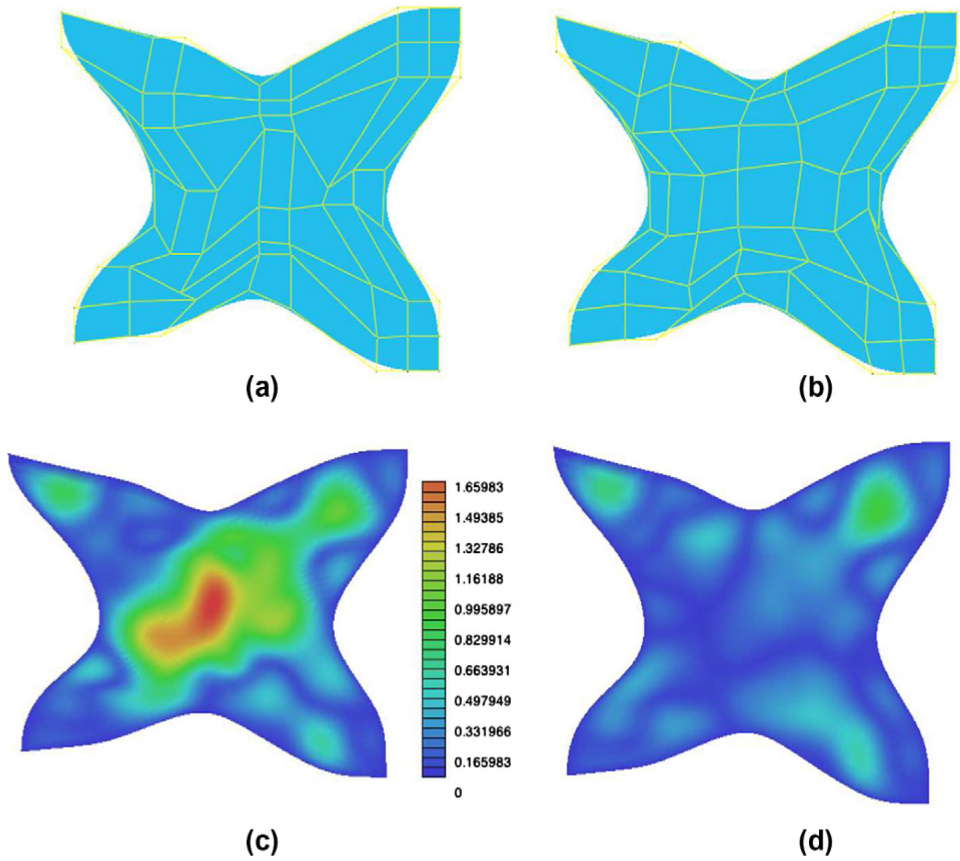

Figure 2.8: Optimization of explicit residual-based a posteriori error estimates based on control points coordinators : (a) initial computational domain; (b) final computational domain ; (c) initial simulation error; (d) final simulation error with same scale [XMDG11].

Such error estimates are easy to implement but they require the computation of mesh-dependent constants associated with Clément-type interpolation operators, and may lead to over-estimations. This makes them less popular among the engineering community. On the other hand, for the implicit residual based approach, a local problem is solved over each of the local subdomains (either individual elements, patches of elements or subdomains consisting of an element and its neighborhood elements). Depending on how the local problem is linked to the global FE solution, different properties of the estimates

can be obtained. For instance, the equilibrated element approach, the flux free approach, and the constitute relation error yield estimates that give an upper bound on the error, while error estimates based on local problems with Dirichlet boundary conditions give a lower bound on the error. In [XMDG12], this type of error assessment method was more optimized with solving the residual equation using several k-refinement steps, which may be very expensive.

Implicit estimators based on the hierarchical method

In [DJS10], authors introduce a posteriori error estimates used in combination with T-splines based on the hierarchical method developed in [BS93], and in which the residual equation is approximately solved using hierarchical bases and bubble functions. These are applied to linear and elastic plate in traction with a circular hole and in fluid analysis for (advection dominated) advection–diffusion problems as examples. Error convergence was shown to be better with a T-spline refinement (Figure 2.9).

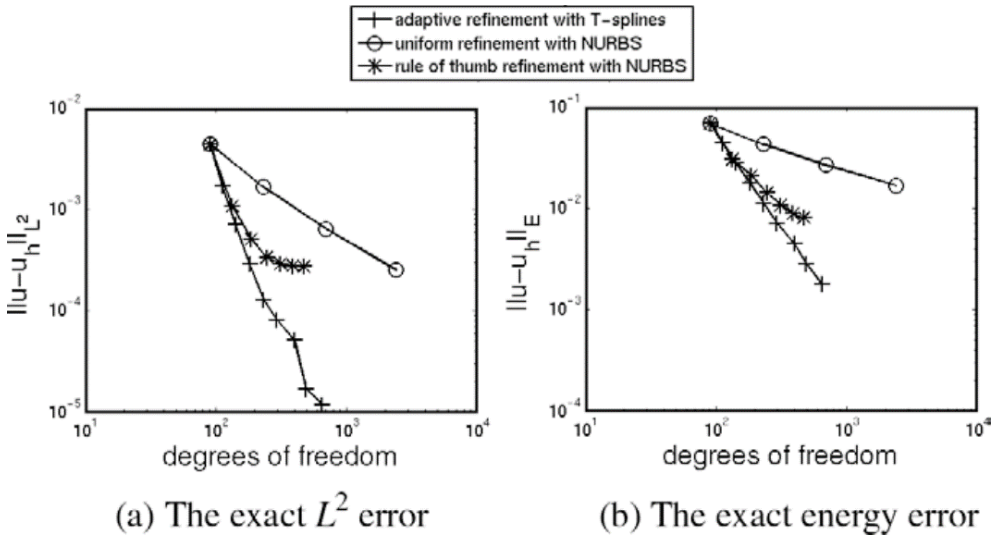

Figure 2.9: Comparison of the convergence of the adaptive algorithm versus the two non-adaptive ones for linear and elastic plate in traction with a circular hole [DJS10].

However, their reliability and efficiency are subjected to a saturation assumption on the enlarged underlying space and the constants in the strengthened Cauchy inequality; consequently, bounding results are not guaranteed and problem dependent.

Functional-type a posteriori error estimates for IGA

Eventually, a functional-type a posteriori error estimate is proposed in [KT15] leading to guaranteed and sharp upper bounds of the exact error in the energy norm provided constants can be accurately estimated or bounded (which is not always possible in practice). They are applicable for any conforming and non-conforming discretizations. The previous method, using $H(div, \Omega)$ spaces which are easily reachable when considering NURBS basis functions, is closely related to the approach proposed in this thesis even though there are fundamental differences (e.g. the verification of balance equations is not imposed in [KT15] for the construction of the estimate). Moreover, this approach always needs to solve a global problem in order to compute an auxiliary function $y \in H(div, \Omega)$, which is extremely expensive in most of cases. Authors made an attempt to reduce the cost of computations for tensorial spline spaces but the idea of cost reduction needs further study in adaptive isogeometric analysis.

A goal-oriented error estimation procedure was developed in [KVvdZvB14], in which a classical dual-weighted residual (DWR) technique is used with p-refinement of the adjoint solution.

2.2.2 Error estimation based on based on a smoothing of the stresses for IGA

In [KKJ17], the error estimation method for IGA denoted recovery-based estimates is presented. A very popular prototype for such approaches is the Zienkiewicz–Zhu type method (so called ZZ-type method). This method with superconvergent patch recovery (SPR) was proposed by authors [KKJ17] to construct a posteriori error estimates in adaptive IGA for solving second order elliptic problems. An improved gradient from recovery procedure was used instead of exact gradient of the exact solution.

A simple comparison on the performance of two error estimates, i.e. an explicit residual based error estimate η_{Res} vs. SPR based ZZ-estimate η_{SPR}, was performed in [KKJ17]. This focused on the approximation of true error and quality of estimates measure in terms of effectivity index θ, which can be defined by the ratio of estimated error with exact isogeometric FE error. The results showed a good quality of SPR based ZZ-estimate with respect to the explicit residual based error one (Figs. 2.10 and 2.11).

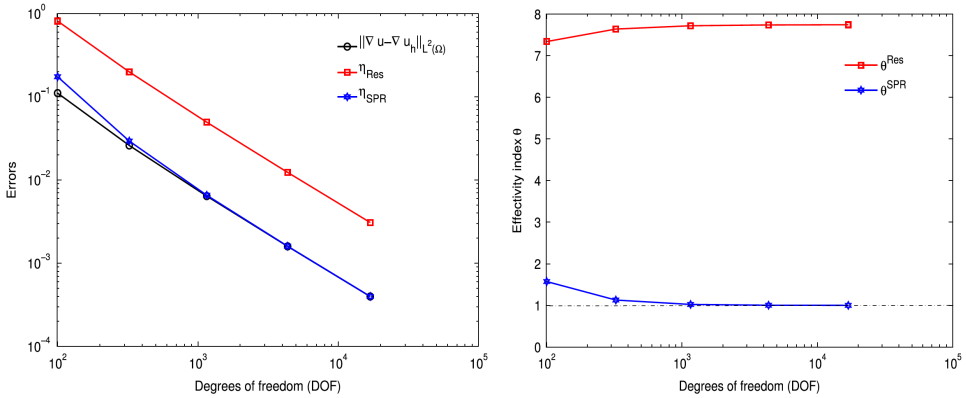

(a) Errors. (b) Effectivity index θ.

Figure 2.10: Comparison of errors and effectivity index between residual based error estimate η_{Res} and the proposed SPR based error estimate η_{SPR} for IGA using quadratic B-splines with uniform h-refinement in the case of a sinus problem [KKJ17].

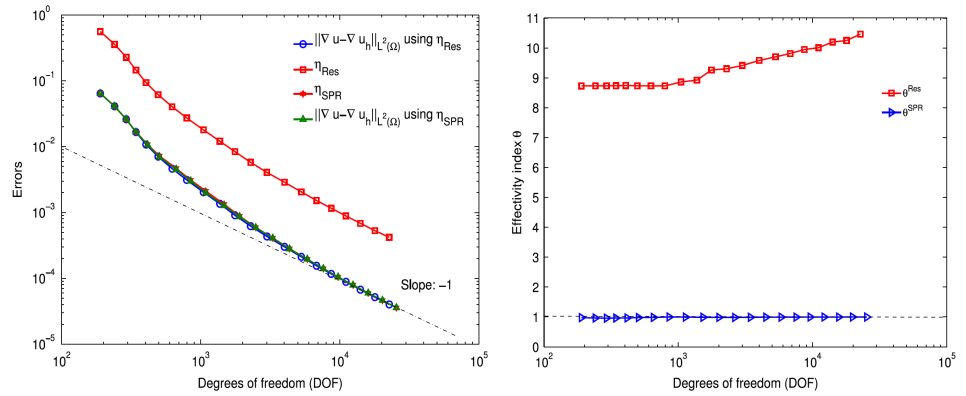

(a) Errors. (b) Effectivity index θ.

Figure 2.11: Comparison of errors and effectivity index between residual based error estimate η_{Res} and the proposed SPR based error estimate η_{SPR} for isogeometric FE using quadratic LR B-splines with adaptive h-refinement in the case of a L-shaped domain problem [KKJ17].

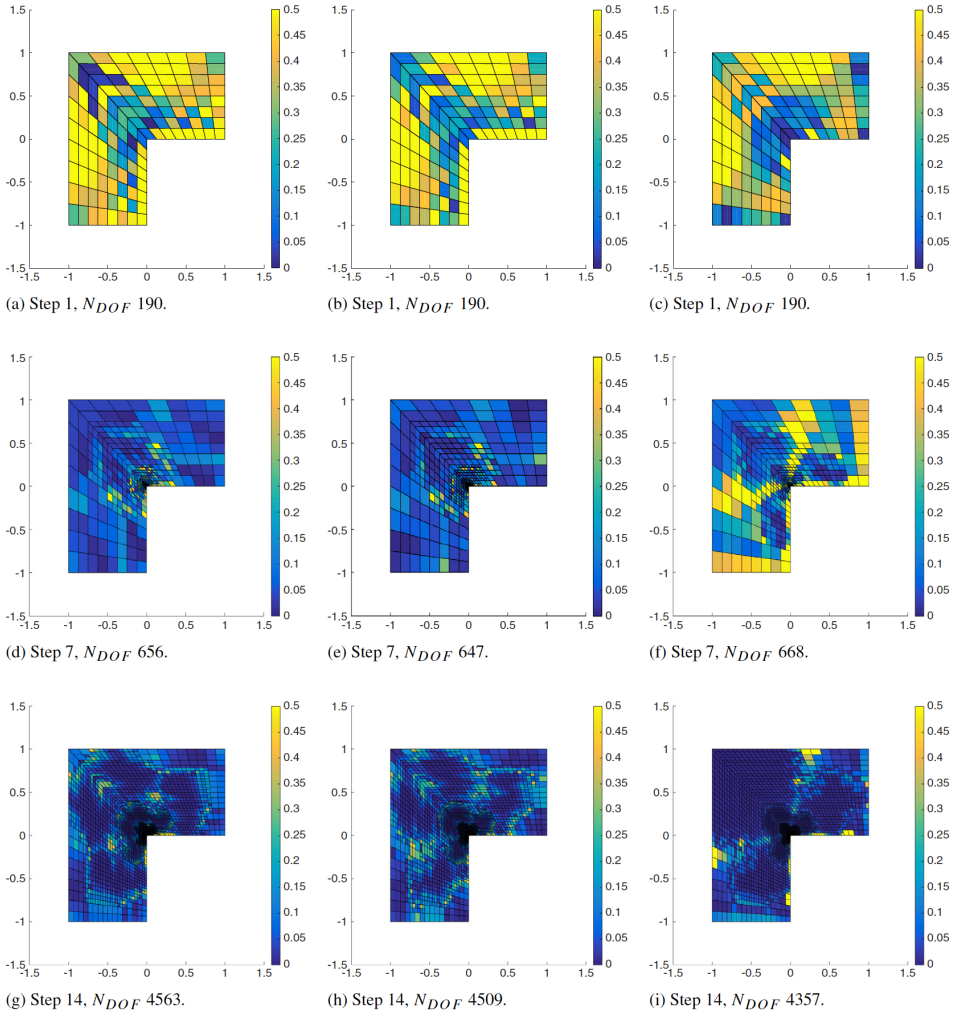

(a) Step 1, N_{DOF} 190. (b) Step 1, N_{DOF} 190. (c) Step 1, N_{DOF} 190.

(d) Step 7, N_{DOF} 656. (e) Step 7, N_{DOF} 647. (f) Step 7, N_{DOF} 668.

(g) Step 14, N_{DOF} 4563. (h) Step 14, N_{DOF} 4509. (i) Step 14, N_{DOF} 4357.

Figure 2.12: L-shaped domain problem: Comparison of absolute value of the deviation effectivity index at element level $|1-\theta^*_{el}|$ at LR meshes obtained via adaptive LR B-splines refinement algorithm for degree $p = 2$ using different recovery based error estimators at different refinement steps for a L-shaped domain problem. The columns from left to right represent the cases with respect to Continuous L^2 projection (CL2P), Discrete least square fitting (DLSF) and Superconvergent patch recovery (SPR), respectively [KKJ17].

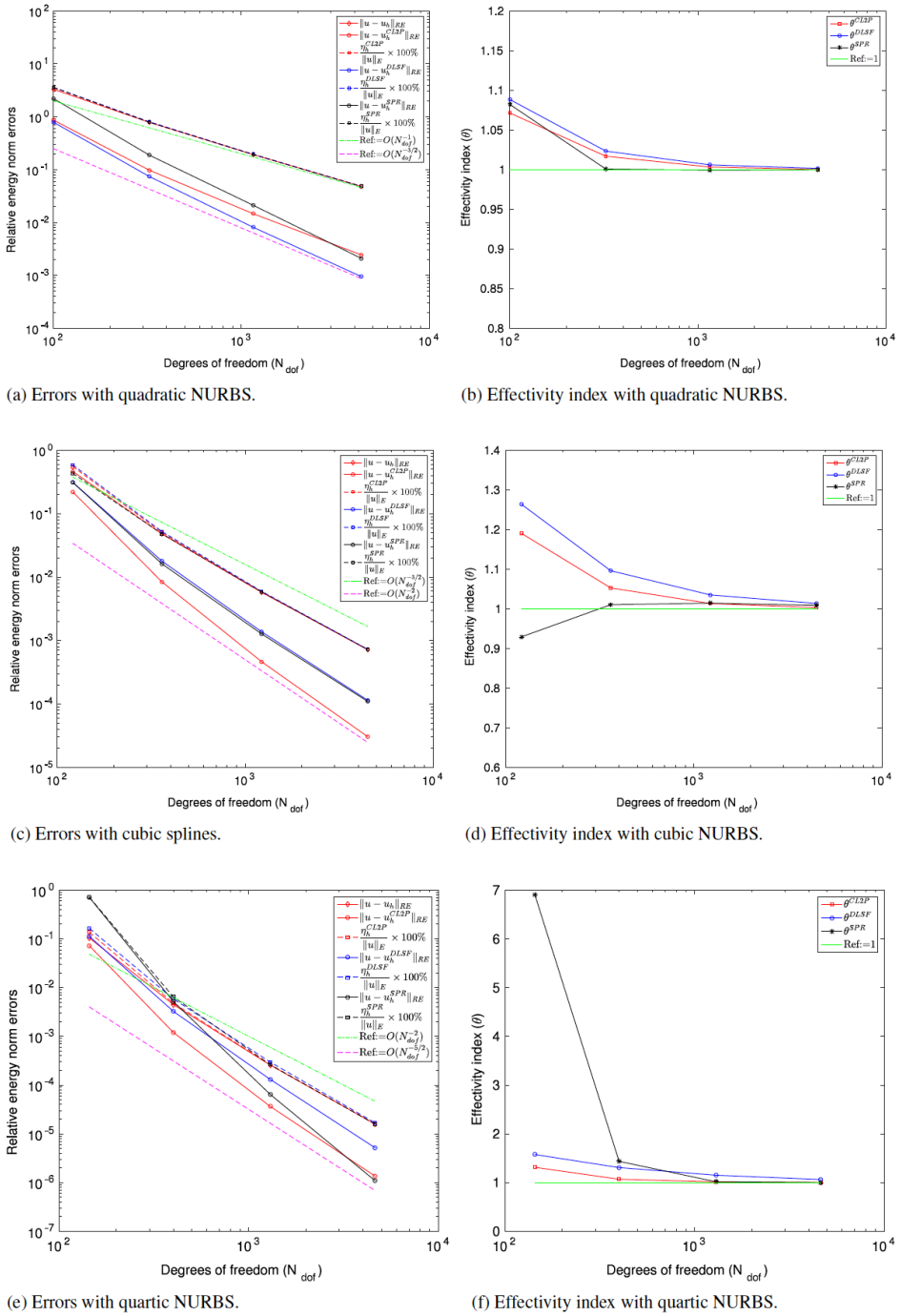

(a) Errors with quadratic NURBS.

(b) Effectivity index with quadratic NURBS.

(c) Errors with cubic splines.

(d) Effectivity index with cubic NURBS.

(e) Errors with quartic NURBS.

(f) Effectivity index with quartic NURBS.

Figure 2.13: Circular domain problem: errors and effectivity index results obtained with different recovery procedures (CL2P, DLSF and SPR) using NURBS spaces of degrees p = 2, 3, 4 to approximate the solution u_h with uniform h-refinement [KKJ17].

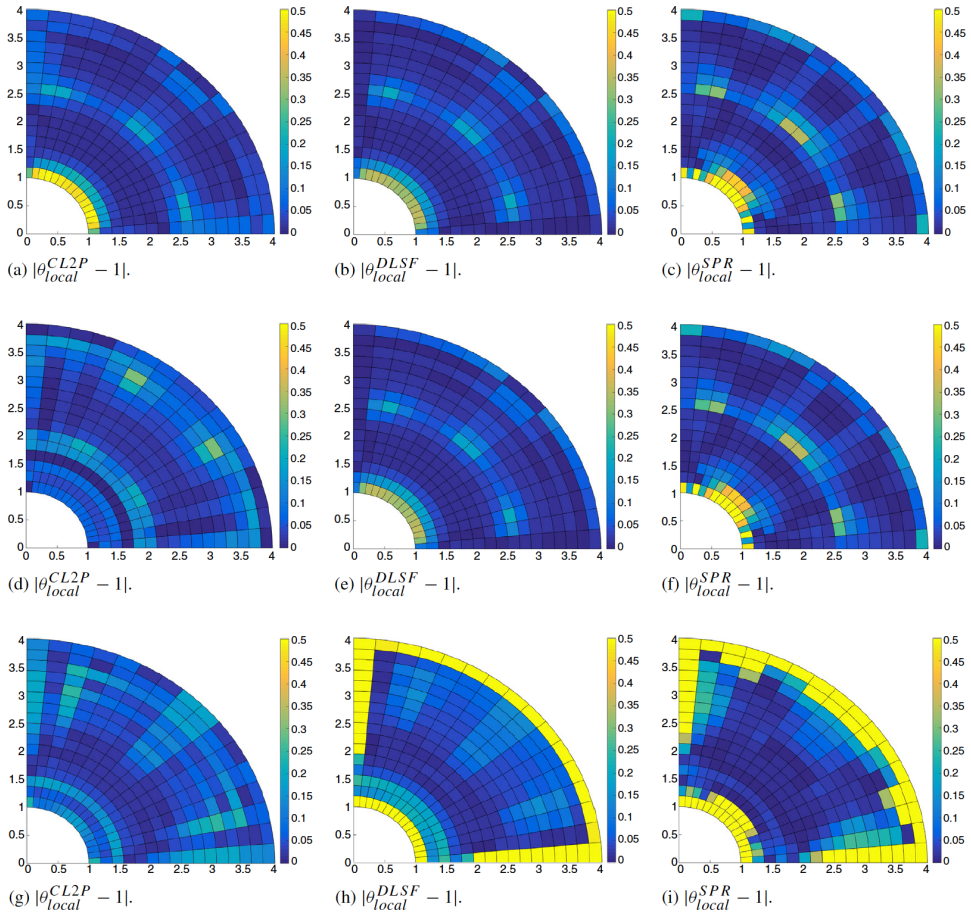

(a) $|\theta_{local}^{CL2P} - 1|$. (b) $|\theta_{local}^{DLSF} - 1|$. (c) $|\theta_{local}^{SPR} - 1|$.

(d) $|\theta_{local}^{CL2P} - 1|$. (e) $|\theta_{local}^{DLSF} - 1|$. (f) $|\theta_{local}^{SPR} - 1|$.

(g) $|\theta_{local}^{CL2P} - 1|$. (h) $|\theta_{local}^{DLSF} - 1|$. (i) $|\theta_{local}^{SPR} - 1|$.

Figure 2.14: Circular domain problem: comparison of deviation of local effectivity index $|1 - \theta_{local}^{*}|$ obtained by Continuous L2-projection (CL2P), Discrete least square fitting (DLSF), and Superconvergent patch recovery (SPR) for NURBS (first row (p = 2), second row (p = 3), and third row (p = 4)) approximate solution u_h at step 2 of uniform refinement [KKJ17]

Different recovery procedures can be used to improve the computed gradient ∇u_h, where u_h is the computed FE solution from NURBS (or B-splines, LR B-splines) based isogeometric analysis. Indeed, an improved gradient ∇u_h^* can be obtained in two different ways: (i) global projection over the domain Ω, (ii) local smoothing of the gradient components over small patches of elements. For the first approach, there are two global recovery procedures denoted as Continuous L2 projection (CL2P) and Discrete least square fitting (DLSF), respectively, where the computed gradient components of the

solution are projected onto the same NURBS (or B-splines, LR B-splines) space that was used for the computation of u_h in FE approximation. For the second approach, the Superconvergent Patch Recovery (SPR) procedure was extended from FEA to isogeometric analysis in [KKJ17]. The main idea of SPR was based on the existence of some points with high accuracy, i.e., derivative superconvergent points within each element. The obtained global effectivity indices for all the three recovery techniques are close to one (Figure 2.13). This is in contrast to classical residual based error estimates. Moreover, the local elementwise effectivity indices for all the three recovery techniques are also close to one, after some initial refinement steps that are needed to keep any possible pollution effects under control (Figs. 2.12 and 2.14).

However, the existence and location of such superconvergent points in isogeometric analysis is not known in literature. Thus for instance the term "sampling points of high accuracy" was used instead of "true derivative superconvergent points" for the SPR procedure. The existence and location of true derivative superconvergent points for different model problems as well as the computation based on these points are still in discussion. Therefore, superconvergence properties and accuracy of the obtained estimate are restricted to specific problems and meshes, for example, for the class of smooth solutions approximated on patch-wise uniform grids of linear or quadratic elements.

2.2.3 Proposing error estimation based on the concept of error in constitutive relation for IGA

The up-to-date error estimation techniques for IGA have numerous limitations. Based on the advantages of CRE in the introduction part, we therefore propose to use the Constitutive Relation Error (CRE) concept for IGA. The CRE concept is based on duality and requires to recover fully equilibrated fields as all error estimation techniques providing for guaranteed bounds without any constant [AO93, DM99, CF99, MMP00, Zie01, BPS09, AM17];

The main technical issue is to recover the admissible stress part. Among the various techniques which enable to perform such a recovery, we focus here on the hybrid-flux (or EET) technique initially developed in [LL83] then extended and enhanced in several works thereafter [LM96, LR97, LCF10, PCL11, RGR14, ACL18]; some alternative techniques can be found in [PDH06, Gal09, EV10] for instance. The hybrid-flux technique, in the FEA context, performs at the element level and involves the construction of equilibrated tractions on element edges before solving local and cheap Neumann problems on each element. We propose here to revisit this technique in order to extend it to IGA; the difficulty lies in the modified notion of locality for IGA basis functions (i.e. spline

functions), as they have a larger support over knot spans than FE basis functions (i.e. Lagrange functions) have over elements. As the technique is general (as merely based on balance equations), we illustrate it on a simple scalar elliptic problem (steady-state thermal problem for instance) in order to keep notations simple and avoid unnecessary details. Moreover, we do not address adaptive strategies with local mesh adaptation as they refer to classical and now well-known techniques.

The proposed procedure thus enables to apply CRE error estimates for linear and nonlinear structural mechanics problems solved with IGA. Performance of the approach, in terms of behavior of the computed CRE estimate, is shown on several numerical experiments. It enables to derive guaranteed and fully computable a posteriori error estimates on the numerical solution provided by IGA. Such estimates, which are valid for a wide class of linear or nonlinear structural mechanics models, thus constitute performing and useful tools to quantitatively control the numerical accuracy and drive adaptive procedures. The focus here is on the construction of equilibrated flux fields, which is key ingredient of the CRE concept, and which was until now almost exclusively developed in the FEA framework alone. The extension to IGA requires to address some technical issues, due to the use of B-Spline/NURBS basis functions. The CRE concept is also implemented together with adjoint techniques in order to perform goal-oriented error estimation.

2.3 Reduced order modelling for parametrized geometry

2.3.1 IGA-based reduced order modelling

To the best of our knowledge, the first study of the combined use of IGA and POD methods is showed in [ZDQ17]. Preliminary related IGA-ROMs have been applied to steady potential flows, parabolic problems or shell structural models. In this work offline–online IGA-ROM is applied for the development of stable computational reduction strategies for viscous flows problems in parametrized shapes by FFD means. Besides the investigation of the other side of the spectrum of incompressible regimes (that is, when the Reynolds number tends to zero), is the coupling of FFD techniques applied to IGA geometries, for internal flows, and using finite element based IGA, in view of studies dealing with nonlinear viscous flows, for which BEM is not suited.

In fact, boundary Element Method (BEM) with IGA is a better seamless integration due to the same boundary representation [LWW+17]. Relying on this benefit, the model could be recomputed without extra mesh construction, meanwhile, this study introduces the model reduction technique to narrow the reanalysis scale and enhance efficiency.

NURBS surfaces are used to construct the model geometry and calculation element. The problem is treated as a state evolution process, it is proceed by approximating the problem solution using the most appropriate set of approximation basis, which depend on the Proper Generalized Decomposition (PGD). The IGABEM calculation combined with the reduction model strategy is proposed in this paper which allow the accurate and fast resolution of IGABEM problems. Moreover, the CPU time is drastically reduced, the numerical example treated, proves the potentiality of this numerical technique. This provides a proper condition that structure optimization bases on.

2.3.2 PGD for parametrized geometry

When dealing with parametrized geometry, several works already introduced model reduction techniques, using FEA or IGA formulations [Boy08,Ngu08,LR10,Roz11,MQR12, MSH15, ZDQ17]; they are mainly based on POD or reduced basis approaches. We focus here on the Proper Generalized Decomposition (PGD) technique, which is an alternative appealing model reduction technique based on low-rank canonical format approximation [CAC10, LV10, Nou10, CLC11, CLB+13, CKL14, CL14, ZCDA18]. It operates in an iterative strategy in which a representation of the solution is defined as a linear combination of separated variables functions (called modes), after defining all model parameters as extra-coordinates of the problem. Modes are computed on the fly in an *offline* step, by solving eigenvalue problems and without any knowledge on the solution (snapshot) compared to POD. An approximate solution of the model can then be obtained for any value of the parameters and be used in an *online* phase, with cheap and fast computations on light computing platforms, in order to perform real-time parametric or sensitivity analysis for optimization, inverse identification, or optimal control purposes. The PGD technique was successfully implemented for many applications with parametric analyses, including parametrized geometry [CNS13, AHC+14, ZDMH15, CNLB16, SZD17]. Here, we go one step further by coupling PGD with IGA. PGD extra-coordinates are then related to the coordinates and weights of control points (at the coarsest mesh level), and separation of variables is introduced between space and geometry variables. This enables to obtain virtual charts for shape optimization, with explicit and continuous dependency of the solution to design variables. Shape sensitivities can then be performed in a straightforward manner, without resorting to classical adjoint state methods [LT03].

In this thesis, IGA is coupled with PGD in order to get certified real-time solutions to problems with parameterized geometry. After defining the parametrization on the mapping from the IGA parametric space to the physical space, a reduced model based

on the PGD is introduced to solve the multi-dimensional problem. From an offline/online strategy, the procedure then enables to describe the manifold of parametric solutions with reduced CPU cost, and to further perform shape optimization in real-time. Here again, a posteriori estimation of the various error sources inheriting from discretization and PGD model reduction is performed from the CRE concept. It enables to control the quality of the approximate PGD solution (globally or on outputs of interest), for any geometry configuration, and to feed a robust greedy algorithm that optimizes the computational effort for a prescribed error tolerance. The overall research work thus provides for reliable and practical tools in mechanical engineering simulation activities. Capabilities and performance of these tools are shown on several numerical experiments with academic and engineering problems, and with linear and nonlinear (damage) models.

Chapter 3

Fundamentals of IGA

Contents

3.1 B-spline 34
3.1.1 Knot vector 34
3.1.2 B-spline basis functions 35
3.1.3 B-spline geometry 40
3.1.4 Non-Uniform Rational B-spline 44
3.2 B-spline refinement 46
3.2.1 Knot insertion 48
3.2.2 Order elevation 51
3.2.3 k-refinement 53
3.3 The IGA framework 53
3.3.1 Model problem 53
3.3.2 IGA code architecture 57
3.3.3 Similarities and differences between IGA and FEA 58
3.4 Mapping in IGA 58
3.4.1 Index space 60
3.4.2 Parametric space 60
3.4.3 Physical space 61
3.4.4 Control mesh 62

In this chapter, we aim at generally introducing the fundamentals of IGA. For more straightforward understandings of IGA, this chapter presents numerous IGA features that are similar to FEM. The root reason that leads IGA to different features compared

to FEM is the B-spline or NURBS basis functions. Thus, we briefly review the definition and specificities of B-spline and NURBS.

3.1 B-spline

B-spline functions are built from a set of polynomial functions that are defined on non-overlapping connected intervals. B-splines are consequently smooth, differentiable and continuous functions within each subinterval. B-splines are used as basis functions in most CAD programs because they are very well suited for representing geometries consisting of curves or surfaces.

A basis of n univariate 1D B-spline functions of order p can be defined from a knot vector $\boldsymbol{\Xi} = \{a = \xi_1, \xi_2, \ldots, \xi_{n+p+1} = b\}$, in which the knots ξ_i are sorted in the ascending order.

3.1.1 Knot vector

Definition 3.1.1. Knot vector It is defined as a finite number of real values $\Xi = \{\xi_1, \xi_2, \ldots, \xi_{n+p+1}\}$. These values ξ_i are sorted in the ascending order.

In this notation:

- ξ_i is the ith knot;
- p is the polynomial order;
- n is the number of B-spline basis functions.

There are many types of knot vectors such as uniform, open uniform, or non-uniform knot vectors. A knot vector is uniform if the knots spans (see definition below) are equal in parameter space, otherwise it is non-uniform.

Definition 3.1.2. Open knot vector: If the first and last knot values are repeated $p + 1$ times, the knot vector is said to be open.

Most commonly, open knot vectors are used in CAD. An important property of B-splines formed from open knot vectors is that they are interpolatory at their start and end points. This property facilitates the application of boundary conditions for analysis. The use of a non-uniform knot vector allows us to obtain much richer behavior than a simple uniform one.

Remark. Only open knots are considered in IGA.

Remark. More than one knot can be located at the same coordinate in the parametric space. These are referred to as repeated knots. Repeated knot values cause a reduction of the continuity of the basis functions at that knot. The multiplicity $r_j = 1$ at the knot leads to C^{p-1} continuity, multiplicity $r_j = p$ leads to C^0 continuity, whereas multiplicity $r_j = p + 1$ leads to a discontinuity.

Definition 3.1.3. Knot-spans: It is the range of parameter values between two successive knots $\{\xi_i, \xi_{i+1}\}$.

It is called empty knot span if $\xi_i = \xi_{i+1}$. It is called an interior knot span if $\xi_i < \xi_{i+1}$. The interior knot span is used to create "elements" in IGA.

3.1.2 B-spline basis functions

Definition 3.1.4. B-spline basis functions are defined recursively from the knot vector Ξ using the Cox-de Boor algorithm [PT95].

B-spline basis functions of degree p, denoted $N_{i,p}$ $(i = 1, \ldots, n)$ with n the number of basis functions, are constructed from the knot vector $\Xi = \{\xi_1, \xi_2, \ldots, \xi_{n+p+1}\}$; $N_{i,p}$ is the ith basis function of order p. The construction of $N_{i,p}$ is started with the zeroth order basis function $(p = 0)$:

$$N_{i,0}(\xi) = \begin{cases} 1 \text{ if } \xi_i \leq \xi \leq \xi_{i+1} \\ 0 \text{ otherwise} \end{cases}$$

then for $1 \leq k \leq p$ and $1 \leq i \leq n + p - k$

$$N_{i,k}(\xi) = \frac{\xi - \xi_i}{\xi_{i+k} - \xi_i} N_{i,k-1}(\xi) + \frac{\xi_{i+k+1} - \xi}{\xi_{i+k+1} - \xi_{i+1}} N_{i+1,k-1}(\xi) \tag{3.1}$$

Whenever a zero denominator appears in the above formula, the corresponding term is considered to be zero.

$$\frac{\xi - \xi_i}{\xi_{i+k} - \xi_i} = 0 \quad if \quad \xi_{i+k} - \xi_i = 0$$

$$\frac{\xi_{i+k+1} - \xi}{\xi_{i+k+1} - \xi_{i_1} = 0} \quad if \quad \xi_{i+k+1} - \xi_{i+1} = 0$$

The derivatives of B-spline functions can also be obtained recursively:

$$\frac{d}{d\xi} N_{i,k}(\xi) = \frac{k}{\xi_{i+k} - \xi_i} N_{i,k-1}(\xi) - \frac{k}{\xi_{i+k+1} - \xi_{i+1}} N_{i+1,k-1}(\xi) \tag{3.2}$$

for $1 \leq k \leq p$ and $1 \leq i \leq n + p - k$.

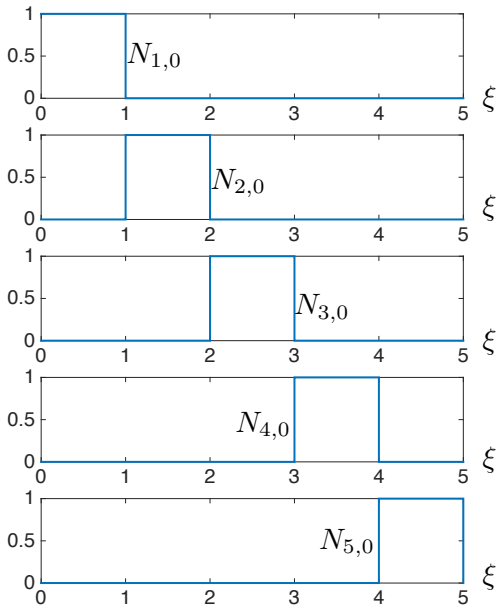

H

Figure 3.1: The non-zero zeroth-degree basis functions, constructed from the knot vector $\Xi = \{0, 1, 2, 3, 4, 5\}$.

The number of basis functions is determined by the order p and the number of knots in the knot vector. Increasing the number of knots will consequently also increase the number of basis functions.

Definition 3.1.5. Based on the number of knots m and the degree of basis functions p, we can define the number of B-spline basis functions n as:

$$n = m - p - 1 \tag{3.3}$$

In order to better imagine the formula 3.1, we construct B-spline functions of a uniform knot vector $\Xi = \{0, 1, 2, 3, 4, 5\}$ and an open knot vector $\Xi = \{0, 0, 0, 1, 2, 3, 4, 4, 5, 5, 5\}$.

Figures 3.1, 3.2, and 3.3 show the example of B-spline functions from degree 0 to degree 2 of the uniform knot vector $\Xi = \{0, 1, 2, 3, 4, 5\}$. With degree $p = 0$, the number of B-spline basis functions is n= 5. With degree $p = 1$, the number of basis B-spline functions is $n = 4$. With degree $p = 2$, the number of B-spline basis functions is n= 3. These basis functions are plotted in Figure 3.1, 3.2, and 3.3, respectively. For B-spline functions with $p = 0$ and $p = 1$, we have the same result as for standard piecewise constant and linear FEM functions, respectively.

According to the formulation, we note that:

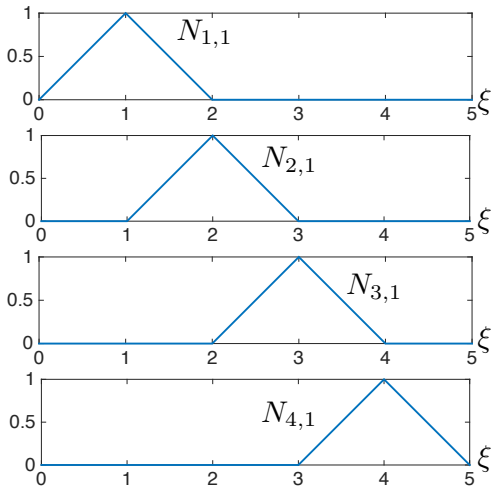

Figure 3.2: The non-zero first-degree basis functions, constructed from the knot vector $\Xi = \{0, 1, 2, 3, 4, 5\}$.

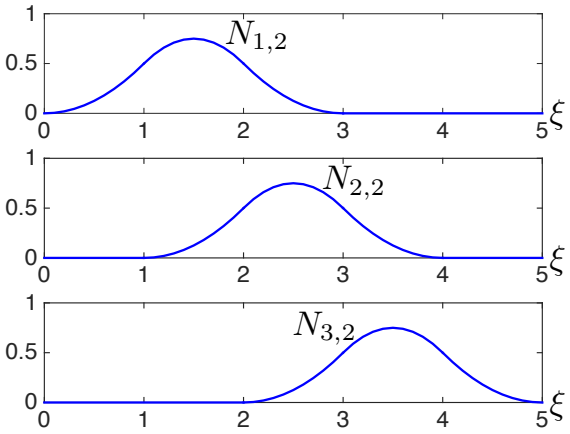

Figure 3.3: The non-zero second-degree basis functions, constructed from the knot vector $\Xi = \{0, 1, 2, 3, 4, 5\}$.

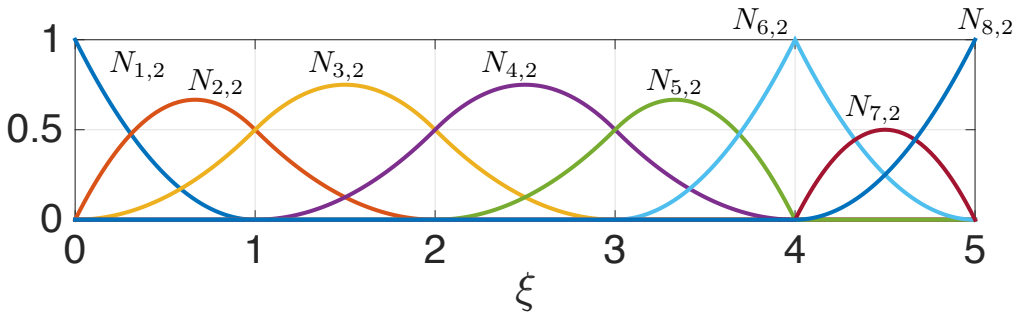

Figure 3.4: The degree 2 B-spline basis functions constructed from the open knot vector $\Xi = \{0, 0, 0, 1, 2, 3, 4, 4, 5, 5, 5\}$.

1. $N_{i,0}$ is a step function, equal to zero everywhere except on the interval $\xi \in \{\xi_i, \xi_{i+1}\}$.
2. For $p > 0$, $N_{i,p}$ is a linear combination of two $(p-1)$-degree basis functions.
3. The computation of a set of basis functions requires the specification of a knot vector Ξ, and the degree p.
4. The interval between two different knots values $\{\xi_i, \xi_{i+1}\}$ divides the parametric space into knot spans. It can have zero length when the multiplicity of the knot ξ_i appears.

Figure 3.4 shows an example of B-spline basis functions with degree 2 of an open knot vector $\Xi = \{0, 0, 0, 1, 2, 3, 4, 4, 5, 5, 5\}$. Due to the multiplicity (equal to 2) of the knot $\xi = 4$, the continuity of the B-spline basis functions at knot $\xi = 4$ is C^0. Figure 3.5 shows the first derivatives of the basis functions shown in Figure 3.4.

From the formulation of B-splines, we can list a number of important properties of the B-spline basis functions:

1. Local support property: as $N_{i,p}$ is a linear combination of two $(p-1)$-degree basis functions, $N_{i,p} = 0$ if ξ is outside the interval $\{\xi_i, \xi_{i+p+1}\}$.
   This means that higher-degree B-spline basis functions have support over much larger spans of the domain than classical FEA functions. Moreover, in the case of repeated knots, knot spans have zero measure. The number of support spans of each basis is still $p + 1$ knot spans (begins at ξ_i and ends at ξ_{i+p+1} including repeated knots).

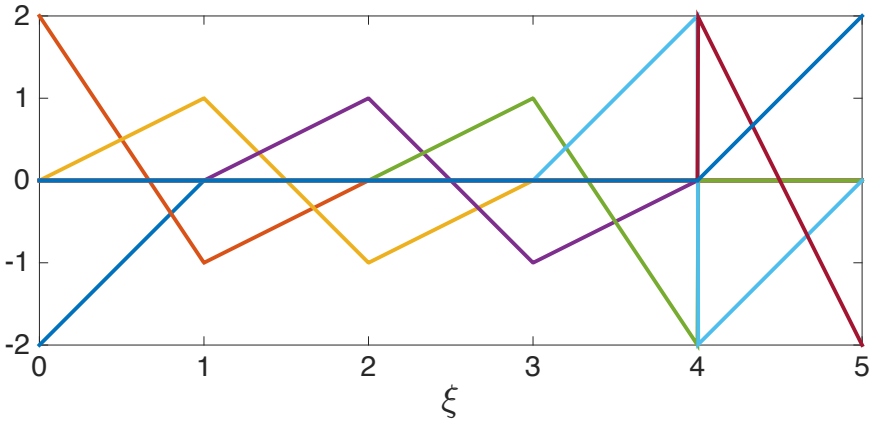

Figure 3.5: The first derivatives of the B-spline basis functions constructed from the open knot vector $\Xi = \{0, 0, 0, 1, 2, 3, 4, 4, 5, 5, 5\}$.

2. Partition of unity: for an arbitrary knot span $\{\xi_i, \xi_{i+1}\}$, $\sum_{j=i-p}^{i} N_{j,p} = 1$ for all $\xi \in \{\xi_i, \xi_{i+1}\}$.

3. All derivatives of $N_{i,p}$ exist in the knot span (see Figure 3.5). At a knot ξ_i, $N_{i,p}$ is $p - r$ times continuously differentiable, where r is the multiplicity of the knot ξ_i. Thus, increasing the degree improves continuity while increasing knot multiplicity decreases continuity.

As we see from this list of properties, the knot vector plays an important role. It not only defines a subdivision of the interval $\{\xi_i, \xi_{i+1}\}$, but also the shape of the basis functions as well as their smoothness. The high smoothness is a special feature of B-spline basis functions and distinguishes these functions from the standard C^0-continuous FEM basis functions.

Remark. For simplicity, we assume for the remainder of this thesis that the knot vector $\Xi = \{\xi_1, \xi_2, \ldots, \xi_{n+p+1}\}$ has $\xi_1 = 0$ and ξ_{n+p+1}=1.

Definition 3.1.6. Parametric space: In one dimension, the parametric space is a set of knot coordinates of a knot vector. The parametric space is defined in $\{0, 1\}$.

3.1.3 B-spline geometry

B-spline curves

A B-spline curve is defined by a linear combination of B-spline basis functions and corresponding control points. A piecewise-polynomial B-spline curve is given by:

$$C(\xi) = \sum_{i=1}^{n} N_{i,p}(\xi) B_i \tag{3.4}$$

where:

- $C(\xi)$ is the B-spline curve;
- B_i are the control points;
- $Ni, p(\xi)$ are the pth-degree B-spline basis functions.

The polygon formed by the B_i is called the control polygon.

Important properties of B-spline curves are:

1. Convex hull property: the curve is contained inside the convex hull of the control polygon.
2. In general, the B-spline curve is not interpolatory.
3. Local modification scheme: due to the local support of B-splines, moving B_i changes $C(\xi)$ only in the interval $\{\xi_i, \xi_{i+p+1}\}$.
4. Repeating a knot or control point r times decreases the number of continuous derivatives by r.
5. Affine invariance: an affine transformation is applied to the curve by applying it to the control points.
6. For open knot vectors, the first and last control points are interpolatory, that is $C(0) = B_1$ and $C(1) = B_n$. The curve is tangential to the control polygon at the start and the end of the curve.

These properties are also illustrated in Figure 3.6, where the curve constructed from the B-spline basis functions of degree $p = 2$ and knot vector:

$$\Xi = \{0, 0, 0, \frac{1}{3}, \frac{2}{3}, 1, 1, 1\}$$

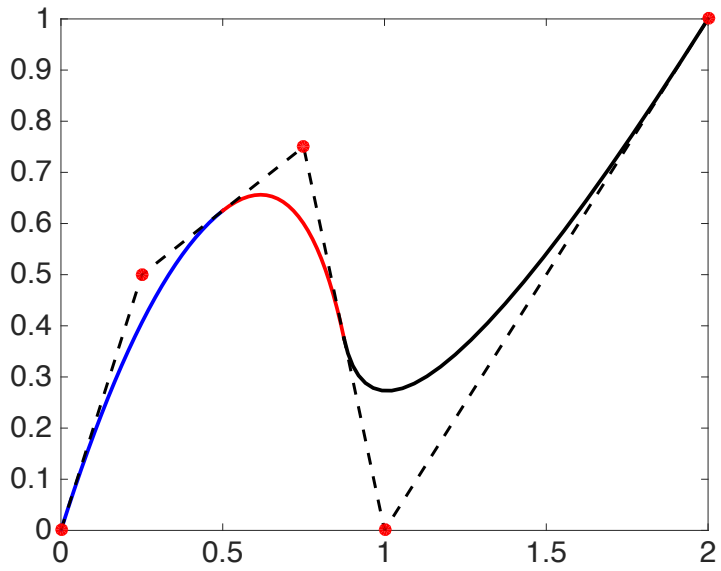

Figure 3.6: B-spline curve of degree $p = 2$ with knot vector $\Xi = \{0, 0, 0, \frac{1}{3}, \frac{2}{3}, 1, 1, 1\}$.

is represented.
The curve is interpolatory at the first and last control points, which is a general feature of a curve built from an open knot vector. According to the definition of knot spans, the curve has 3 knot spans $\{0, \frac{1}{3}\}$, $\{\frac{1}{3}, \frac{2}{3}\}$ and $\{\frac{2}{3}, 1\}$. These knot spans define 3 "elements" of the curve with different colors. With degree $p = 2$ and multiplicity r=1 at knots $\xi = \frac{1}{3}$ and $\xi = \frac{2}{3}$, the B-spline curve has C^1 continuity at the corresponding knot positions.

Figure 3.7 illustrates a B-spline curve constructed from the same knot vector $\Xi = \{0, 0, 0, \frac{1}{3}, \frac{2}{3}, 1, 1, 1\}$ but with the first control point changed. Due to the local support of B-spline basic functions, the curve position is impacted only over the blue element. With this feature, shape optimization can be performed on any part of the B-spline geometry domain by using IGA without difficulty.

B-spline surface

Given two knot vectors for each parametric direction $\Xi_1 = \{\xi_1, ..., \xi_{n_1+p_1+1}\}$ and $\Xi_2 = \{\eta_1, ..., \eta_{n_2+p_2+1}\}$, as well as a control net of points $B_{i,j}$ with i=1,..,n_1 and j=1,...,n_2, a tensor product B-spline surface is defined by taking a bidirectional control net and the two knot vectors:

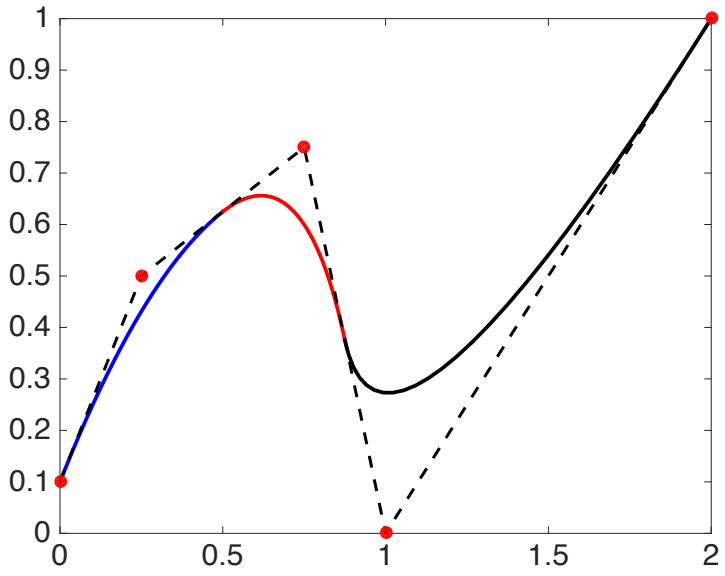

Figure 3.7: Local influence of control points on B-spline curves. The first control point is modified.

$$S(\xi,\eta) = \sum_{i=1}^{n_1}\sum_{j=1}^{n_2} N_{i,p_1}(\xi)N_{j,p_2}(\eta)B_{i,j} \tag{3.5}$$

where $N_{i,p_1}(\xi)$, $N_{i,p_2}(\xi)$ are the univariate B-spline basis functions of order p_1 and p_2 corresponding to knot vectors Ξ_1 and Ξ_2, respectively.

The bivariate B-spline basis functions are defined as:

$$N_{i,j}^{p_1,p_2}(\xi,\eta) = N_{i,p_1}(\xi)N_{j,p_2}(\eta) \tag{3.6}$$

Define a global index for the B-spline surface as:

$$A = (i-1)n + j \tag{3.7}$$

the B-spline surface can be written in a condensed form as:

$$S(\xi) = \sum_{A=1}^{n\times m} N_A^{p_1,p_2}(\xi)B_A \tag{3.8}$$

Many of the properties of a B-spline surface are the result of its tensor product:

1. The local support of the basis functions directly results from the one-dimensional functions that form them. The support of a given bivariate function is the area of $\{\xi_i, \xi_{i+p_1+1}\} \times \{\eta_j, \eta_{j+p_2+1}\}$ in the index space.

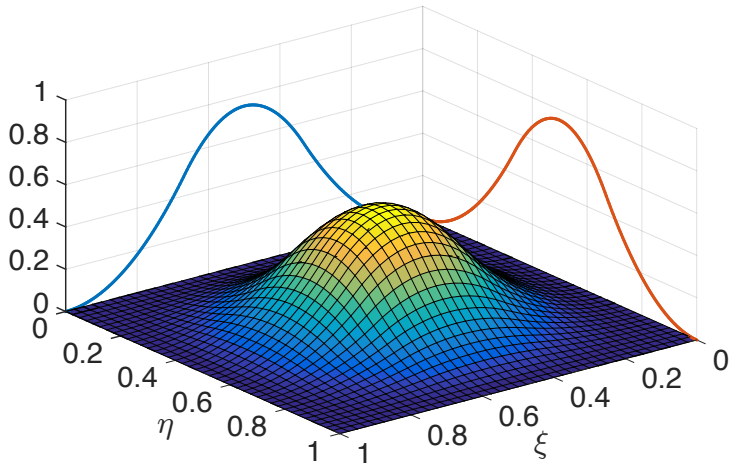

Figure 3.8: Bivariate B-spline basis function of two basis functions (blue and red) with $\Xi_1 = \{0, 0, 0, \frac{1}{3}, \frac{2}{3}, 1, 1, 1\}$ and $\Xi_2 = \{0, 0, 0, \frac{1}{3}, \frac{2}{3}, 1, 1, 1\}$.

2. Partition of unity:

$$\sum_{i=1}^{n^\xi} \sum_{j=1}^{n^\eta} N_{i,p^\xi}(\xi) N_{j,p^\eta}(\eta) = \left(\sum_{i=1}^{n^\xi} N_{i,p^\xi}(\xi) \right) \left(\sum_{j=1}^{n^\eta} N_{j,p^\eta}(\eta) \right) = 1 \tag{3.9}$$

3. The number of continuous partial derivatives in a given parametric direction is determined from the associated one-dimensional knot vectors Ξ_1 and Ξ_2, and polynomial orders p_1 and p_2.

Let us consider the two knot vectors $\Xi_1 = \{0, 0, 0, 1, 1, 1\}$ and $\Xi_2 = \{0, 0, 1, 1\}$, as well as a grid of six control points:

$$B_{1,1} = [0; 1; 4], \quad B_{2,1} = [2; 1; 4], \quad B_{3,1} = [2; 0; 1]$$

$$B_{1,2} = [0; 5; 4], \quad B_{2,2} = [4; 4; 4], \quad B_{3,2} = [4; 0; 0]$$

Together with the basis functions made by the knot vector and the control points, we can create a B-spline surface by the formula 3.5. The corresponding surface is shown in Figure 3.9.

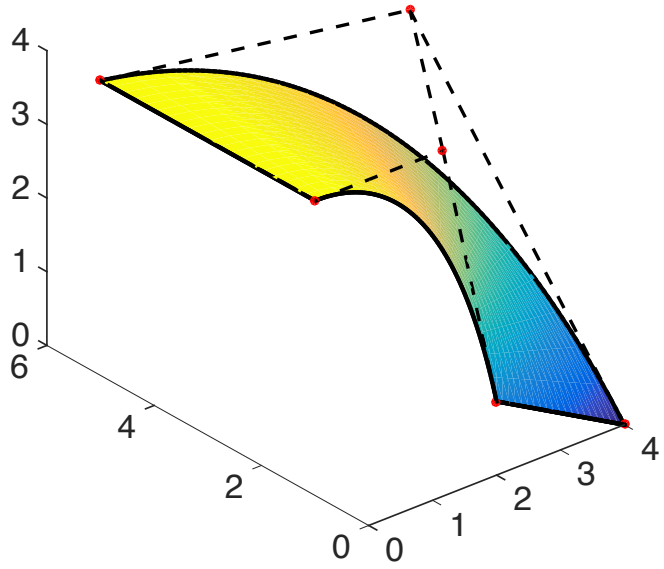

Figure 3.9: The B-spline surface of degree $[2;\ 1]$ given by the knot vectors $\Xi_1 = \{0,0,0,1,1,1\}$ and $\Xi_2 = \{0,0,1,1\}$.

B-spline volume

The extension to B-spline volume is straightforward, where a trivariate basis is formed through a tensor product of B-spline basis functions as

$$V(\xi,\eta,\mu) = \sum_{i=1}^{n_1}\sum_{j=1}^{n_2}\sum_{k=1}^{n_3} N_{i,p_1}(\xi)N_{j,p_2}(\eta)N_{k,p_3}(\mu)B_{i,j,k} \tag{3.10}$$

3.1.4 Non-Uniform Rational B-spline

NURBS basis functions

A large number of geometries can accurately be described by using the B-spline functions. However, it is not possible using only B-spline functions to represent circles in 2D. For this reason, we introduce NURBS. NURBS are commonly used in computer-aided design (CAD), manufacturing (CAM), and engineering (CAE). The term "non-uniform" refers to the knot vector which in general is not uniform. The term "rational" refers to the basis functions. While for B-spline, the basis functions are piecewise polynomials, for NURBS they are piecewise rational polynomials.

A NURBS basic functions $R_{i,p}$ is constructed from the associated set of B-spline functions $N_{i,p}(\xi)$ by introducing additional weights w_i. The univariate NURBS basis functions are defined by:

$$R_{i,p}(\xi) = \frac{w_i N_{i,p}(\xi)}{\sum_{j=1}^{n} w_j N_{j,p}(\xi)} = \frac{w_i N_{i,p}(\xi)}{W(\xi)} \tag{3.11}$$

Using NURBS in analysis often requires to know the derivatives of the basis functions. The derivative of a NURBS function is obtained by differentiating (3.11) with respect to ξ .

$$\frac{d}{d\xi} R_{i,p}(\xi) = w_i \frac{N'_{i,p}(\xi) W(\xi) - N_{i,p}(\xi) W'(\xi)}{W^2(\xi)} \tag{3.12}$$

NURBS functions inherit all positive properties of B-spline functions (local support, partition of unity, pointwise non-negativity, local linear independence,...). The important properties of NURBS are:

1. NURBS basis functions form a partition of unity.
2. The continuity and support of NURBS basis functions are the same as for B-splines.
3. Affine transformations in the physical space are obtained by applying the transformation to the control points, that is, NURBS possess the property of affine covariance.
4. If weights are equal, NURBS come down to B-spline functions.
5. NURBS surfaces and solids are the projective transformations of tensor product, piecewise polynomial entities.

Remark. B-splines can be seen as a special case of NURBS where all weights are equal. Thus, we will only use the term NURBS to refer to B-spline as well as NURBS functions in the following.

NURBS geometry

Similarly to B-spline curves, the NURBS curve is defined as the sum of control points multiplied by the respective NURBS basis functions:

$$C(\xi) = \sum_{i=1}^{n} R_{i,p}(\xi) B_i \tag{3.13}$$

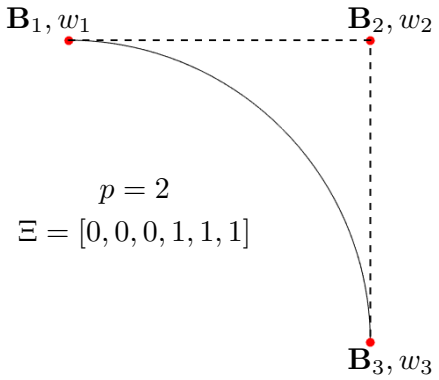

Figure 3.10: The circular arc with angle $\theta = 90^o$, constructed from control points $\mathbf{B}_1$, $\mathbf{B}_2$ and $\mathbf{B}_3$, and with $w_1 = w_3 = 1$ and $w_2 = \cos(\theta/2)$.

In order to represent a circular arc with angle θ, and from control points $\mathbf{B}_1$, $\mathbf{B}_2$ and $\mathbf{B}_3$ (with $\mathbf{B}_2$ at the intersection of tangents at both ends of the arc), weights should be set as $w_1 = w_3 = 1$ and $w_2 = \cos(\theta/2)$ (see Figure 3.10).

Rational surfaces and solids are defined analogously in terms of the rational basis functions

$$R_{i,j}^{p^\xi,p^\eta}(\xi,\eta) = \frac{w_{i,j} N_{i,p^\xi}(\xi) N_{j,p^\eta}(\eta))}{\sum_{\hat{i}=1}^{n^\xi} \sum_{\hat{j}=1}^{n^\eta} w_{\hat{i},\hat{j}} N_{\hat{i},p^\xi}(\xi) N_{\hat{j},p^\eta}(\eta)} \tag{3.14}$$

$$R_{i,j,k}^{p^\xi,p^\eta,p^\mu}(\xi,\eta,\mu) = \frac{w_{i,j,k} N_{i,p^\xi}(\xi) N_{j,p^\eta}(\eta) N_{k,p^\mu}(\mu)}{\sum_{\hat{i}=1}^{n^\xi} \sum_{\hat{j}=1}^{n^\eta} \sum_{\hat{k}=1}^{n^\mu} w_{\hat{i},\hat{j},\hat{k}} N_{\hat{i},p^\xi}(\xi) N_{\hat{j},p^\eta}(\eta) N_{\hat{k},p^\mu}(\mu)} \tag{3.15}$$

Remark. It is important to note that 2 and 3-dimensional NURBS basis functions are not tensor products of one-dimensional NURBS basis functions. They are obtained as the weighted ratio of tensor products of B-spline basis functions.

Figures 3.11 and 3.12 show the ability of NURBS in representing circular features in 2D and 3D geometries. As we can see, few elements may be used to present a complex geometry, contrary to FEM. This is the most remarkable feature of IGA.

3.2 B-spline refinement

It is regularly required to refine the model to enhance the precision of the analysis results. Hence, the refinement step is an essential operation in IGA. The basic refinement

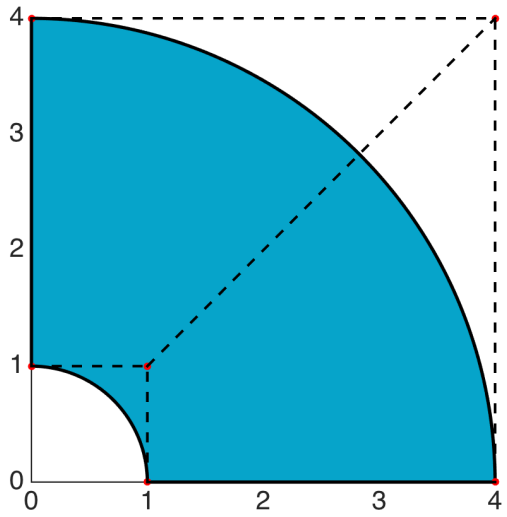

Figure 3.11: NURBS surface.

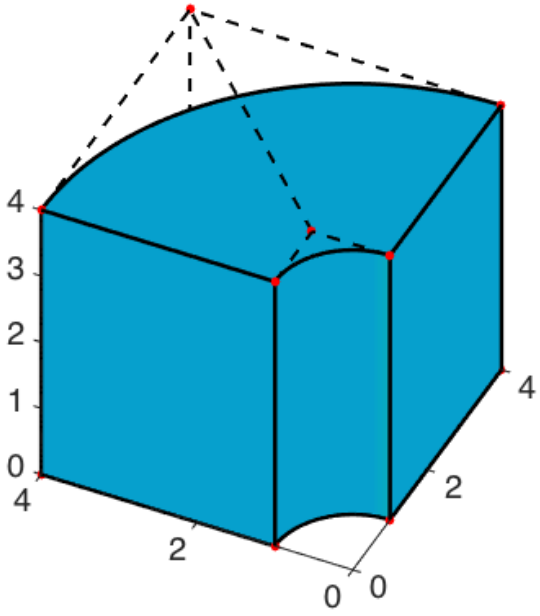

Figure 3.12: NURBS solid.

mechanism of B-spline differs from FEM, which guides to the higher richness in IGA refinement. In general, there are two kinds of refinements of B-spline function that familiar to FEM, particularly knot insertion (h-refinement), and degree elevation (p-refinement). Moreover, IGA has a more powerful k-refinement which is combined degree elevation with knot insertion. This dissertation uses the k-refinement in almost IGA linear, nonlinear numerical example as well as in error estimation.

3.2.1 Knot insertion

The first technique,called knot insertion, allows us to insert as many new knots as we wish. It is important to note that knot insertion is really just a change of vector space basis; the curve is not changed, either geometrically or parametrically. Figure 3.13 details how the mesh of the computation domain is changed after two h-refinement steps.

Knot insertion is one of the most important of all B-spline algorithms. Some of its uses are:

- Evaluating points and derivatives on curves and surfaces.
- Subdividing geometry.
- Adding more control points in order to increase flexibility in shape control.

The knot vector $\Xi_1 = \{0, 0, 0, 1, 1, 1\}$ becomes $\Xi_{1'} = \{0, 0, 0, 0.5, 1, 1, 1\}$ by inserting knot $\xi = 0.5$ for example. The number of B-spline basis functions will increase by one more function; the basis B-spline functions can be obtained by formula 3.1. The change of basis functions after knot insertion is presented in Figure 3.14 and Figure 3.15.

The new control points can be obtained by solving a system of linear equations. As the curve should not be changed, we can set

$$\sum_{i=1}^{n} N_{i,p}(\xi) B_i = \sum_{j=1}^{n+1} \overline{N}_{j,p}(\xi) \overline{B}_i \tag{3.16}$$

Inserting $\bar{\xi} \in [\xi_k, \xi_{k+1}]$, new control points are then defined as $\bar{\mathbf{B}}_i = \alpha_i \mathbf{B}_i + (1-\alpha_i)\mathbf{B}_{i-1}$ where:

$$\alpha_i = \begin{cases} 1 & \text{if } 1 \le i \le k-p \\ \frac{\bar{\xi}-\xi_i}{\xi_{i+p}-\xi_i} & \text{if } k-p+1 \le i \le k \\ 0 & \text{if } k+1 \le i \le n+p+2 \end{cases} \tag{3.17}$$

The original curve and the new curve made of degree 2 B-splines is shown in Figure 3.15. We can observe that the geometry does not change, even though the basis functions and control points are changed.

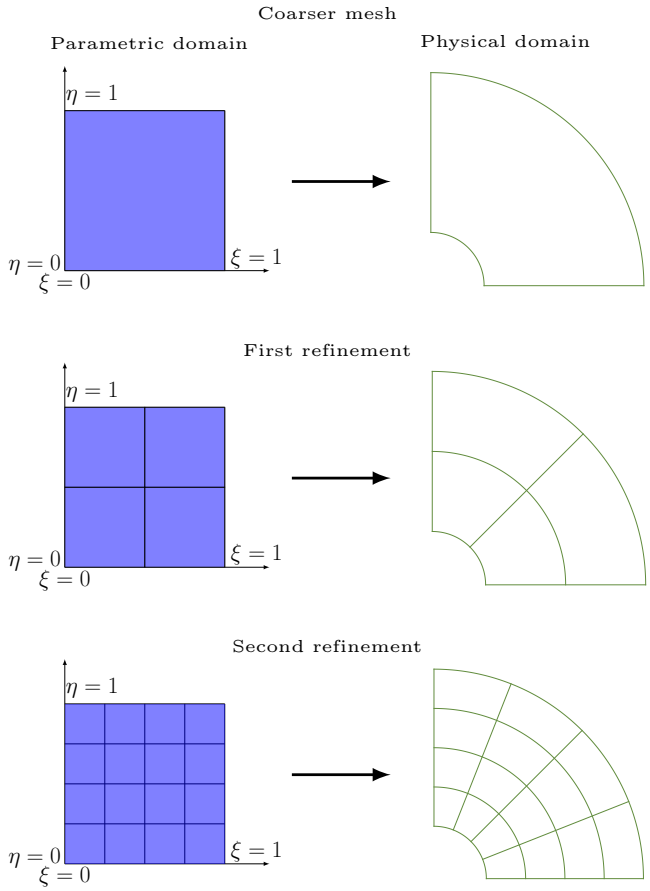

Figure 3.13: Computation domain after h-refinement.

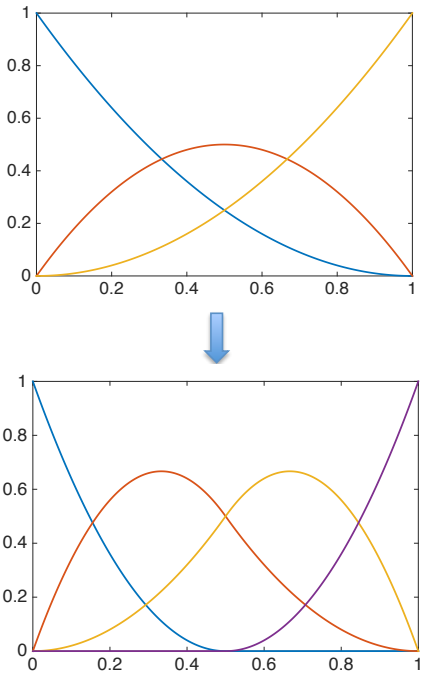

Figure 3.14: Original B-spline basis functions and new B-spline basis functions after knot insertion.

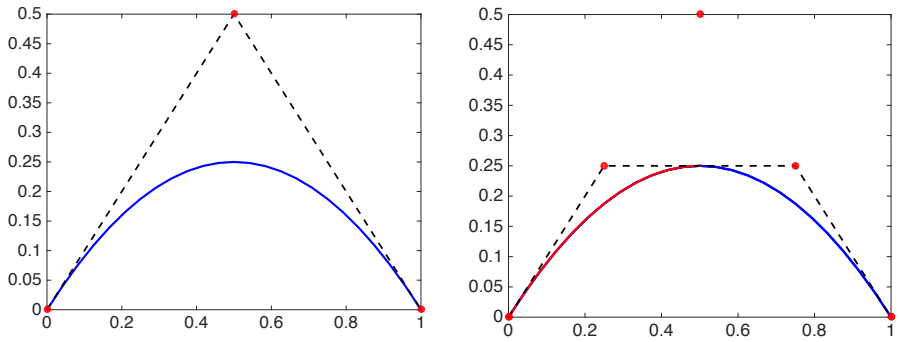

Figure 3.15: Original curve and new curve after knot insertion. There are two elements in the new curve.

Remark. Based on (3.17), only p new control points should be computed when inserting a knot.

Knot insertion has similarities with the classical h-refinement strategy in FEM due to the ability to split an original element into new elements. However, the continuity of the basis across the new element boundaries is C^{p-1}. In FEM, the continuity of the basis across element boundaries is C^0. If we insert new knot values that increase the multiplicity of existing knot values, we will decrease the continuity of the basis without creating new elements.

3.2.2 Order elevation

Order elevation is analogous to p-refinement in the conventional FEM as it increases the polynomial order of the basis. During order elevation no new knot value is added. Therefore, no new element is created and the continuity increases.

For example, we consider a degree p B-spline curve for operating the degree elevation (p-refinement). The first step of degree elevation starts by replicating existing knots until their multiplicity is equal to the polynomial order. It leads to a curve which is divided into many Bézier curves by knot insertion. Next, the degree of the polynomial is elevated on each of these individual segments to the desire degree. Lastly, excess knots are removed to combine the segments into one single degree-elevated B-spline curve.

Remark. It is important to note that each unique knot value in the knot vector must be repeated to preserve discontinuities in the pth derivative of the curve being elevated. The number of new control points depends on the multiplicities of existing knots.

Degree elevation of the Bézier curve is a process that starts with a Bézier curve of

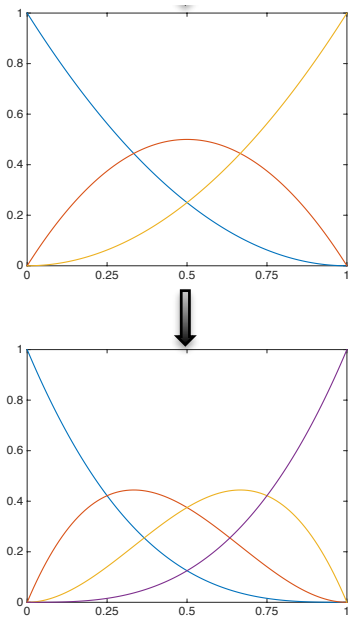

Figure 3.16: Basis functions after p-refinement.

degree p, with p+1 control points. The new Bézier curve of degree p+1 has p+2 control points. The new control points, denoted by $\bar{\mathbf{B}}_i$, are computed from original control points $\mathbf{B}_j$ as described in (3.18).

$$\begin{cases} \bar{\mathbf{B}}_0 = \mathbf{B}_0 \\ \bar{\mathbf{B}}_i = \alpha_i \mathbf{B}_{i-1} + (1-\alpha_i)\mathbf{B}_i \quad \text{if } i = 1, 2, .., p. \\ \bar{\mathbf{B}}_{p+1} = \mathbf{B}_p \end{cases} \tag{3.18}$$

with $\alpha_i = \dfrac{i}{p+1}$.
The original knot $\Xi_1 = \{0, 0, 0, 1, 1, 1\}$ will be changed in knot $\Xi_{1'} = \{0, 0, 0, 0, 1, 1, 1, 1\}$ after applying degree elevation. Figure 3.16 shows the changes in the associated B-spline basis functions.

Applying (3.18) to compute the new control points of the B-spline curve in 3.15, we have the same B-spline curve with higher degree in Figure 3.17. Comparing Figure 3.15 and Figure 3.17, we have the same curve with different control points.

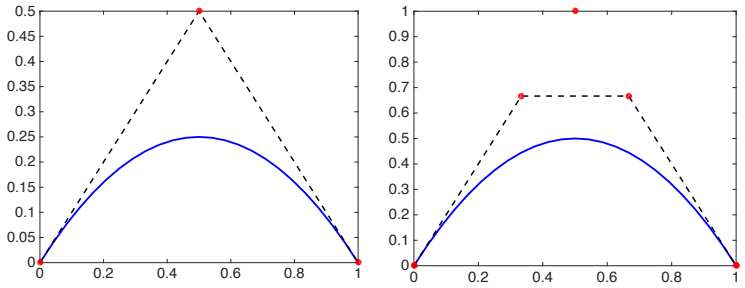

Figure 3.17: Curve after p-refinement.

3.2.3 k-refinement

The k-refinement procedure consists of degree elevation and knot insertion processes. The degree elevation and knot insertion are not commutative. Therefore, the final B-spline basis functions will change depending on whether the first refinement process is degree elevation or knot insertion. This method is very meaningful in practice because it allows to build the geometry with the desired polynomial degree in each direction.

Figure 3.18 shows the B-spline basis functions constructed from knot vector $\Xi_1 = \{0, 0, 1, 1\}$ applying k-refinement. On the left, $\Xi_1 = \{0, 0, 1, 1\}$ performs knot insertion, then degree elevation. On the right, $\Xi_1 = \{0, 0, 1, 1\}$ performs degree elevation, then knot insertion. We can observe that new B-spline basis functions have huge differences in Figure 3.18.

Figure 3.19 shows the application of k-refinement in a 2D numerical example. From the left to the right, the first figure describes the initial computation domain with 1 element and with degree 2 in the x-direction and degree 1 in the y-direction. After k-refinement, we obtain the same computation domain with 4 elements and with degree 2 in the x-direction and degree 2 in the y-direction. The continuity at the boundary of two elements is C^1. The last figure is for defining control points of local elements in the error estimation.

3.3 The IGA framework

3.3.1 Model problem

Without loss of generality in introducing the approximate framework of IGA, we consider a linear elliptic problem defined on an open bounded domain $\Omega \subset \mathbb{R}^d$ (d=1, 2 or 3 being the space dimension) with Lipschitz boundary $\partial\Omega$. We assume that prescribed

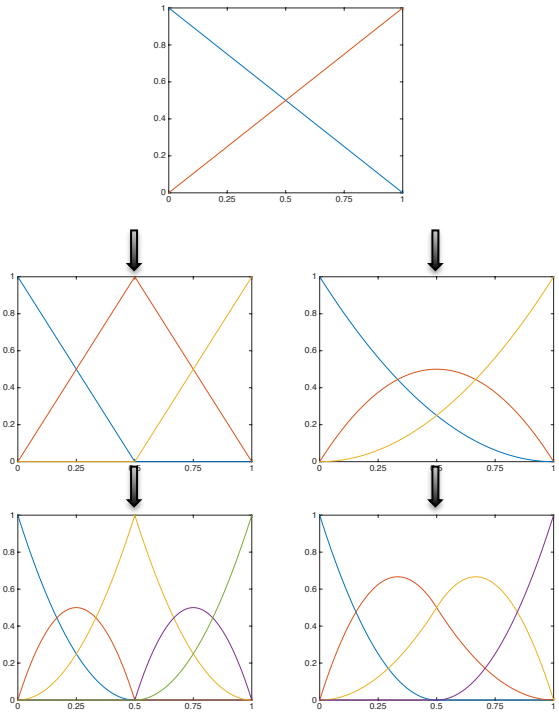

Figure 3.18: Basis functions after k-refinement.

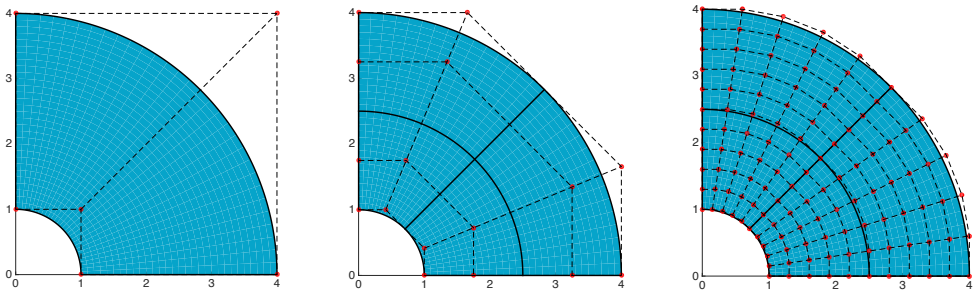

Figure 3.19: 2D element after k-refinement.

homogeneous Dirichlet boundary conditions are imposed on part $\partial_u\Omega \neq \emptyset$ of $\partial\Omega$, whereas on the complementary part $\partial_q\Omega$ of $\partial\Omega$ Neumann boundary conditions (given flux $F_d \in L^2(\partial_q\Omega)$) are applied, with $\partial_u\Omega \cap \partial_q\Omega = \emptyset$ and $\overline{\partial_u\Omega \cup \partial_q\Omega} = \partial\Omega$. A given source term $f_d \in L^2(\Omega)$ may also be active in Ω. We denote by $\mathbb{K} \in [L^\infty(\Omega)]^{d\times d}$ the diffusion matrix, assumed to be symmetric, continuous and uniformly elliptic:

$$\exists \alpha > 0, \exists \beta > 0 \quad \text{such that} \quad \alpha|\tau|^2 \leq \tau \cdot \mathbb{K}\tau \leq \beta|\tau|^2 \quad \forall \tau \in \mathbb{R}^d \tag{3.19}$$

The reference mathematical problem consists in finding u (and associated flux $\mathbf{q} = \mathbb{K}\nabla u$) solution to the following system of equations:

$$\begin{cases} -\nabla.\mathbb{K}\nabla u = f_d & in \quad \Omega \\ n.\mathbb{K}\nabla u = F_d & on \quad \Gamma_N \\ u = 0 & on \quad \Gamma_D \end{cases} \tag{3.20}$$

$\mathbf{n}$ denoting the unit outgoing normal vector to Ω. Introducing the functional space $\mathcal{U} = H_0^1(\Omega) = \{v \in H^1(\Omega), v_{|\partial_u\Omega} = 0\}$, the weak formulation of the problem reads:

$$\text{Find } u \in \mathcal{U} \text{ such that } a(u,v) = l(v) \quad \forall v \in \mathcal{U} \tag{3.21}$$

where bilinear form $a(\cdot,\cdot)$ and linear form $l(\cdot)$ are defined as:

$$a(u,v) = \int_\Omega \mathbb{K}\nabla u \cdot \nabla v d\Omega \quad l(v) = \int_\Omega f_d v d\Omega + \int_{\partial_q\Omega} F_d v dS \tag{3.22}$$

From the previous assumptions, and referring to the Lax-Milgram theorem, we claim that the reference problem (6.23) has a unique solution. The solution u to the previous mathematical model is the reference when dealing with discretization error.

We define the energy norm $\|u\|_\mathbb{K} = \sqrt{a(u,u)}$ which is equivalent to the H^1-norm in $\mathcal{U}$. This norm will be preferred to the classical residual norm in order to define a measure of the global discretization error, as it is directly linked to the properties of the problem/operator.

The approximation of the solution u can be written in terms of NURBS basis functions as:

$$u = \sum_{i=1}^{n} N_i B_i \tag{3.23}$$

The test function v is discretized as:

$$v = \sum_{j=1}^{n} N_j C_j \tag{3.24}$$

Substituting (3.23) and (3.24) into (6.23) and noticing that the set of values $\{C_j\}$ is arbitrary, the discrete form is now written as

$$\sum_{i=1}^{n} B_i \sum_{j=1}^{n} \int_{\Omega} \mathbb{K} \nabla N_i \cdot \nabla N_j d\Omega = \int_{\Omega} f_d N_j dx + \int_{\partial_q \Omega} F_d N_j dS \tag{3.25}$$

By defining the left-hand side and right-hand side of (3.25) as:

$$K = \sum_{i=1} \sum_{j=1}^{n} \int_{\Omega} \mathbb{K} \nabla N_i \cdot \nabla N_j d\Omega \tag{3.26}$$

$$F = \int_{\Omega} f_d N_j dx + \int_{\partial_q \Omega} F_d N_j dS \tag{3.27}$$

the system to solve is expressed in matrix notation as

$$KB = F \tag{3.28}$$

where:

- K is the stiffness matrix,
- B is the displacement vector,
- F is the loading vector.

3.3.2 IGA code architecture

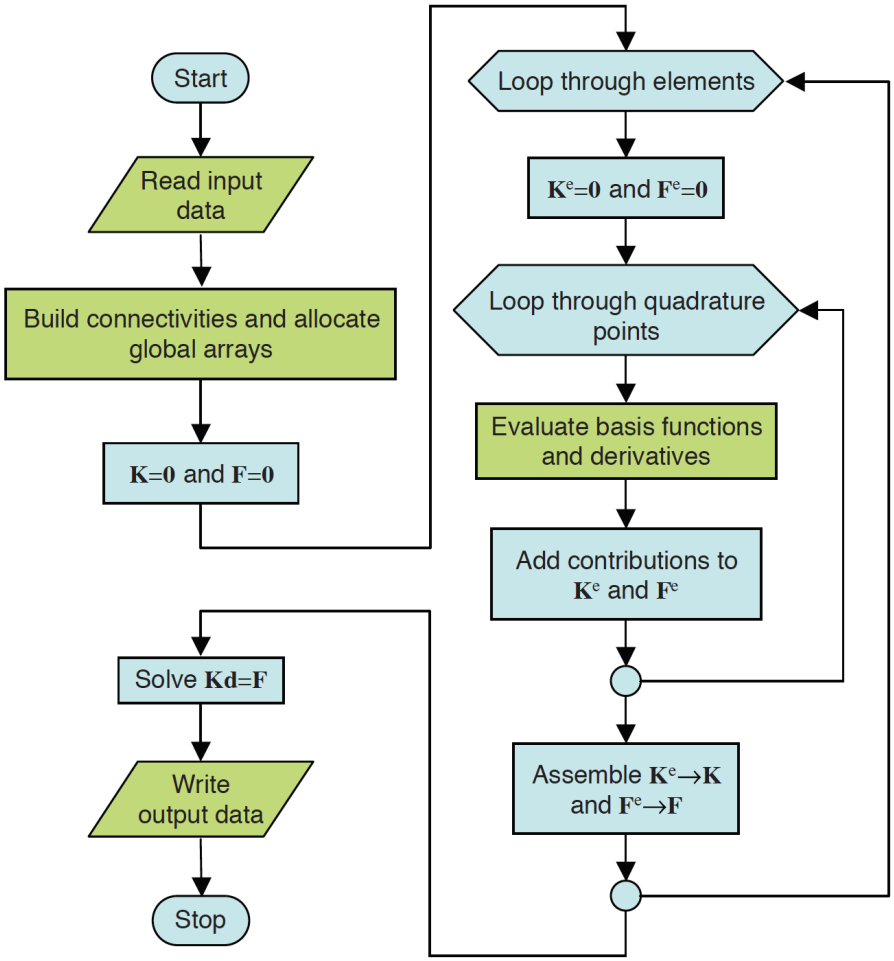

Figure 3.20: Flowchart of a classical finite element code to solve (3.28). Such a code can be converted to a single-patch isogeometric analysis code by replacing the routines shown in green.

The equation 3.28 of IGA is similar to FEM. Thus, we can adjust the architecture of a classical FEA code to be used for IGA. Input data and connection between elements depend on the specific element technology. It leads to the difference of this step. Next, the basis functions must be updated to evaluate the NURBS functions. Lastly, the format of the output will be specific to the NURBS basis.

3.3.3 Similarities and differences between IGA and FEA

Throughout our discussion on NURBS, we have made comparisons with classical FEA functions and geometries. These are summarized below.

Table 3.1: Differences between isogeometric analysis and finite element analysis

Isogeometric analysis	Finite element analysis
Exact geometry	Approximate geometry
Control points	Nodal points
Control variables	Nodal variables
NURBS basis	Polynomial basis
High, easily controlled continuity	C^0-continuity, always fixed
hpk-refinement space	hp-refinement space

Table 3.2: Common features shared by isogeometric analysis and finite element analysis

Isogeometric analysis and finite element analysis
Galerkin's method
Code architecture
Compactly supported basis
Partition of unity
Affine covariance

3.4 Mapping in IGA

In practice, integrals are computed using a Gaussian quadrature to calculate the stiffness matrix and loading vector. Figure 3.21 shows the element Ω^e in the physical space, the element $\hat{\Omega}^e$ in the parametric space and parent element Ω^e. The physical element Ω^e is pulled back first to the parametric space by the geometrical mapping, then through a second mapping to the parent element. The parent element has a constant area and is where the integration is performed, with easier exploitation of the Gaussian quadrature (isoparametric formulation).

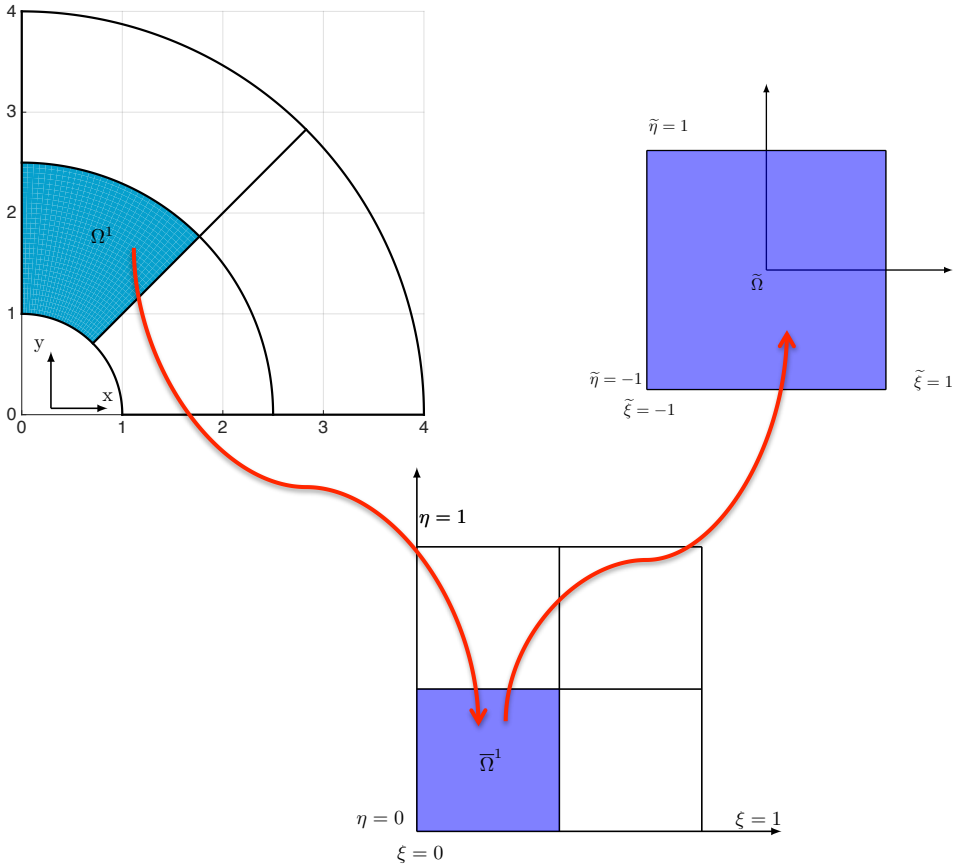

Figure 3.21: Mapping in IGA.

3.4.1 Index space

Index space is formed through the specified knot vectors by giving each knot value a distinct coordinate including the repeated knots. As an example, consider a NURBS patch defined through bivariate NURBS basis functions with knot vectors $\Xi_1 = \{0, 0, 0, 0.5, 1, 1, 1\}$ and $\Xi_2 = \{0, 0, 0, 0.5, 1, 1, 1\}$ in each of the parametric directions ξ,η. This will form the index space as illustrated in Figure 3.22. By equally spacing each of the knots in the plot, it is easy to see exactly which knot spans each of the functions are supported in, including where they overlap. The color area indicates a non-zero knot span.

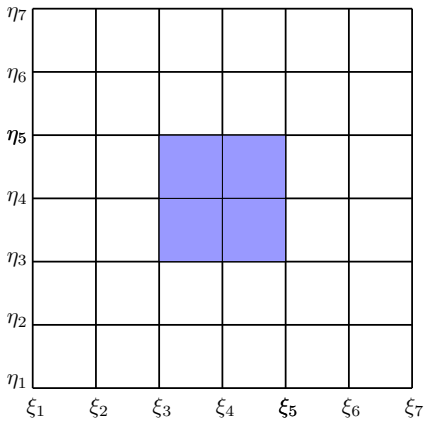

Figure 3.22: Index space.

3.4.2 Parametric space

The parametric space is formed by considering only the non-zero intervals between knot values. For the knot vectors considered previously, the parametric space is illustrated in Figure 3.23. It is clear that we only have four non-trivial elements (elements with positive measure), and therefore only four elements in which calculations need to be performed during analysis. We define the parametric space with the associated set of parametric coordinates $\{\xi, \eta\}$. Knot lines provide a natural definition of element boundaries.

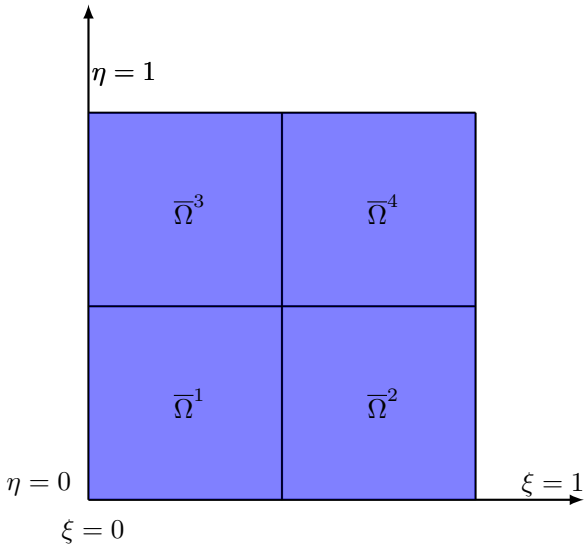

Figure 3.23: Parametric space.

3.4.3 Physical space

The physical space is where the actual geometry is represented by a linear combination of the basis functions and the control points. The basis functions are usually not interpolating the control points.

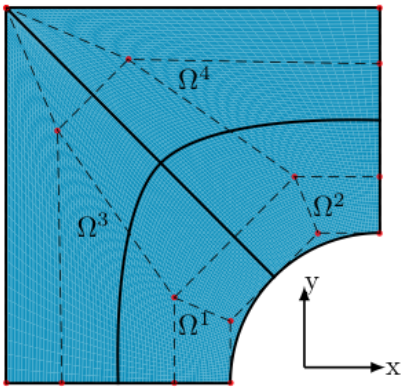

Figure 3.24: Physical space.

The physical space enables the geometrical representation of Ω; it consists in giving control points $\mathbf{B}_i$ defined by space coordinates in the real space and associated weight

w_i in order to attract more or less the curve to coincide with geometry. A geometrical mapping $\mathbf{F}$ thus transforms coordinates of the parametric space to the physical space Ω, and conversely. Figure 3.24 describes a 2D NURBS surface defined for knot vectors $\Xi_1 = \{0, 0, 0, 0.5, 1, 1, 1\}$ and $\Xi_2 = \{0, 0, 0, 0.5, 1, 1, 1\}$. The element boundaries correspond to the black curves.

3.4.4 Control mesh

The control mesh (or net) is defined by the control points. The control mesh interpolates all control points. It controls the geometry, but does generally not coincide with the physical mesh. The control variables are located at the control points and are the degrees of freedom of the problem. The control mesh may be severely distorted while the physical geometry still remains well defined.

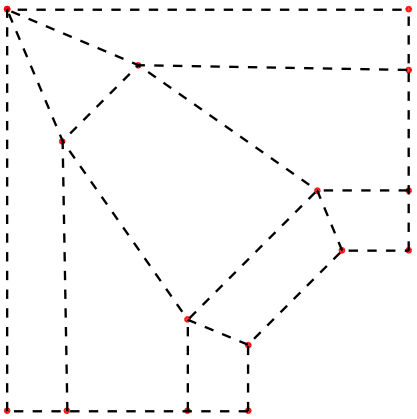

Figure 3.25: Control net corresponding to the physical space of Figure 3.24.

Chapter 4

Error estimation in the IGA using the concept of CRE for linear mechanics problems

Contents

4.1 Introduction of the CRE concept 64
4.1.1 Definition of CRE 64
4.1.2 CRE properties 66
4.1.3 Goal-oriented error estimation 67
4.2 Construction of an admissible flux field 69
4.2.1 General hybrid-flux technique 69
4.2.2 Technical implementation on a 2D example 72
4.3 Numerical examples 78
4.3.1 Example 1: thermal problem on a quarter of an annulus . . . 78
4.3.2 Example 2: elasticity problem on a L-shape domain 89
4.3.3 Example 3: elasticity problem on a 3D structure 92
4.4 Conclusion 94

4.1 Introduction of the CRE concept

4.1.1 Definition of CRE

The definition of the error in IGA is closely connected to the definition of the notion of approximate solution. The key idea of the Constitutive Relation Error (CRE) concept comes from a mechanical point of view. An approximation (u_h, σ_h) of the exact pair (u, σ), computed from IGA or FEA, has a stress component that does not verify the equilibrium equation. The difficult part is to develop admissible approximate solutions which satisfy the conditions of admissibility exactly. The construction process of admissible approximate solutions in the CRE concept, explained in full details in [LP05], has similitudes with various methods in the literature such as equilibrated residual [AO97] or flux-free [PDH06, CDH09] approaches. They all share the approach of constructing a fully equilibrated dual field, which is actually the only way to recover guaranteed and fully computable error estimates in the energy norm.

Let us recall the FEM (or IGA) model problem to use unique notations when writing CRE formula. We consider for this a scalar (e.g. thermal) elliptic problem. The problem consists in finding u (with associated flux $\mathbf{q} = \mathbb{K}\nabla u$) solution to the following system of equations:

$$\begin{aligned} -\nabla \cdot (\mathbb{K}\nabla u) &= f_d \quad \text{in } \Omega \\ u &= 0 \quad \text{on } \partial_u \Omega \\ \mathbb{K}\nabla u \cdot \mathbf{n} &= F_d \quad \text{on } \partial_q \Omega \end{aligned} \tag{4.1}$$

$\mathbf{n}$ denoting the unit outgoing normal vector to Ω.

Introducing the functional space $\mathcal{U} = H_0^1(\Omega) = \{v \in H^1(\Omega), v_{|\partial_u \Omega} = 0\}$, the weak formulation of the problem reads:

$$\text{Find } u \in \mathcal{U} \text{ such that } a(u, v) = l(v) \quad \forall v \in \mathcal{U} \tag{4.2}$$

In the framework of the FEM method, the displacement field plays a special role and the error is defined as the difference between the exact displacement field and the FEM displacement field.

$$e_h = u - u_h \tag{4.3}$$

We highlight the constitutive relation for the heat flux

$$\mathbf{q} = \mathbb{K}\nabla u \tag{4.4}$$

where $\mathbb{K}$ designates the heat operator of the material. From this definition, one can deduce an error in the heat fluxes term:

$$\mathbf{q} - \mathbf{q}_h = \mathbb{K}\nabla e_h \tag{4.5}$$

A major drawback of this approximation approach from a mechanical point of view is that the heat flux part $\mathbf{q}_h$ of the approximation does not verify the equilibrium equations. This observation is at the root of the introduction of the notion of error in constitutive relation (CRE) [LP05]. The critical part of CRE concept is to improve approximate solutions to meet the conditions of admissibility precisely.

For the considered problem, it applies to a so-called admissible solution $(\hat{u}, \hat{\mathbf{q}}) \in \mathcal{U} \times \mathcal{S}$ satisfying boundary conditions and balance equations. The functional space $\mathcal{S}$ is defined as:

$$\mathcal{S} = \{\tau \in H(div, \Omega), \int_\Omega \tau \cdot \nabla v \mathrm{dx} = \int_\Omega f_d v \mathrm{dx} + \int_{\partial_q \Omega} F_d v \mathrm{dS}\} \tag{4.6}$$

with $H(div, \Omega) = \{\tau \in [L^2(\Omega)]^d, \nabla \cdot \tau \in L^2(\Omega)\}$.

Definition 4.1.1. Error in constitutive relation associated with the admissible pair $(\hat{u}, \hat{\mathbf{q}})$: It is the quantity defined at all points of the domain Ω by:

$$e_{CRE} = \hat{\mathbf{q}} - \mathbb{K}\nabla\hat{u} \tag{4.7}$$

The error in constitutive relation is measured using the energy norm:

$$E^2_{CRE}(\hat{u}, \hat{\mathbf{q}}) = \int_\Omega (\hat{\mathbf{q}} - \mathbb{K}\nabla\hat{u})\mathbb{K}^{-1}(\hat{\mathbf{q}} - \mathbb{K}\nabla\hat{u})\mathrm{dx} = \|\hat{\mathbf{q}} - \mathbb{K}\nabla\hat{u}\|^2_{\mathbb{K}^{-1}} \tag{4.8}$$

where $\|\cdot\|_{\mathbb{K}^{-1}}$ is the energy norm in terms of flux over Ω.

The calculation of the CRE cannot be made directly on the pair $(u_h, \mathbf{q}_h)$ because this pair is not admissible. It is necessary to post-process the FEM solution in order to construct an admissible displacement-heat flux pair $(\hat{u}_h, \hat{\mathbf{q}}_h)$. The displacement field u_h is admissible. Therefore, for the sake of simplicity, we generally choose:

$$\hat{u}_h = u_h \tag{4.9}$$

The heat flux part $\mathbf{q}_h$ of the approximation is not statically admissible. The basic idea consists in seeking a field $\hat{\mathbf{q}}_h$ as a prolongation of the FEM solution The construction of an equilibrated heat flux field $\hat{\mathbf{q}}_h$ is carried out in two stages in classical FEA. First, one constructs force densities F on the element edges over the mesh. The purpose of these densities is to represent the heat flux vectors on the element sides. In the second stage, a simple solution is obtained by solving a local problem on each element K.

Definition 4.1.2. Strong prolongation condition: For any basic function φ_i and for any element K of the mesh, the condition reads:

$$\int_K (\hat{\mathbf{q}}_h - \mathbf{q}_h) \cdot \nabla \varphi_i \mathrm{dx} = 0 \tag{4.10}$$

Remark. The prolongation condition 4.10 has a strong mechanical content. It requires that heat fluxes $\hat{\mathbf{q}}_h$ and $\mathbf{q}_h$ yield the same work in each element when associated with kinematic field φ_i.

4.1.2 CRE properties

The relationship between the error in the solution and the error in constitutive relation is given by the popular Prager-Synge theorem. The Prager-Synge equality [PS47] then links the CRE measure E_{CRE} to a global measure (energy norm over the domain Ω) of the discretization error between u and $\hat{u}$:

$$E_{CRE}^2(\hat{u}, \hat{\mathbf{q}}) = \|\mathbf{q} - \hat{\mathbf{q}}\|_{\mathbb{K}^{-1}}^2 + \|\mathbf{q} - \mathbb{K}\nabla\hat{u}\|_{\mathbb{K}^{-1}}^2 \geq \|\mathbf{q} - \mathbb{K}\nabla\hat{u}\|_{\mathbb{K}^{-1}}^2 = \|u - \hat{u}\|_{\mathbb{K}}^2 \tag{4.11}$$

Choosing $\hat{u} = u_h \in \mathcal{U}$, the CRE measure thus defines a strict and fully computable bound on the global error between u and its approximation u_h.

When introducing as the approximate heat flux the average of the finite element heat flux and the admissible heat flux:

$$\hat{\mathbf{q}}^* = \frac{1}{2}[\hat{\mathbf{q}} + \mathbb{K}\nabla\hat{u}] \tag{4.12}$$

an extension of the Prager-Synge equality can be derived:

$$E_{CRE}^2(\hat{u}, \hat{\mathbf{q}}) = 4\|\mathbf{q} - \hat{\mathbf{q}}^*\|_{\mathbb{K}^{-1}}^2 \tag{4.13}$$

The measure of the error in constitutive relation enables one to calculate the error between $\mathbf{q}$ and $\hat{\mathbf{q}}$ exactly, in the sense of the energy norm, without knowing the exact solution $\mathbf{q}$. This last relation is practically used for goal-oriented error estimation. The practical construction of $\hat{\mathbf{q}}$ for IGA is the topic of Section 5.4.1.

Remark. An alternative to (4.11), when considering flux fields $\mathbf{z} \in H(\Omega, div)$ alone and $\partial_u\Omega = \partial\Omega$, reads:

$$\|\mathbf{q} - \mathbb{K}\nabla\hat{u}\|_{\mathbb{K}^{-1}} \leq \|\mathbf{z} - \mathbb{K}\nabla\hat{u}\|_{\mathbb{K}^{-1}} + C_\Omega\|div\mathbf{q} + f_d\| \tag{4.14}$$

where C_Ω is the constant in the Friedrich's type inequality (which depends on matrix $\mathbb{K}$ and domain Ω, but not on the mesh). This inequality was used in [KT15] for a posteriori error estimation in IGA simulations; the recovery of $\mathbf{z} \in H(\Omega, div)$ (i.e. not fully equilibrated with the external loading contrary to $\hat{\mathbf{q}} \in \mathcal{S}$) is quite simple due to the regularity of IGA basis functions, but the inequality requires the evaluation of a constant which may lead to large over-estimations in the general case.

Remark. The CRE functional can also be defined by means of dual potentiels (in the Legendre-Fenchel sense). Indeed, introducing the dual potentials $\psi(\nabla v) = \frac{1}{2}\nabla v \cdot \mathbb{K}\nabla v$ and $\psi^*(\tau) = \frac{1}{2}\tau \cdot \mathbb{K}^{-1}\tau$, we get:

$$E^2_{CRE}(\hat{u}, \hat{\mathbf{q}}) = 2\int_\Omega (\psi(\nabla \hat{u}) + \psi^*(\hat{\mathbf{q}}) - \hat{\mathbf{q}} \cdot \nabla \hat{u})\mathrm{d}\mathbf{x} \tag{4.15}$$

This formulation using potentials is general and enables to define the CRE estimate for nonlinear models (see Chapter 6).

4.1.3 Goal-oriented error estimation

The error measured in a global (energy) norm is clearly not the best criterion for control and adaptivity when one is interested in specific outputs of interest of the problem. Therefore, goal-oriented error estimates may be derived. Following the classical extraction (adjoint-based) technique [PP97, PO99, BR01] and the CRE concept, we can easily get error bounds on outputs.
We consider a functional output of interest Q, linear with respect to u, defined globally by means of an extraction pair $\mathbf{q}_\Sigma$ and f_Σ :

$$Q(u) = \int_\Omega (\mathbf{q}_\Sigma \cdot \nabla u + f_\Sigma u)\mathrm{d}\mathbf{x} \tag{4.16}$$

Functions $\mathbf{q}_\Sigma$ and f_Σ, referred to as extraction operators or extractors, may be defined explicitly or implicitly (depending on the quantity Q). Then, we define the adjoint problem that consists here (self-adjoint operator) in finding $\tilde{u}$ (and $\tilde{\mathbf{q}} = \mathbb{K}\nabla\tilde{u}$) such that:

$$a(v, \tilde{u}) = a(\tilde{u}, v) = Q(v) \quad \forall v \in \mathcal{U} \tag{4.17}$$

Computing an approximate adjoint solution $(\tilde{u}_h, \tilde{\mathbf{q}}_h = \mathbb{K}\nabla\tilde{u}_h)$ with IGA (and possibly different discretization parameters), then recovering an admissible heat flux field $\hat{\tilde{\mathbf{q}}}_h$ such that:

$$\int_\Omega \hat{\tilde{\mathbf{q}}}_h \cdot \nabla v \mathrm{d}\mathbf{x} = \int_\Omega (\mathbf{q}_\Sigma \cdot \nabla v + f_\Sigma v)\mathrm{d}\mathbf{x} \quad \forall v \in \mathcal{U} \tag{4.18}$$

we get:

$$\begin{aligned} Q(u) - Q(u_h) = a(u - u_h, \tilde{u}) &= \int_\Omega \nabla(u - u_h) \cdot \tilde{\mathbf{q}} \mathrm{dx} \\ &= \int_\Omega \nabla(u - u_h) \cdot \hat{\tilde{\mathbf{q}}}_h \mathrm{dx} \\ &= \int_\Omega \nabla(u - u_h) \cdot (\hat{\tilde{\mathbf{q}}}_h - \mathbb{K}\nabla\tilde{u}_h)\mathrm{dx} + \int_\Omega \nabla(u - u_h) \cdot \mathbb{K}\nabla\tilde{u}_h \mathrm{dx} \\ &= \int_\Omega \nabla(u - u_h) \cdot (\hat{\tilde{\mathbf{q}}}_h - \tilde{\mathbf{q}}_h)\mathrm{dx} + \int_\Omega (\hat{\mathbf{q}}_h - \mathbf{q}_h) \cdot \nabla\tilde{u}_h \mathrm{dx} \end{aligned} \tag{4.19}$$

so that

$$|Q(u) - Q(u_h) - Q_{corr,1}| \leq \|\mathbf{q} - \mathbf{q}_h\|_{\mathbb{K}^{-1}} . \|\hat{\tilde{\mathbf{q}}}_h - \tilde{\mathbf{q}}_h\|_{\mathbb{K}^{-1}} \leq E_{CRE}(u_h, \hat{\mathbf{q}}_h) . E_{CRE}(\tilde{u}_h, \hat{\tilde{\mathbf{q}}}_h) \tag{4.20}$$

where $Q_{corr,1} = \int_\Omega (\hat{\mathbf{q}}_h - \mathbf{q}_h) \cdot \nabla\tilde{u}_h \mathrm{dx}$ is a fully computable correction term. An improved bounding can be obtained introducing fluxes $\hat{\mathbf{q}}_h^*$ and $\hat{\tilde{\mathbf{q}}}_h^*$. Indeed, starting from (4.19), we get:

$$\begin{aligned} Q(u) - Q(u_h) - Q_{corr,1} &= \int_\Omega (\mathbf{q} - \mathbf{q}_h) \cdot \mathbb{K}^{-1}(\hat{\tilde{\mathbf{q}}}_h - \tilde{\mathbf{q}}_h)\mathrm{dx} \\ &= \int_\Omega (\mathbf{q} - \hat{\mathbf{q}}_h^*) \cdot \mathbb{K}^{-1}(\hat{\tilde{\mathbf{q}}}_h - \tilde{\mathbf{q}}_h)\mathrm{dx} + \int_\Omega (\hat{\mathbf{q}}_h^* - \mathbf{q}_h) \cdot \mathbb{K}^{-1}(\hat{\tilde{\mathbf{q}}}_h - \tilde{\mathbf{q}}_h)\mathrm{dx} \end{aligned} \tag{4.21}$$

so that

$$|Q(u) - Q(u_h) - Q_{corr,2}| \leq \|\mathbf{q} - \hat{\mathbf{q}}_h^*\|_{\mathbb{K}^{-1}} . \|\hat{\tilde{\mathbf{q}}}_h - \tilde{\mathbf{q}}_h\|_{\mathbb{K}^{-1}} = \frac{1}{2} E_{CRE}(u_h, \hat{\mathbf{q}}_h) . E_{CRE}(\tilde{u}_h, \hat{\tilde{\mathbf{q}}}_h) \tag{4.22}$$

with $Q_{corr,2} = Q_{corr,1} + \int_\Omega (\hat{\mathbf{q}}_h^* - \mathbf{q}_h) \cdot \mathbb{K}^{-1}(\hat{\tilde{\mathbf{q}}}_h - \tilde{\mathbf{q}}_h)\mathrm{dx} = \int_\Omega (\hat{\mathbf{q}}_h - \mathbf{q}_h) \cdot \mathbb{K}^{-1}\hat{\tilde{\mathbf{q}}}_h^* \mathrm{dx}$.

In practice, accurate bounds are obtained by a local enrichment of the adjoint solution alone. Outside local mesh refinement, a non-intrusive approach, henceforth known as handbook technique, can be introduced for the approximate solution of the adjoint problem [CL08, LP10, WC12]. Noticing that the adjoint loading $(\mathbf{q_q}, f_\mathbf{q})$ usually applies on a local subdomain of Ω, and therefore leads to an adjoint solution with localized high gradients (Saint-Venant principle), the idea is to introduce local enrichment functions in the vicinity of the space region of interest where the quantity Q is defined. This enrichment is particularly well-suited to handle pointwise quantities of interest and yields accurate local error bounds without requiring any regularization (e.g. mollification [PO99]) of the functional being considered or any specific local remeshing technique.

4.2 Construction of an admissible flux field

We detail in this section a procedure that enables to recover a relevant admissible flux field $\hat{\mathbf{q}}_h \in \mathcal{S}$ from a post-processing of the approximate IGA flux field $\mathbf{q}_h$ at hand, and using conventional tools available in commercial software. This procedure essentially follows the same principles as the hybrid-flux (or EET) technique developed in the FEA context [LL83, LM96, PCL11, RGR14]. Nevertheless, as IGA shape functions φ_I are associated with non-interpolating control points I (instead of physical nodes in FEA), and may be supported by a large number of knot spans (compared to FEA where the support of the shape function φ_I associated to node I is made of elements connected to this node alone), the EET technique requires specific modifications.

4.2.1 General hybrid-flux technique

The proposed procedure for the recovery of $\hat{\mathbf{q}}_h \in \mathcal{S}$ in the IGA context uses weak equilibration properties (5.4) of the IGA approximate flux field $\mathbf{q}_h = \mathbb{K}\nabla u_h \notin \mathcal{S}$ at hand. It involves local independent computations on (non-zero) knot spans Ω^e in the physical space, associated with tensorized regular (line, rectangle, parallelepiped) knot spans $\hat{\Omega}^e$ in the parametric space (see Section 3.4.2). Indeed, after defining an equilibrated traction field $\hat{F}^e$ on the boundary $\partial\Omega^e$ of each knot span Ω^e, the following Neumann problems are solved at the knot span level:

$$-\nabla\cdot\hat{\mathbf{q}}_h = f_d \quad \text{in } \Omega^e \quad ; \quad \hat{\mathbf{q}}_h\cdot\mathbf{n}^e = \hat{F}^e \quad \text{on } \partial\Omega^e \tag{4.23}$$

$\mathbf{n}^e$ being the unit outgoing normal vector to Ω^e. The recovery procedure is thus split in two steps which are detailed below.

Step 1: computation of equilibrated tractions on the boundary of knot spans

For each knot span Ω^e, equilibrated tractions $\hat{F}^e_\Gamma$ are computed on each edge/face Γ of $\partial\Omega^e$. These tractions should be such that:

$$\begin{aligned} &\hat{F}^e_\Gamma = F_d \quad \text{if } \Gamma\subset\partial_q\Omega \quad \textit{(satisfaction of Neumann boundary conditions)} \\ &\int_{\Omega^e} f_d \mathrm{d}\mathbf{x} + \sum_{\Gamma\subset\partial\Omega^e}\int_\Gamma \hat{F}^e_\Gamma \mathrm{d}S = 0 \quad \forall\Omega^e \quad \textit{(satisfaction of equilibrium at the knot span level)} \end{aligned} \tag{4.24}$$

Furthermore, in order to ensure continuity of the normal admissible flux between knot spans, tractions are defined as $\hat{F}^e_\Gamma = \eta^e_\Gamma\hat{F}_\Gamma$ with $\eta^e_\Gamma = \pm 1$ and $\hat{F}_\Gamma$ a traction field specific to the edge/face Γ.

A key point to compute tractions $\hat{F}_\Gamma^e$ is the so-called prolongation condition, which is a local energy relation between the IGA field $\mathbf{q}_h$ and the recovered equilibrated field $\hat{\mathbf{q}}_h$. Denoting again by $\{\varphi_I\}_{1\leq I\leq N}$ the set of IGA basis functions (B-Splines or NURBS), the prolongation condition reads:

$$\int_{\Omega^e}(\hat{\mathbf{q}}_h-\mathbf{q}_h)\cdot\nabla\varphi_I\mathrm{d}\mathbf{x}=0\quad\forall\varphi_I,\forall\Omega^e \tag{4.25}$$

Using local properties (4.23) as well as the divergence theorem, (4.25) comes down to:

$$\sum_{\Gamma\subset\partial\Omega^e}\int_\Gamma\hat{F}_\Gamma^e\varphi_I\mathrm{d}S=\int_{\Omega^e}(\mathbf{q}_h\cdot\nabla\varphi_I-f_d\varphi_I)\mathrm{d}\mathbf{x}=Q_I^e \tag{4.26}$$

where Q_I^e is a computable quantity. For a given function φ_I, imposing (4.26) for all knot spans supporting φ_I leads to a small-size system of equations $\mathcal{S}_I$ to solve. It is important to notice that:

- ensuring (4.26) naturally enables to verify (4.24) due to the partition of unity property $\sum_{I=1}^n\varphi_I=1$ in the physical space;
- the unknowns of each system $\mathcal{S}_I$ are quantities $\int_\Gamma\hat{F}_\Gamma\varphi_I\mathrm{d}S$ i.e. projections, over φ_I, of unsigned tractions $\hat{F}_\Gamma$ on edge/face Γ of the physical mesh;
- each system $\mathcal{S}_I$ is usually rank deficient, but there is always at least one solution due to the weak equilibration property verified by $\mathbf{q}_h$ and resulting from (5.4). For a basis function φ_I vanishing on $\partial_q\Omega$, this reads $\sum_e Q_I^e=\int_\Omega(\mathbf{q}_h\cdot\nabla\varphi_I-f_d\varphi_I)\mathrm{d}\mathbf{x}=0$;
- a unique solution for each system $\mathcal{S}_I$ may be obtained, if necessary, by the minimization of a cost function that involves the least square distances between unknowns $\int_\Gamma\hat{F}_\Gamma\varphi_I\mathrm{d}S$ and available average quantities $\int_\Gamma\langle\mathbf{q}_h\rangle\cdot\mathbf{n}\varphi_I\mathrm{d}S$. As the quantity $\mathbf{q}_h\cdot\mathbf{n}$ might be discontinuous across the interface Γ (even though is it usually not the case due to the classical use of high-order IGA basis functions), $\langle\mathbf{q}_h\rangle$ denotes the average of this field defined from values on the two knot spans connected to Γ.

After computing projection quantities $\int_\Gamma\hat{F}_\Gamma\varphi_I\mathrm{d}S$, (unsigned) tractions $\hat{F}_\Gamma$ can be recovered as a linear combination of IGA shape functions:

$$\hat{F}_\Gamma(\mathbf{x})=\sum_{J\in\mathcal{J}_\Gamma}\hat{f}_\Gamma^J\varphi_{J|\Gamma}(\mathbf{x}) \tag{4.27}$$

where $\mathcal{J}_\Gamma$ denotes the set of indices for non-zero shape functions on Γ. Nevertheless, as non-zero functions $\varphi_{J|\Gamma}$ are usually not independent functions (contrary to the FEA

case), projections on independent functions should be recovered in order to define invertible elementary matrix systems giving coefficients $\hat{f}_\Gamma^J$.

Details on the definition and solution of each system $\mathcal{S}_I$, as well as on the computation of coefficients $\hat{f}_\Gamma^J$, are given in Section 4.2.2 for an illustrative 2D case.

Step 2: local recovery of an equilibrated flux field

From the equilibrated traction field $\hat{F}^e$ computed in Step 1, an associated admissible flux field $\hat{\mathbf{q}}_h$ verifying (4.23) is recovered over each knot span Ω^e. The local equilibrium property (4.23) may be recast in a weak form as:

$$\int_{\Omega^e} \hat{\mathbf{q}}_h \cdot \nabla v \mathrm{d}\mathbf{x} = \int_{\Omega^e} f_d v \mathrm{d}\mathbf{x} + \int_{\partial\Omega^e} \hat{F}^e v \mathrm{d}S \quad \forall v \in \mathcal{U}(\Omega^e) \tag{4.28}$$

with $\mathcal{U}(\Omega^e) = H^1(\Omega^e)$. A (non-unique) solution to (4.28) can be obtained analytically, using polynomial functions with sufficiently high degree, provided the source term f_d is polynomial as well [LR97]. In practice, an alternative approach with numerical solution and higher-order enrichment is preferred. Indeed, the optimal flux field satisfying (4.28) is the one that minimizes over Ω^e the local contribution $\|\hat{\mathbf{q}}_h - \mathbf{q}_h\|_{\mathbb{K}^{-1}|\Omega^e}$ of the error estimate $E^2_{CRE}(u_h, \hat{\mathbf{q}}_h)$ (or equivalently minimizes $\|\hat{\mathbf{q}}_h\|_{\mathbb{K}^{-1}|\Omega^e}$). Duality arguments show that the underlying constrained minimization problem is equivalent to taking $\hat{\mathbf{q}}_{h|\Omega^e} = \mathbb{K}\nabla\rho$, with $\rho \in \mathcal{U}(\Omega^e)$ satisfying the following Neumann problem:

$$\int_{\Omega^e} \mathbb{K}\nabla\rho \cdot \nabla v \mathrm{d}\mathbf{x} = \int_{\Omega^e} f_d v \mathrm{d}\mathbf{x} + \int_{\partial\Omega^e} \hat{F}^e v \mathrm{d}S \quad \forall v \in \mathcal{U}(\Omega^e) \tag{4.29}$$

A numerical approximation of the solution of (4.29) is in practice obtained from an IGA approximation using mesh enrichment over the knot span Ω^e. In the remainder of the chapter, we choose to use a k-refinement approach (see Section 3.2) with extra order 3; the final order of local basis functions is therefore $p+3$. This choice of extra order value is motivated by numerical studies performed in [BSU+94].

Remark. The flux obtained from a numerical approximation of ρ is not rigorously equilibrated in each knot span Ω^e, so that computed error bounds are not mathematically guaranteed. Nevertheless, choosing a $p+3$ order enables to obtain in practice a negligible error due to non-equilibrium in the computation of the CRE error estimate [BSU+94].

Remark. The solution of problem (4.29) is defined up to an additive constant (translation). This constant is fixed by imposing ρ to zero at an arbitrary point by means of a Lagrange multiplier.

Remark. The previous approach for the construction of an admissible field $\hat{\mathbf{q}}_h$ can also be used in the case of locally refined IGA meshes. Two cases should be considered:

- when hierarchical refinement is performed, with the local addition of patches representing finer details, the associated nested structure of the approximation space makes the extension of the hybrid-flux approach straightforward;
- when T-splines are used, the local refinement procedure is equivalent to hanging nodes in the FEA context. Consequently, a similar approach to that used for the construction of an admissible field $\hat{\mathbf{q}}_h$ in FEA with hanging nodes (see [LM96]) should be followed.

4.2.2 Technical implementation on a 2D example

In this section, we focus on technical details related to Step 1 of the previously introduced procedure, i.e. the computation of equilibrated tractions. For this purpose, and in order the methodology to be easily understandable, we work in the parametric space (made of regular knot spans) instead of the physical space; we recall that they are related each other by means of a global mapping $\mathbf{F}$ in the isoparametric framework. Furthermore, in order to keep notations simple, we consider a two-dimensional parametric space with order 2 B-Spline functions and knot vectors $\boldsymbol{\Xi}^1 = [0,0,0,1/3,2/3,1,1,1]$ and $\boldsymbol{\Xi}^2 = [0,0,0,1/3,2/3,1,1,1]$ (see Figure 4.1). Consequently, the parametric space is made of 3 knot spans and 5 functions in each direction (9 knot spans and 25 shape functions in the tensorized space). Tensorization results in the fact that basis functions read:

$$\varphi_I(\xi,\eta) = N_{i,2}(\xi).N_{j,2}(\eta) = N_i(\xi).N_j(\eta) \quad \text{or equivalently} \quad \varphi_I = N_i^{\xi}.N_j^{\eta} \quad (1 \leq i,j \leq 5) \tag{4.30}$$

where we simplified the notation $N_i = N_{i,2}$ for better readability. These functions are associated with control points $\mathbf{B}_I$ in order to define the exact geometry in the physical space.
Similarly, each knot span in the parametric space reads:

$$\overline{\Omega}^e = \overline{\Omega}_1^{e_1} \times \overline{\Omega}_2^{e_2} \quad (1 \leq e_1, e_2 \leq 3) \tag{4.31}$$

where $\overline{\Omega}_d^{e_d}$ are 1D knot spans in the dimension d. In each 1D dimension, it can be easily seen that several functions may be non-zero at a given knot (interface between knot spans) compared to FEA where a single basis function is non-zero at each node position. Furthermore, the Cox-de Boor recursion formula leads to 3 (or $p+1$ in the general case) different basis functions supported by a given knot span, as illustrated in Figure 4.2.

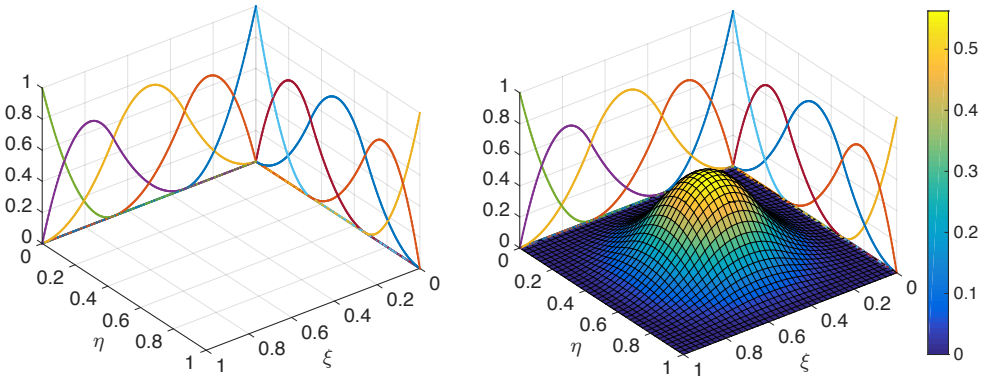

Figure 4.1: 2D parametric space and shape functions constructed from the tensorization of knot vectors $\boldsymbol{\Xi}^1$ and $\boldsymbol{\Xi}^2$ (left), and plot of the basis function $N_{3,2}(\xi)N_{3,2}(\eta)$.

The restrictions of these functions to each individual 1D knot span will be used as independent functions on which to perform projections and define expansions (4.27) of tractions $\hat{F}_\Gamma$.

Coming back to the 2D parametric space, we then consider all shape functions which are non-zero at node positions (tensorization of knot positions). As an illustration, we consider the node i shown in Figure 4.3, for which 4 functions are non-zero: $N_2^\xi.N_2^\eta$, $N_2^\xi.N_3^\eta$, $N_3^\xi.N_2^\eta$, and $N_3^\xi.N_3^\eta$. Consequently, 4 systems $\mathcal{S}_I$ associated to each of these basis functions φ_I and resulting from (4.26) can be defined for this node (compared to one in classical FEA). They are defined over supports of each function as illustrated in Figure 4.4.

In order to detail systems $\mathcal{S}_I$ for functions of the type $\varphi_I = N_i^\xi.N_j^\eta$, we introduce the following notations:

$$\int_{\Gamma_k} \hat{F}_{\Gamma_k} N_i^\xi.N_j^\eta \mathrm{d}S = \hat{b}^{ij}_{\Gamma_k} \quad ; \quad \int_{\overline{\Omega}^e} (\mathbf{q}_h \cdot \nabla(N_i^\xi.N_j^\eta) - f_d N_i^\xi.N_j^\eta)\mathrm{d}\boldsymbol{\xi} = Q^e_{ij} \tag{4.32}$$

Illustration of the system for $\varphi_I = N_2^\xi.N_3^\eta$

We use the numbering of Figure 4.3, and write (4.26) for each knot span in the support of $N_2^\xi.N_3^\eta$. We thus come down to the configuration shown in Figure 4.3, and the following

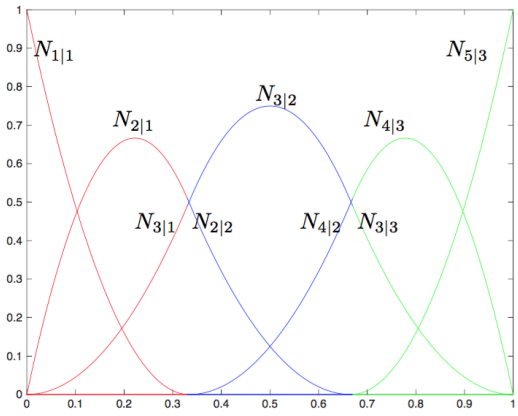

Figure 4.2: Restrictions of 1D B-Spline functions to knot span 1 (in red), 2 (in blue), and 3 (in green).

systems holds:

$$\begin{cases} \hat{b}^{23}_{\Gamma_1} - \hat{b}^{23}_{\Gamma_7} & = Q^1_{23} \\ \hat{b}^{23}_{\Gamma_7} - \hat{b}^{23}_{\Gamma_2} & = Q^2_{23} \\ \hat{b}^{23}_{\Gamma_8} - \hat{b}^{23}_{\Gamma_1} + \hat{b}^{23}_{\Gamma_4} & = Q^4_{23} \\ \hat{b}^{23}_{\Gamma_2} - \hat{b}^{23}_{\Gamma_8} - \hat{b}^{23}_{\Gamma_5} & = Q^5_{23} \\ \hat{b}^{23}_{\Gamma_9} - \hat{b}^{23}_{\Gamma_4} & = Q^7_{23} \\ \hat{b}^{23}_{\Gamma_5} - \hat{b}^{23}_{\Gamma_9} & = Q^8_{23} \end{cases} \tag{4.33}$$

The previous system is simplified by gathering knot spans 4 and 7, and 5 and 8 (see Figure 4.5), so that the system becomes small-sized and similar to the FEA context with interior node i. It reads:

$$\begin{cases} \hat{b}^{23}_{\Gamma_1} - \hat{b}^{23}_{\Gamma_7} & = Q^1_{23} \\ \hat{b}^{23}_{\Gamma_7} - \hat{b}^{23}_{\Gamma_2} & = Q^2_{23} \\ \hat{b}^{23}_{\Gamma_8} + \hat{b}^{23}_{\Gamma_9} - \hat{b}^{23}_{\Gamma_1} & = Q^4_{23} + Q^7_{23} \\ \hat{b}^{23}_{\Gamma_2} - \hat{b}^{23}_{\Gamma_8} - \hat{b}^{23}_{\Gamma_9} & = Q^5_{23} + Q^8_{23} \end{cases} \tag{4.34}$$

Noticing that $Q^1_{23} + Q^2_{23} + Q^4_{23} + Q^5_{23} + Q^7_{23} + Q^8_{23} = 0$ (weak equilibration property (5.4) verified by $\mathbf{q}_h$), the previous system has an infinite number of solutions. The following cost function is then introduced:

$$\sum_{\Gamma \in \mathcal{G}} \left| \frac{\hat{b}^{23}_{\Gamma} - \bar{b}^{23}_{\Gamma}}{|\Gamma|} \right|^2 \tag{4.35}$$

with $\mathcal{G} = \{\Gamma_1, \Gamma_2, \Gamma_7, \Gamma_8, \Gamma_9\}$ and $\bar{b}^{23}_{\Gamma} = \int_{\Gamma} \langle \mathbf{q}_h \rangle \cdot \mathbf{n} N^{\xi}_2 . N^{\eta}_3 \mathrm{d}S$ ($\langle \mathbf{q}_h \rangle = \mathbf{q}_h$ here as C^1

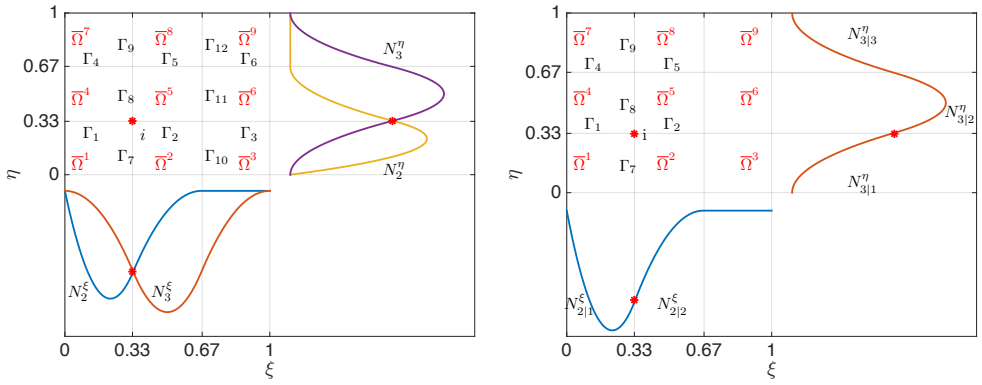

Figure 4.3: Definition of shape functions and edges associated with node i (left), and configuration at node i for the system associated to $\varphi_I = N_2^\xi.N_3^\eta$ (right).

functions are used). A constrained minimization is then performed to recover a unique solution to (4.34).

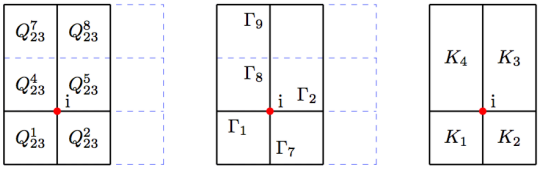

Figure 4.5: Illustration of the gathering of knot spans around node i.

Final projections and expansion of tractions

Using a similar procedure, systems $\mathcal{S}_I$ associated to node i and for basis functions $N_2^\xi.N_2^\eta$, $N_3^\xi.N_2^\eta$, and $N_3^\xi.N_3^\eta$ are solved (see Figure 4.4). Values are thus obtained for the following unknowns:

- $\hat{b}_{\Gamma_1}^{22}$, $\hat{b}_{\Gamma_2}^{22}$, $\hat{b}_{\Gamma_7}^{22}$, $\hat{b}_{\Gamma_8}^{22}$ (for the system with basis function $N_2^\xi.N_2^\eta$);
- $\hat{b}_{\Gamma_1}^{23}$, $\hat{b}_{\Gamma_2}^{23}$, $\hat{b}_{\Gamma_7}^{23}$, $\hat{b}_{\Gamma_8}^{23}$, $\hat{b}_{\Gamma_9}^{23}$ (for the system with basis function $N_2^\xi.N_3^\eta$);
- $\hat{b}_{\Gamma_1}^{32}$, $\hat{b}_{\Gamma_2}^{32}$, $\hat{b}_{\Gamma_3}^{32}$, $\hat{b}_{\Gamma_7}^{32}$, $\hat{b}_{\Gamma_8}^{32}$ (for the system with basis function $N_3^\xi.N_2^\eta$);
- $\hat{b}_{\Gamma_1}^{33}$, $\hat{b}_{\Gamma_2}^{33}$, $\hat{b}_{\Gamma_3}^{33}$, $\hat{b}_{\Gamma_7}^{33}$, $\hat{b}_{\Gamma_8}^{33}$, $\hat{b}_{\Gamma_9}^{33}$ (for the system with basis function $N_3^\xi.N_3^\eta$).

Then, projections on edges over independent restrictions of 1D B-Spline functions (see Figure 4.2) can be obtained as a linear combination (using the partition of unity

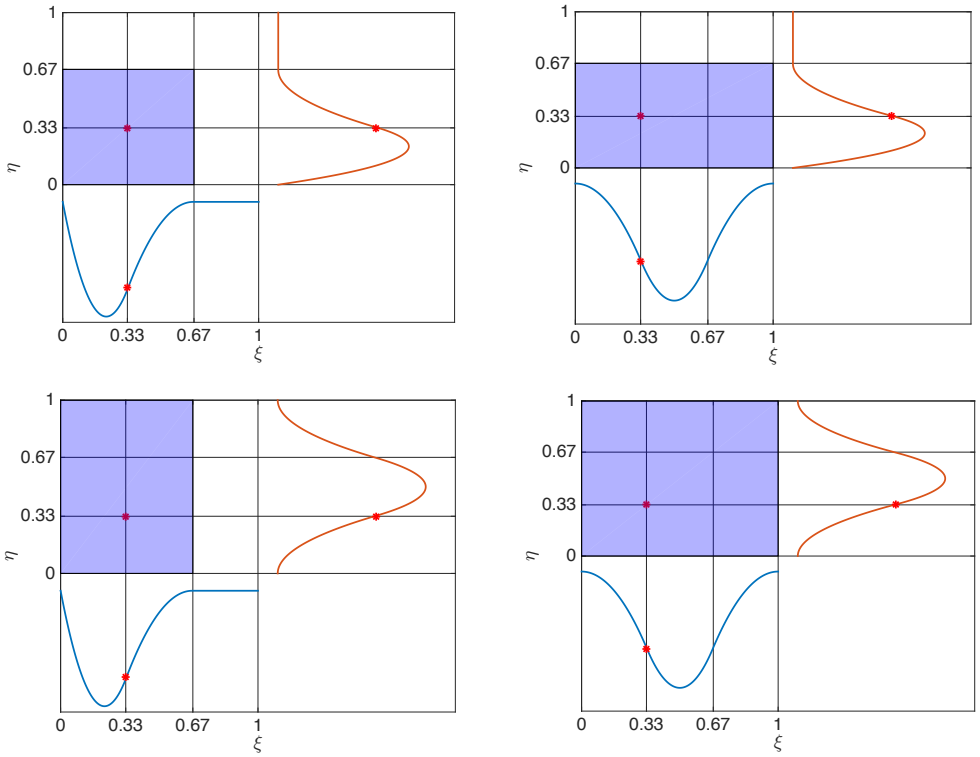

Figure 4.4: Support of the system $\mathcal{S}_I$ associated to basis function $N_2^\xi.N_2^\eta$ (top left), $N_3^\xi.N_2^\eta$ (top right), $N_2^\xi.N_3^\eta$ (bottom left), and $N_3^\xi.N_3^\eta$ (bottom right).

property) of the previous values:

$$\begin{aligned}
&\int_{\Gamma_1} \hat{F}_{\Gamma_1} N_{2|1} \mathrm{d}S = \hat{b}^{22}_{\Gamma_1} + \hat{b}^{23}_{\Gamma_1} \quad ; \quad \int_{\Gamma_1} \hat{F}_{\Gamma_1} N_{3|1} \mathrm{d}S = \hat{b}^{32}_{\Gamma_1} + \hat{b}^{33}_{\Gamma_1} \\
&\int_{\Gamma_2} \hat{F}_{\Gamma_2} N_{2|2} \mathrm{d}S = \hat{b}^{22}_{\Gamma_2} + \hat{b}^{23}_{\Gamma_2} \quad ; \quad \int_{\Gamma_2} \hat{F}_{\Gamma_1} N_{3|2} \mathrm{d}S = \hat{b}^{32}_{\Gamma_2} + \hat{b}^{33}_{\Gamma_2} \\
&\int_{\Gamma_3} \hat{F}_{\Gamma_3} N_{3|3} \mathrm{d}S = \hat{b}^{32}_{\Gamma_3} + \hat{b}^{33}_{\Gamma_2} \\
&\int_{\Gamma_7} \hat{F}_{\Gamma_7} N_{2|1} \mathrm{d}S = \hat{b}^{22}_{\Gamma_7} + \hat{b}^{32}_{\Gamma_7} \quad ; \quad \int_{\Gamma_7} \hat{F}_{\Gamma_7} N_{3|1} \mathrm{d}S = \hat{b}^{23}_{\Gamma_7} + \hat{b}^{33}_{\Gamma_7} \\
&\int_{\Gamma_8} \hat{F}_{\Gamma_8} N_{2|2} \mathrm{d}S = \hat{b}^{22}_{\Gamma_8} + \hat{b}^{32}_{\Gamma_8} \quad ; \quad \int_{\Gamma_8} \hat{F}_{\Gamma_8} N_{3|2} \mathrm{d}S = \hat{b}^{23}_{\Gamma_8} + \hat{b}^{33}_{\Gamma_8} \\
&\int_{\Gamma_9} \hat{F}_{\Gamma_9} N_{3|3} \mathrm{d}S = \hat{b}^{23}_{\Gamma_9} + \hat{b}^{33}_{\Gamma_9}
\end{aligned} \tag{4.36}$$

Performing a similar approach for all nodes and all basis functions enables to obtained all necessary projections, before recovering tractions themselves. For instance, considering the node j shown in Figure 4.6 enables to recover the last projection on edge Γ_8:

$$\int_{\Gamma_8} \hat{F}_{\Gamma_8} N_{4|2} \mathrm{d}S = \hat{b}^{24}_{\Gamma_8} + \hat{b}^{34}_{\Gamma_8} \tag{4.37}$$

Eventually, the traction $\hat{F}_{\Gamma_8}$ is recovered as:

$$\hat{F}_{\Gamma_8}(\boldsymbol{\xi}) = \hat{f}^2_{\Gamma_8} N_{2|2}(\boldsymbol{\xi}) + \hat{f}^3_{\Gamma_8} N_{3|2}(\boldsymbol{\xi}) + \hat{f}^4_{\Gamma_8} N_{4|2}(\boldsymbol{\xi}) \tag{4.38}$$

where coefficients $\hat{f}^2_{\Gamma_8}$, $\hat{f}^3_{\Gamma_8}$, and $\hat{f}^4_{\Gamma_8}$ are solutions of a small linear system involving known projections $\int_{\Gamma_8} \hat{F}_{\Gamma_8} N_{2|2} \mathrm{d}S$, $\int_{\Gamma_8} \hat{F}_{\Gamma_8} N_{3|2} \mathrm{d}S$, and $\int_{\Gamma_8} \hat{F}_{\Gamma_8} N_{4|2} \mathrm{d}S$.

The overall procedure for the construction of equilibrated tractions thus involves the solution of small-size independent systems, as in FEA.

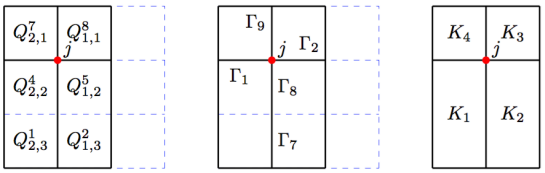

Figure 4.6: Illustration of the gathering of knot spans around node j, for the system with basis function $N^{\xi}_2.N^{\eta}_3$.

4.3 Numerical examples

4.3.1 Example 1: thermal problem on a quarter of an annulus

We first consider a heat transfer problem (Poisson equation) on a quarter of annulus with prescribed homogeneous Dirichlet boundary conditions, similar to the one described in [KT15]. The physical domain Ω is defined as $(r, \theta) \in [1, 4] \times [0, \pi/2]$ in a polar coordinates system; it is represented using order 2 NURBS basis functions in both directions of the parametric space (see Figure 4.7).

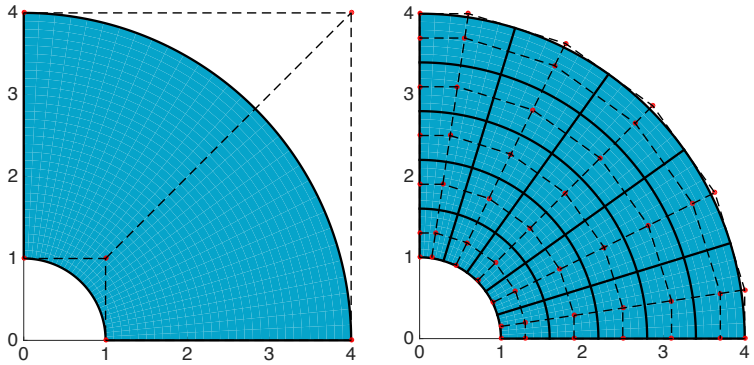

Figure 4.7: IGA representation of the geometry with control mesh (left), and initial discretization with 5×5 non-zero knot spans in the physical space. Control points are represented by red dots.

The problem reads:

$$-\Delta u = f \quad \text{in } \Omega \quad ; \quad u = 0 \quad \text{on } \partial\Omega \tag{4.39}$$

The body force is chosen as:

$$\begin{aligned} f(x,y) =& (2x^4 + 2y^4 + 4x^2y^2 - 50x^2 - 50y^2 + 100)\sin(x)\sin(y) \\ &+ (68x - 8x^3 - 8xy^2)\cos(x)\sin(y) \\ &+ (68y - 8y^3 - 8x^2y)\sin(x)\cos(y) \end{aligned} \tag{4.40}$$

so that the exact solution $u(x, y)$ is analytical (manufactured solution): $u(x, y) = (x^2 + y^2 - 1).(x^2 + y^2 - 16).\sin(x).\sin(y)$. It is represented in Figure 4.8.

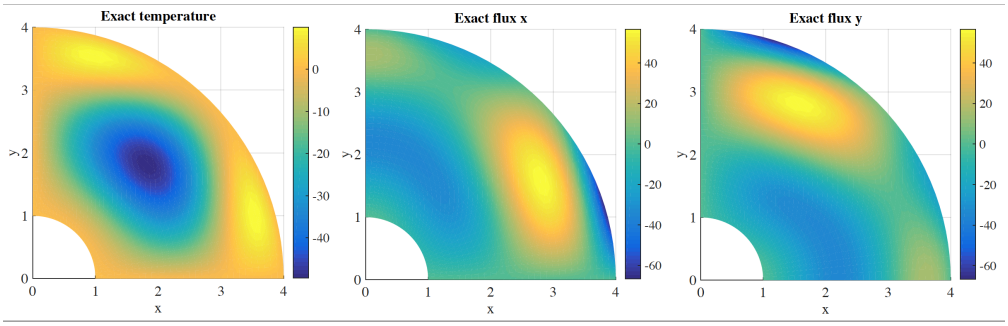

Figure 4.8: Exact solution for the 2D heat problem: u (left), $\mathbf{q} \cdot \mathbf{e}_x$ (center), and $\mathbf{q} \cdot \mathbf{e}_y$ (right).

Estimation of the error in the energy norm

When approximating the exact solution by means of IGA, we investigate the accuracy and convergence of the CRE estimate $E_{CRE}(u_h, \hat{\mathbf{q}}_h)$ as an assessment of the exact discretization error in the energy norm $\mathcal{E}_{glob}$. For this purpose, we consider three uniform meshes with different mesh sizes as shown in Figure 4.9.

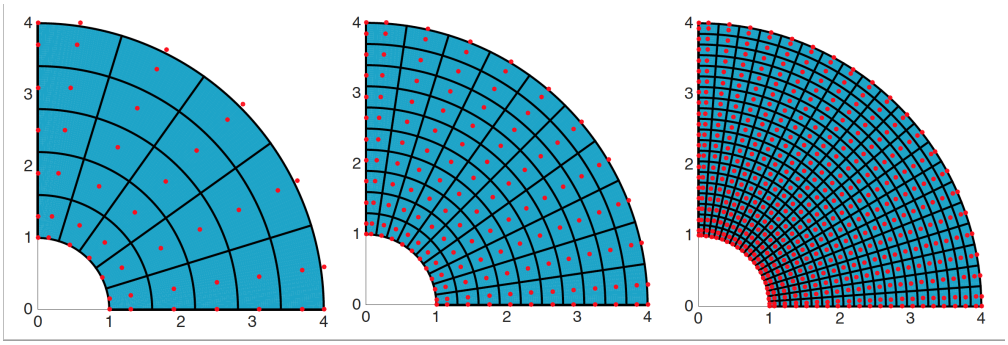

Figure 4.9: The various mesh sizes used, with 5×5 (left), 10×10 (center), and 20×20 (right) knot spans.

The approximate IGA flux field $\mathbf{q}_h$ obtained using the 5×5 mesh is represented in Figure 4.10.

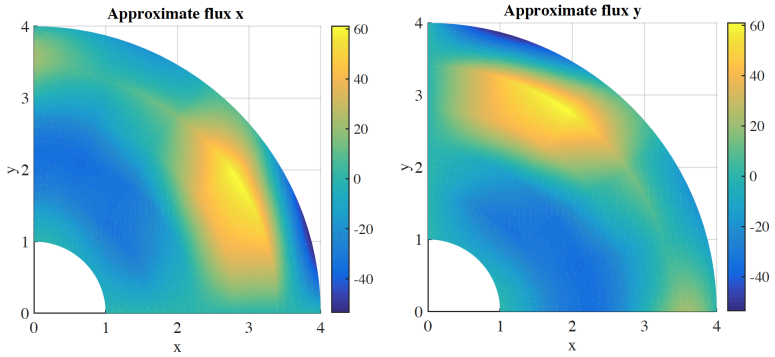

Figure 4.10: Approximate IGA flux field obtained with the 5×5 mesh: $\mathbf{q}_h \cdot \mathbf{e}_x$ (left) and $\mathbf{q}_h \cdot \mathbf{e}_y$ (right).

For each mesh, we represent in Figure 4.11, 4.12, and 4.13, respectively, the admissible flux field recovered from the approach of Section 5.4.1, as well as the associated CRE error map.

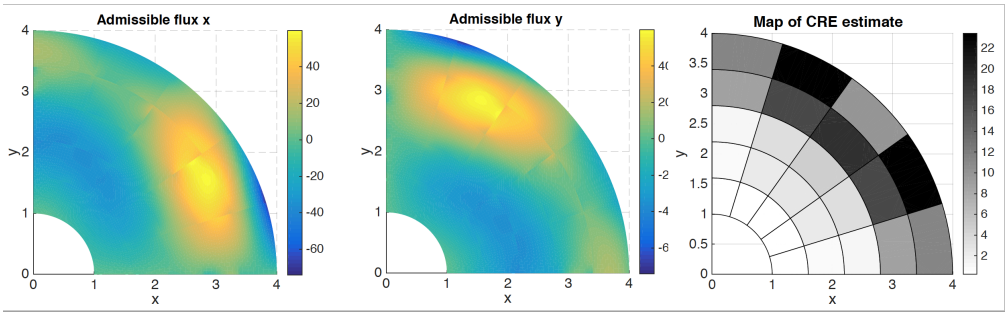

Figure 4.11: Admissible flux $\hat{\mathbf{q}}_h \cdot \mathbf{e}_x$ (left) and $\hat{\mathbf{q}}_h \cdot \mathbf{e}_y$ (center), and CRE error map (right) for the 5×5 mesh.

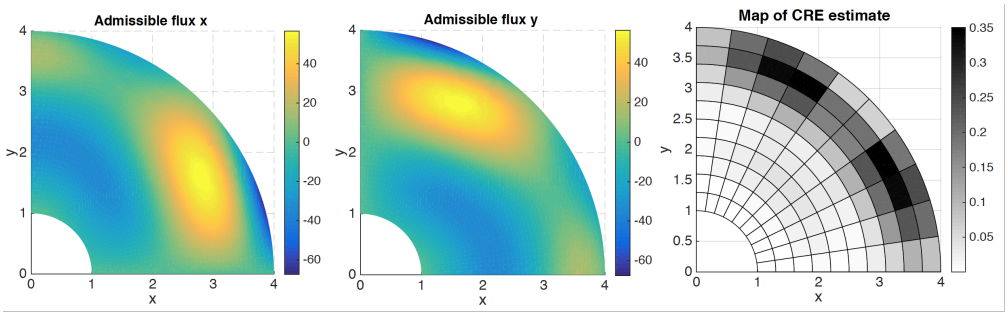

Figure 4.12: Admissible flux $\hat{\mathbf{q}}_h \cdot \mathbf{e}_x$ (left) and $\hat{\mathbf{q}}_h \cdot \mathbf{e}_y$ (center), and CRE error map (right) for the 10×10 mesh.

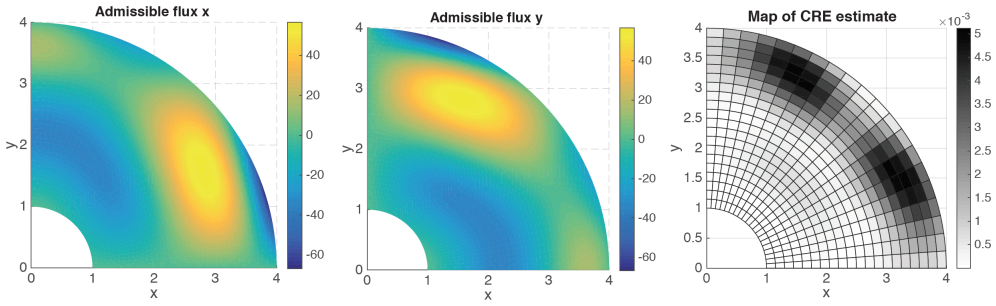

Figure 4.13: Admissible flux $\hat{\mathbf{q}}_h \cdot \mathbf{e}_x$ (left) and $\hat{\mathbf{q}}_h \cdot \mathbf{e}_y$ (center), and CRE error map (right) for the 20×20 mesh.

Eventually, we plot in Figure 4.14 the convergence of the CRE error estimate with respect to the (uniform) mesh size. We observe that the convergence rate is similar to the one predicted by *a priori* error analysis.

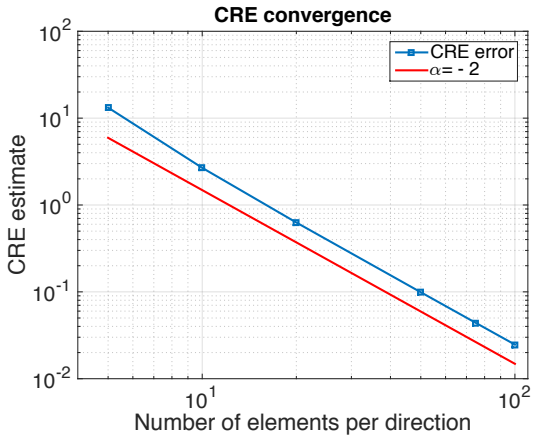

Figure 4.14: Convergence of the error estimate with respect to the mesh size.

Effectivity index with degree 2,3,4

For this problem, the value of the global effectivity index $i_{eff} = E_{CRE}/\|e_h\|_{\mathbb{K}}$ is between 1.08 and 1.11 for all meshes with $p = 2$, and between 1.0009 and 1.0116 for all meshes with $p = 4$. Furthermore, we represent in Figures 4.15, 4.16, 4.17 (resp. Figures 4.18, 4.19, 4.20 and Figures 4.21, 4.22, 4.23) the CRE error maps and local effectivity indices for IGA degrees 2, 3 and 4, and for a 5×5 (resp. 10×10 and 15×15) mesh. The maps of local effectivity indices show that the CRE estimate is a relevant and robust tool for mesh adaptation.

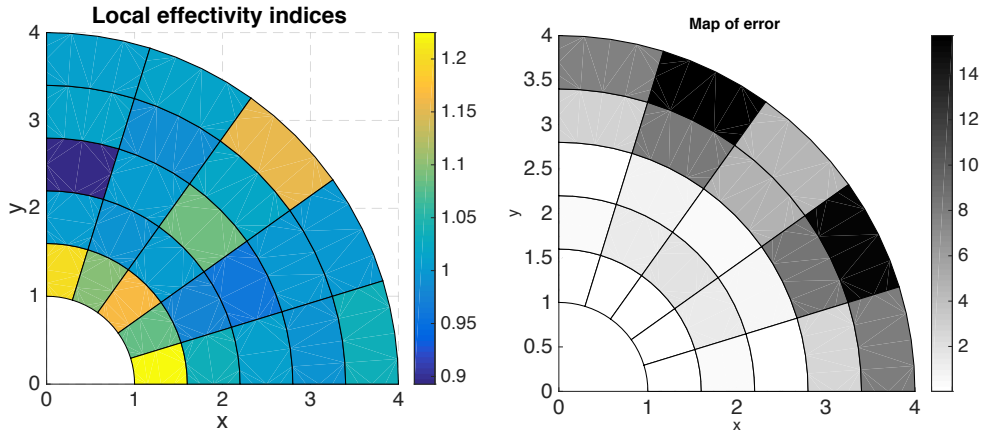

Figure 4.15: Local effectivity indices (left) and CRE error map (right) for the 5×5 mesh and IGA degree 2.

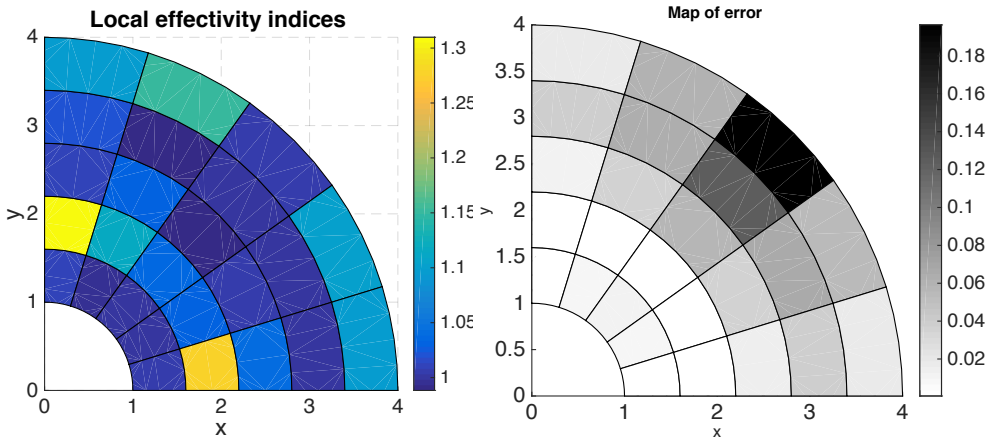

Figure 4.16: Local effectivity indices (left) and CRE error map for the 5×5 mesh and IGA degree 3.

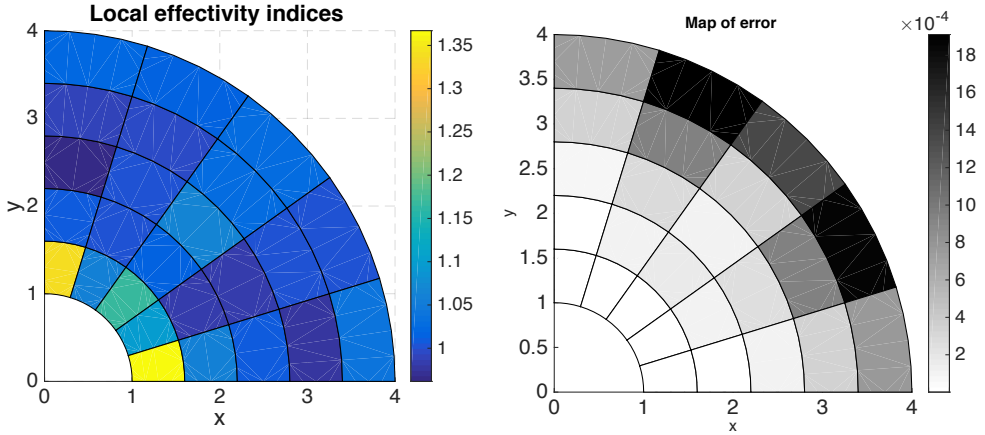

Figure 4.17: Local effectivity indices (left) and CRE error map for the 5×5 mesh and IGA degree 4.

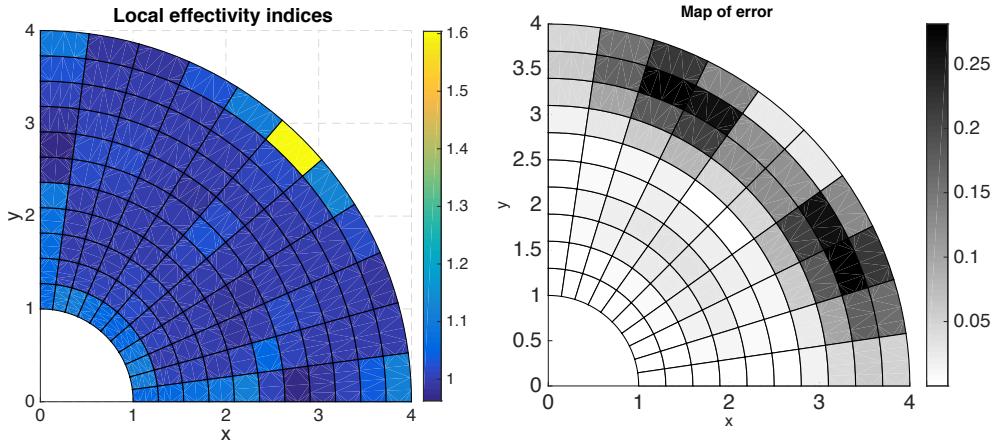

Figure 4.18: Local effectivity indices (left) and CRE error map for the 10×10 mesh and IGA degree 2.

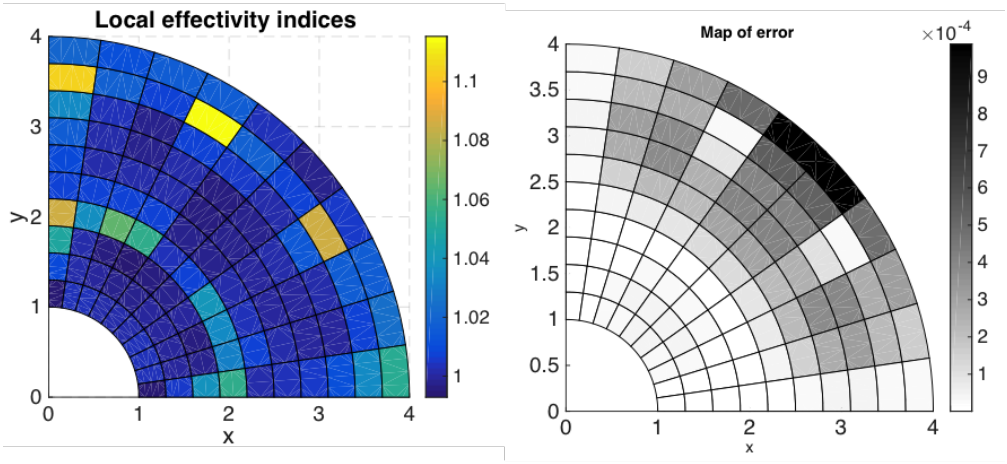

Figure 4.19: Local effectivity indices (left) and CRE error map for the 10×10 mesh and IGA degree 3.

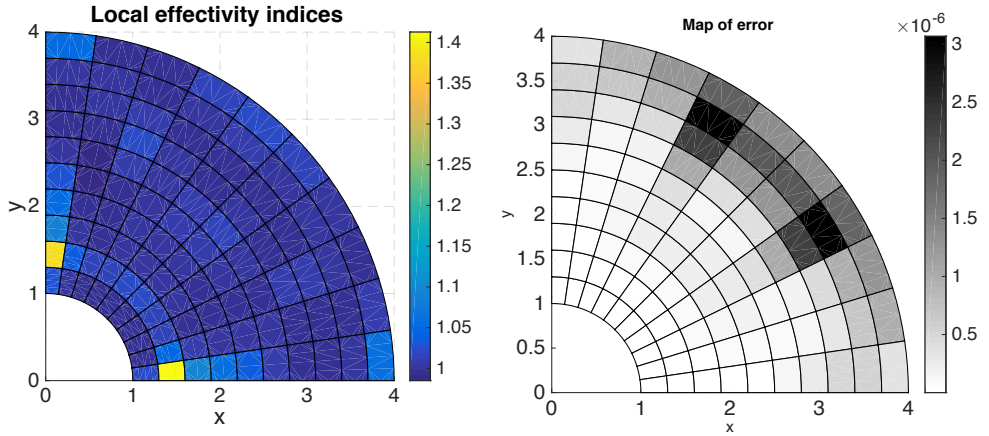

Figure 4.20: Local effectivity indices (left) and CRE error map for the 10×10 mesh and IGA degree 4.

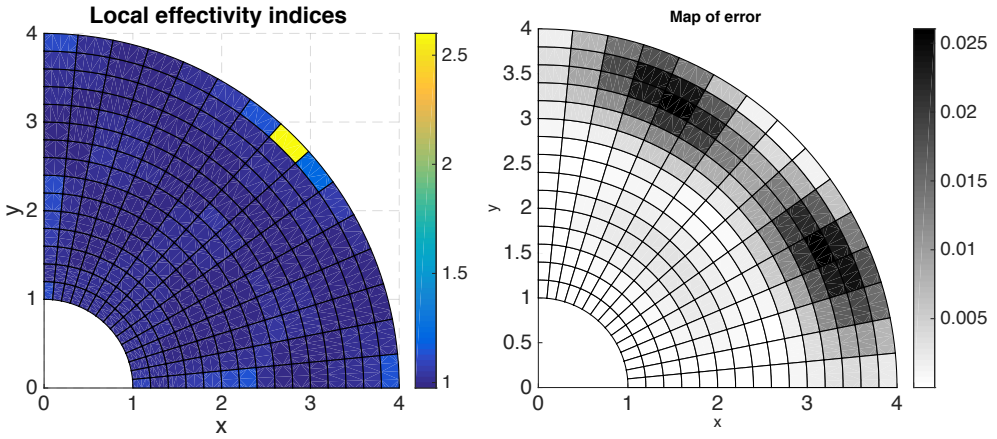

Figure 4.21: Local effectivity indices (left) and CRE error map (right) for the 15×15 mesh and IGA degree 2.

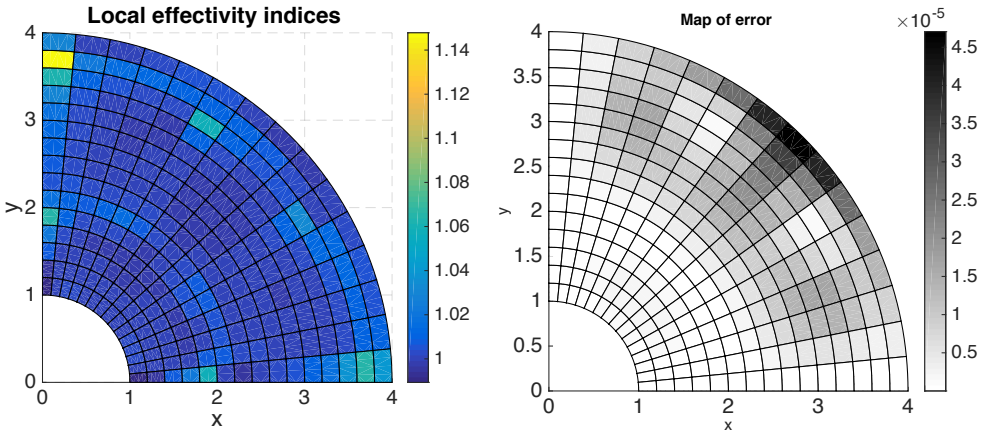

Figure 4.22: Local effectivity indices (left) and CRE error map (right) for the 15×15 mesh and IGA degree 3.

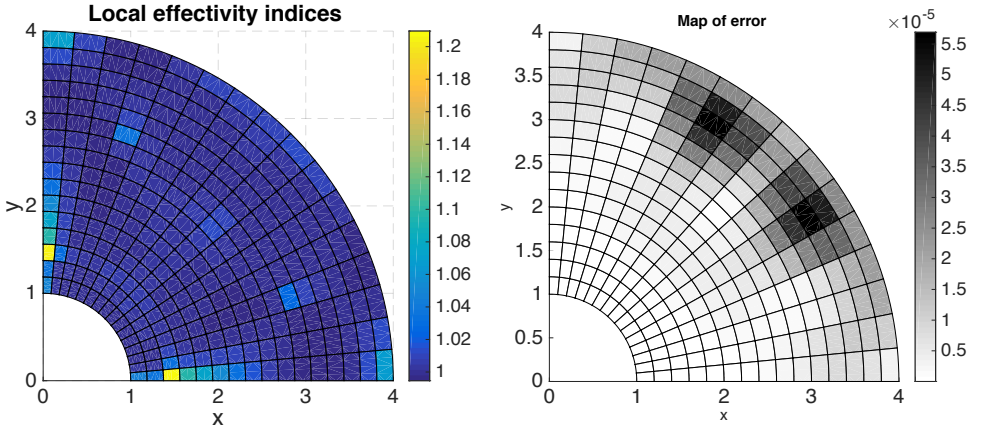

Figure 4.23: Local effectivity indices (left) and CRE error map (right) for the 15×15 mesh and IGA degree 4.

Estimation of the error on a quantity of interest

We consider the quantity of interest $Q = \dfrac{1}{|\omega|}\displaystyle\int_{\omega} u(\mathbf{x})\mathrm{d}\mathbf{x}$ where ω is a local zone (single knot span) indicated in Figure 4.24.

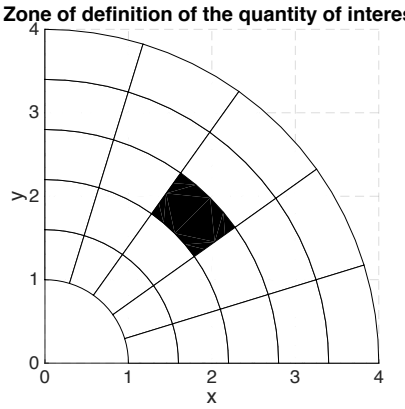

Figure 4.24: Definition of the local zone ω over which the quantity of interest Q is defined.

In order to assess the discretization error on this quantity, we introduce the adjoint problem as described in Section 4.1.3. Its loading is made of a uniform body force $f_\Sigma = \dfrac{1}{|\omega|}$ applied in ω. The approximate solution obtained using IGA with a 10×10 mesh is given in Figure 4.25.

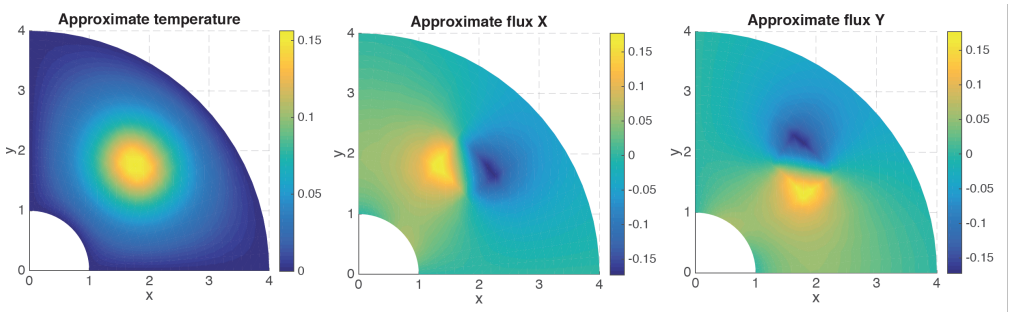

Figure 4.25: Approximate IGA adjoint solution: $\tilde{u}_h$ (left), $\tilde{\mathbf{q}}_h \cdot \mathbf{e}_x$ (center), and $\tilde{\mathbf{q}}_h \cdot \mathbf{e}_y$ (right).

After computing an admissible adjoint flux field $\hat{\tilde{\mathbf{q}}}_h$, and the associated CRE error estimate $E_{CRE}(\tilde{u}_h, \hat{\tilde{\mathbf{q}}}_h)$, bounds on Q can be obtained (see Section 4.1.3). We give in Figure 4.26 the map of the admissible adjoint flux field $\hat{\tilde{\mathbf{q}}}_h$ and that of the CRE error estimate $E_{CRE}(\tilde{u}_h, \hat{\tilde{\mathbf{q}}}_h)$. In addition, and from the bounding result (4.22), we represent in Figure 4.27 the evolution of the relative error bounding gap $2E_{CRE}(u_h, \hat{\mathbf{q}}_h).E_{CRE}(\tilde{u}_h, \hat{\tilde{\mathbf{q}}}_h)/(Q_h^- + Q_h^+)$ with respect to the mesh size of the adjoint problem alone. Here, the adjoint problem is refined uniformly.

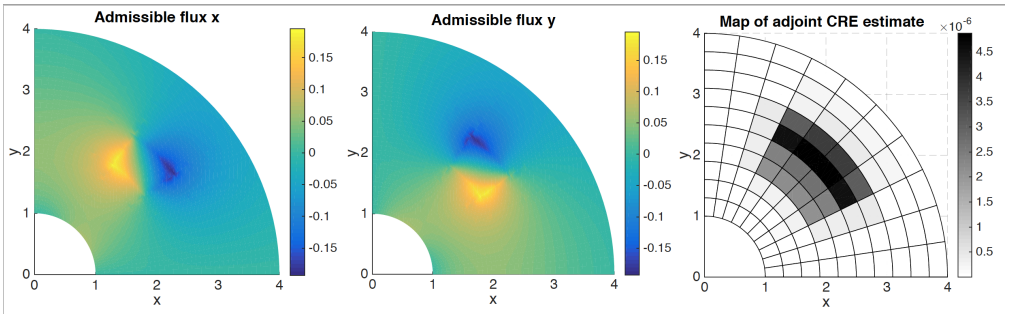

Figure 4.26: Adjoint flux field $\hat{\tilde{\mathbf{q}}}_h \cdot \mathbf{e}_x$ (left) and $\hat{\tilde{\mathbf{q}}}_h \cdot \mathbf{e}_y$ (center), and map of the adjoint CRE estimate (right).

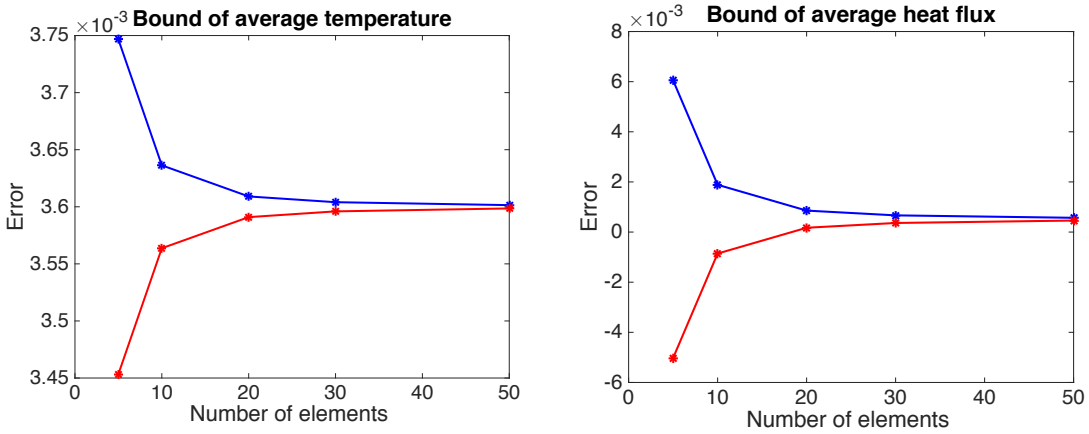

Figure 4.27: Evolution of the relative bounding gap $2E_{CRE}(u_h, \hat{\mathbf{q}}_h).E_{CRE}(\tilde{u}_h, \hat{\tilde{\mathbf{q}}}_h)/(Q_h^- + Q_h^+)$ with respect to the adjoint mesh size.

We observe that we get both accurate and guaranteed bounds on the quantity of interest Q.

Estimation of the error on local mesh

We use here the hierarchical refinement tools available in the IGAPack package available at *https://github.com/canitesc/IGAPack*. The 8 elements in Figure 4.28 that have high error value are selected for local refinement. The error map of local refinement is showed in Figure 4.29; it indicates that the constructed CRE estimate is consistent with local refinement.

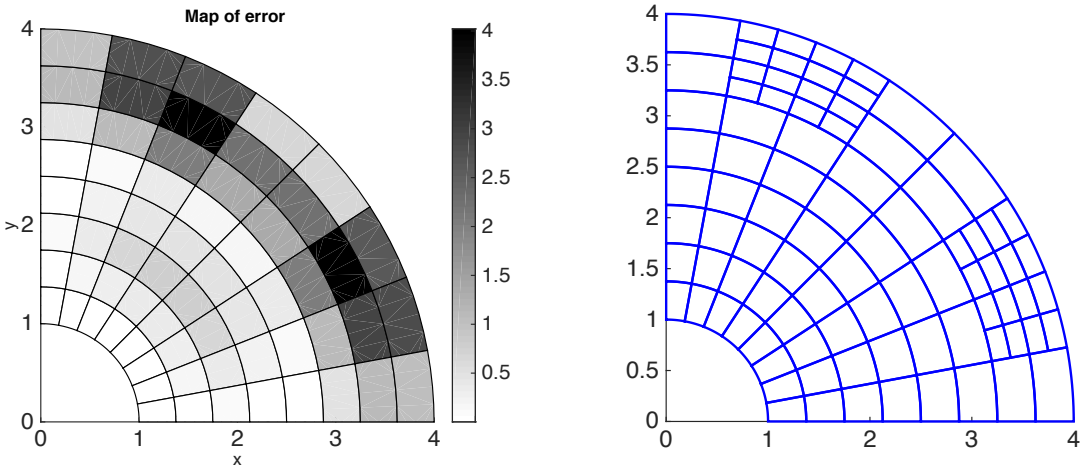

Figure 4.28: CRE error map and locally refined mesh in the area with maximum error.

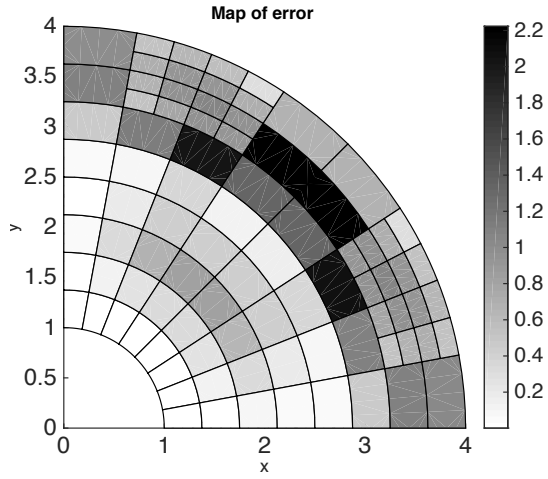

Figure 4.29: CRE error map for the locally refined mesh.

4.3.2 Example 2: elasticity problem on a L-shape domain

We now investigate a linear elasticity problem on a domain Ω consisting of a L-shape console beam (see Figure 4.30), as described in [KT15, VGJS11]. The domain is defined as $\Omega = [-1,1]^2 \backslash [0,1]^2$, and specific Dirichlet boundary conditions are prescribed as shown in Figure 4.30. The material parameters are $E = 1$ (Young modulus) and $\nu = 0.3$ (Poisson ratio). Order 2 basis functions are used in both directions of the parametric space. In its original discretization, the physical mesh is made of 10×10 knot spans.

The plane stress assumption is made.

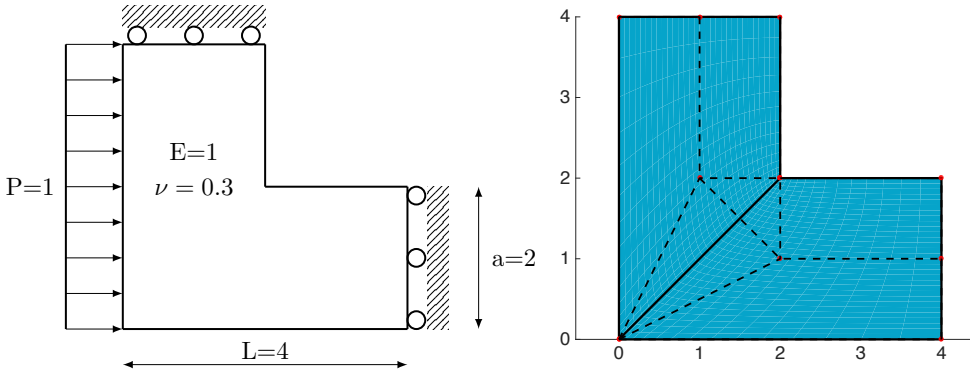

Figure 4.30: IGA representation of the L-shape geometry (left), and physical mesh (right).

The approximate IGA solution in terms of displacement and stress fields is given in Figure 4.31 and 4.32, respectively.

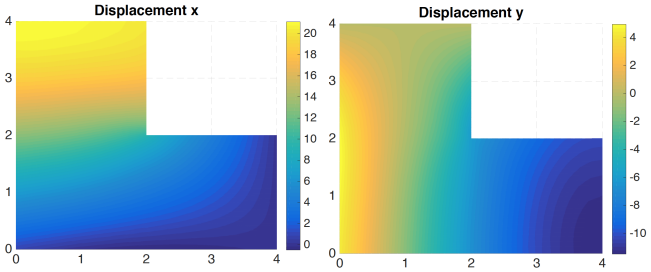

Figure 4.31: IGA displacement field $\mathbf{u}$, with components $\mathbf{u} \cdot \mathbf{e}_x$ (left) and $\mathbf{u} \cdot \mathbf{e}_y$ (right).

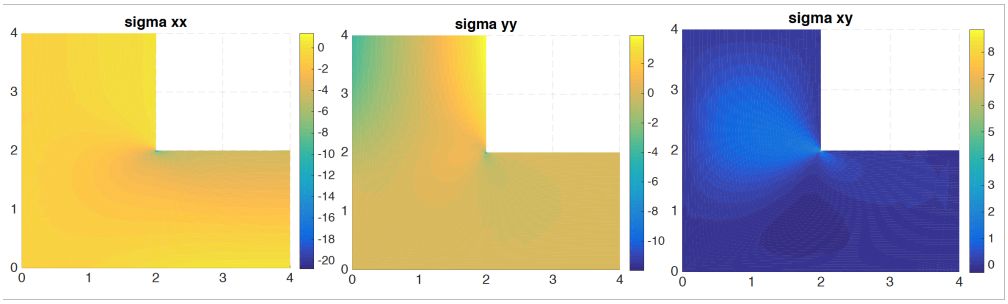

Figure 4.32: IGA stress field σ, with components σ_{xx} (left), σ_{yy} (center), and σ_{xy} (right).

The interest of this problem is to check that the estimate enables to accurately detect the local error due to the singularity at the re-entrant corner. After computing admissible fields, the map of the CRE estimate is given in Figure 4.33 for several uniform meshes with 10×10, 20×20, or 30×30 knot spans. These maps clearly indicate that the major error source is located at the singularity. Furthermore, the global effectivity index is between 1.12 and 1.17 for all meshes.

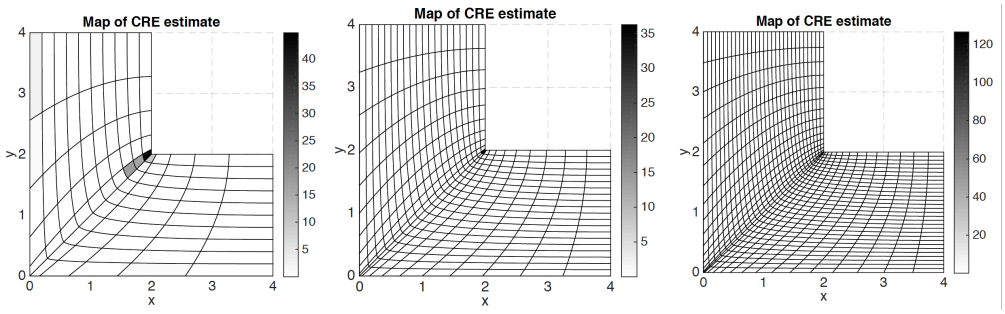

Figure 4.33: Map of the CRE error estimate for the L-shape domain and with various discretizations: 10×10 (left), 20×20 (center), and 30×30 (right) knot spans.

In addition, we show in Figures 4.34 and 4.35 the CRE error estimation results obtained when considering a highly graded IGA mesh, with two levels mesh distorsion. These are obtained by changing geometry lengths (resulting in a small re-intrant corner on the top right of the structure) the while keeping the problem unchanged. Here again, the estimate indicates the correct distribution of the error even though local effectivity indices are a bit higher.

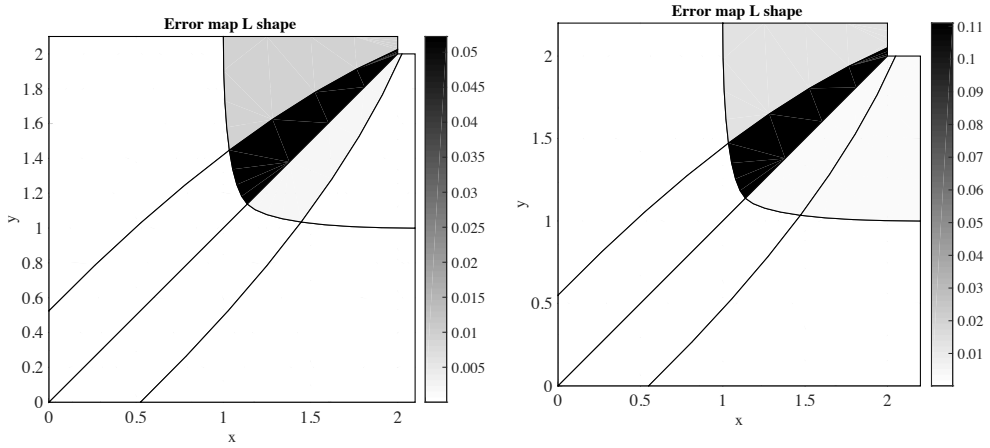

Figure 4.34: Map of the CRE error estimate for the L-shape domain with highly graded mesh.

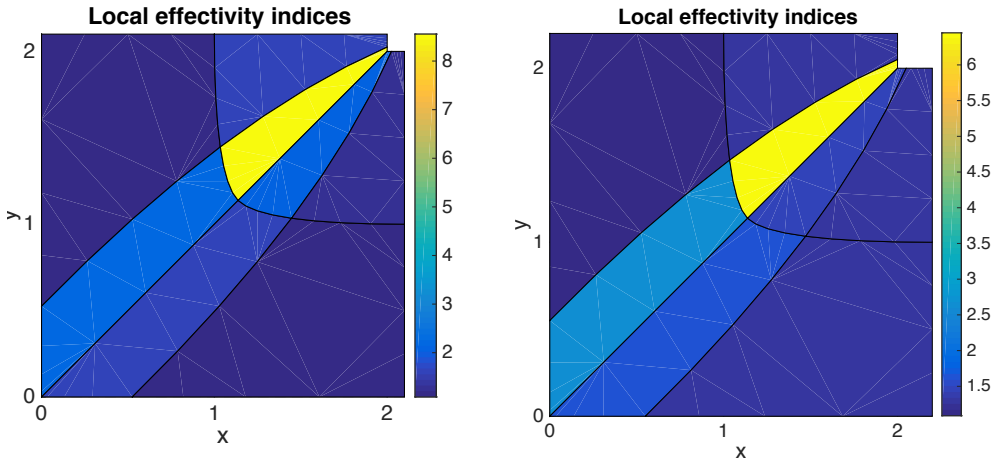

Figure 4.35: Local effectivity indices for the L-shape domain with highly graded mesh.

4.3.3 Example 3: elasticity problem on a 3D structure

Eventually, we consider the 3D geometry shown in Figure 4.36. It is a quarter of hollow cylinder with height $h = 3$, external radius $R_e = 4$, and internal radius $R_i = 1$. A uniform body force $f_d = 1$ is applied in the domain Ω, while homogeneous Dirichlet boundary conditions are prescribed on the whole boundary $\partial\Omega$. The approximate solution is given in Figure 4.37.

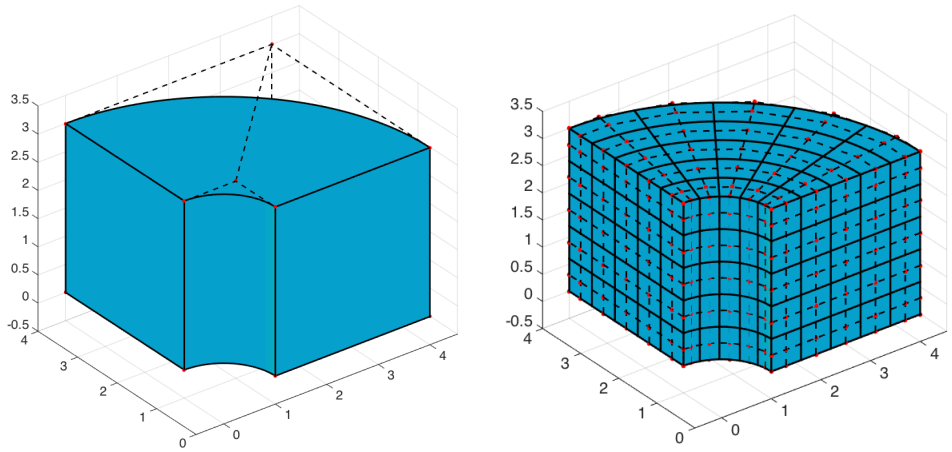

Figure 4.36: IGA representation of the 3D geometry and mesh.

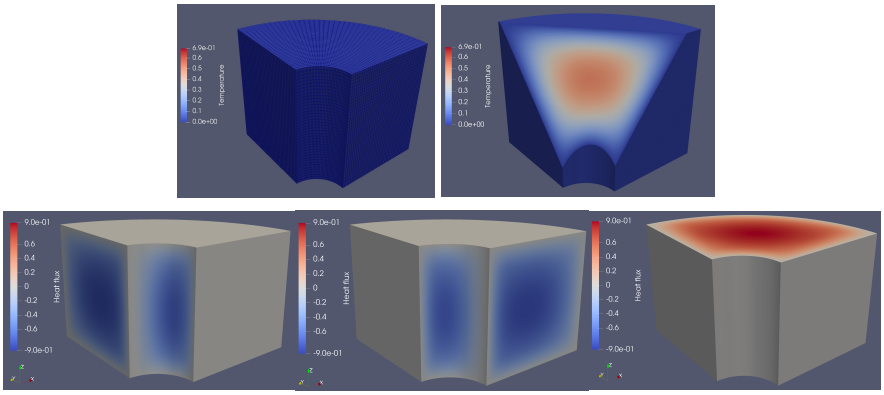

Figure 4.37: Approximate IGA solution: temperature (top), and flux (bottom).

The map of the CRE estimate is given in Figure 4.38. The global effectivity index is 1.17. This example thus shows that the a posteriori error estimation approach can be extended to 3D problems, still with the same level of accuracy and robustness.

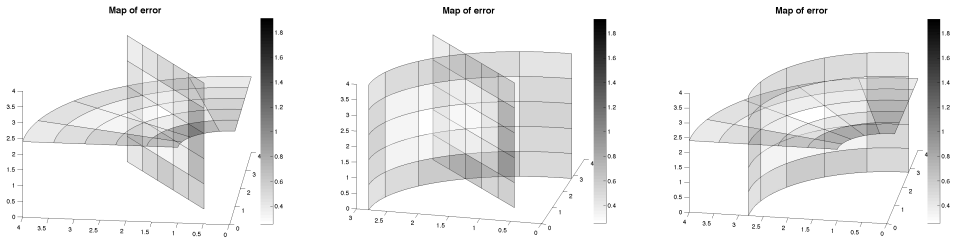

Figure 4.38: Map of the CRE estimate.

4.4 Conclusion

In this chapter, we presented a general procedure based on the CRE framework for the computation of guaranteed and accurate *a posteriori* error estimates for IGA simulations of linear mechanics models. This is the first tool of this kind in the literature. It was shown that the main technical point, which is the construction of equilibrated flux/stress fields, could be performed from an extension of the hybrid-flux technique classically employed in the FEA context. This requires a few additional technicalities in order to take into account the specific features of IGA basis functions. Numerical results confirmed the performance and potential of the approach.

Chapter 5

Coupling PGD with IGA

Contents

5.1 Introduction 95
5.2 Parametrized IGA formulation 98
5.2.1 Model problem with parametrized geometry 98
5.2.2 IGA formulation 98
5.2.3 Parametrized mapping 100
5.3 PGD model reduction: computation and post-processing . . 101
5.3.1 Approximate PGD solution 101
5.3.2 Post-processing of the PGD solution 104
5.4 Error estimation and adaptive process 105
5.4.1 Recovery of equilibrated fields 106
5.4.2 Adaptive algorithm 107
5.5 Numerical results 110
5.5.1 Computation of the torsion stiffness of a parametrized NACA profile 110
5.5.2 Parametrized 3D geometry 117
5.6 Conclusion 119

5.1 Introduction

In this IGA context and assuming no topological changes, the parametrization of the geometry may be naturally implemented using a parametrized mapping from the IGA

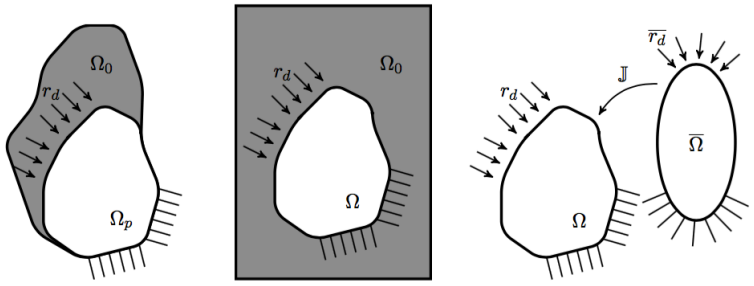

Figure 5.1: Possible numerical methods to deal with evolving geometries: boundary tracking method (left), immersed boundary method (center), and mapping from a reference shape (right).

parametric space to the physical space, without any remeshing, and with design variables associated to coordinates (and potentially weights) of control points. This mapping, which is defined as a function of a finite number of parameters, is therefore simplified compared to the FEA context in which alternative techniques have been investigated in order to address evolving geometries; let us cite fictitious domain or immersed boundary methods where the computational domain is extended from the actual shape to a fixed exterior domain [HM03, Can07, NCS11, NP18], and boundary tracking methods with explicit description of the boundary [CNLB16] (see Figure 5.1). Here, the admissible shapes are taken to be images of a fixed reference shape under a smooth, invertible mapping using IGA functions. The state equations are then mapped back to the reference domain and become parameter-dependent PDEs on a fixed domain. Consequently, the IGA mesh being automatically adapted from the parametrized geometry, difficulties relating to geometric variability are removed and time-consuming remeshing procedures are avoided. From this framework, we propose to couple IGA with PGD model reduction. PGD extra-coordinates are then related to the coordinates and weights of control points (at the coarsest mesh level), and separation of variables is introduced between space and geometry variables. This enables to obtain virtual charts for shape optimization, with explicit and continuous de- pendency of the solution to design variables. Shape sensitivities can then be performed in a straightforward manner.

As any numerical method, the proposed IGA-PGD method is associated with several error sources. These need to be effectively assessed and controlled to ensure the quality of the results, and then permit the industrial transfer and use of the numerical procedure for robust optimization and design. This is a main challenge identified in the report of

the NSF *Simulation-Based Engineering Science* panel [OFJ+06].

In particular, shape optimization being concerned with finding a geometric shape that is optimal with respect to some cost functional that depends explicitly or implicitly on the shape, specific quantities related to the cost functional need to be carefully computed. In order to control the quality of the approximation, and as an additional scientific contribution in the thesis, we introduce verification tools based on the Constitutive Relation Error concept. It provides for a general framework to obtain guaranteed, accurate and fully computable bounds on global error (in the energy norm) or on specific quantities of interest (goal-oriented error estimation) using adjoint-based techniques [PP97, PO99, BR01, GS02]. Here we use similar tools as those described in [LC11, CL12, LC12, CPAL17] and which use the CRE concept to address robust *a posteriori* error estimation when using PGD. It is based on the processing of the approximate PGD solution at hand. Furthermore, it enables to split error sources between PGD truncation and discretization errors, which helps driving adaptive algorithms to save CPU time and memory space. Let us note that alternative verification tools have been investigated in the context of PGD [ACDH10, Alm13, AGZ+15], but they usually focus on PGD truncation error alone.

We propose here to extend the technique proposed in [CPAL17] to parametrized geometry, and to the context of IGA. To address the second point, we refer to a recent work that introduced *a posteriori* error estimation based on CRE for IGA approximations [TCHM18]. Its uses a hybrid-flux technique, over the IGA parametric domain and considering individual local problems on each knot span, in order to construct a perfectly equilibrated flux field from the IGA flux field, which is a mandatory procedure to recover strict bounds on discretization error. Consequently, the verification procedure we propose for the IGA-PGD method provides guaranteed error bounds involving both discretization error and truncation error in the PGD modal representation. It thus certifies the quality of the IGA-PGD approximation (globally or on specific outputs of interest) over the whole set of possible geometry configurations. It also enables to drive a greedy adaptive algorithm which optimizes the computational effort for a prescribed error tolerance (i.e. correct computations are performed at the correct cost), by defining a suitable PGD approximation in terms of required number of terms in the modal representation of the solution, but also in terms of the discretization meshes used to compute modes. Let us note that splitting PGD truncation and discretization errors is of major interest here as the mesh can be highly distorted for some geometry parameter ranges that involve large deformations of shapes.

5.2 Parametrized IGA formulation

5.2.1 Model problem with parametrized geometry

We consider a family of physical open bounded domains $\Omega(\mathbf{p}) \in \mathbb{R}^d$ (d=1, 2 or 3), with boundary $\partial\Omega(\mathbf{p})$, whose geometry is parametrized by a finite-dimensional vector $\mathbf{p} \in \mathcal{P}$ of parameters which drive the variations of the geometry. Over this parametrized domain, we define a linear elliptic problem, that is the Poisson equation with prescribed boundary conditions. We assume that homogeneous Dirichlet boundary conditions are prescribed on a non-zero part $\partial_u\Omega(\mathbf{p}) \subset \partial\Omega(\mathbf{p})$, while Neumann boundary conditions with given normal flux $F_d \in L^2(\partial_q\Omega)$ are prescribed on the complementary part $\partial_q\Omega(\mathbf{p}) \subset \partial\Omega(\mathbf{p})$. A given source term $f_d \in L^2(\Omega)$ may also be active in $\Omega(\mathbf{p})$. The problem thus consists in finding, for any value of the parameter set $\mathbf{p}$, the field $u_\mathbf{p}$ solution to:

$$-\Delta u_\mathbf{p} = f_d \quad \text{in } \Omega(\mathbf{p}) \quad ; \quad u_\mathbf{p} = 0 \quad \text{on } \partial_u\Omega(\mathbf{p}) \quad ; \quad \frac{\partial u_\mathbf{p}}{\partial \mathbf{n}} = F_d \quad \text{on } \partial_q\Omega(\mathbf{p}) \tag{5.1}$$

We define $\mathbf{q_p} = \nabla u_\mathbf{p}$ the flux associated to $u_\mathbf{p}$. Introducing the functional space $\mathcal{U}_\mathbf{p} = H^1_0(\Omega(\mathbf{p})) = \{v \in H^1(\Omega(\mathbf{p})), v_{|\partial_u\Omega(\mathbf{p})} = 0\}$, the weak formulation of the problem reads:

$$\text{Find } u_\mathbf{p} \in \mathcal{U}_\mathbf{p} \text{ such that } a_\mathbf{p}(u_\mathbf{p}, v) = \ell_\mathbf{p}(v) \quad \forall v \in \mathcal{U}_\mathbf{p} \tag{5.2}$$

where parametrized bilinear form $a_\mathbf{p}(\cdot,\cdot)$ and linear form $\ell_\mathbf{p}(\cdot)$ are defined as:

$$a_\mathbf{p}(u,v) = \int_{\Omega(\mathbf{p})} \nabla u \cdot \nabla v \mathrm{d}\mathbf{x} \quad ; \quad \ell_\mathbf{p}(v) = \int_{\Omega(\mathbf{p})} f_d v \mathrm{d}\mathbf{x} + \int_{\partial_q\Omega(\mathbf{p})} F_d v \mathrm{d}S \tag{5.3}$$

From the previous assumptions, and referring to the Lax-Milgram theorem, the mathematical problem (6.23) has a unique solution $u_\mathbf{p}$, for any configuration of the geometry, which will be taken as the reference when dealing with discretization error in the remainder of the thesis. In addition, we introduce the energy norm $\|u\| = \sqrt{a_\mathbf{p}(u,u)}$ which is equivalent to the H^1-norm in $\mathcal{U}_\mathbf{p}$. This norm, which is directly linked to the properties of the problem operator, will be used in order to define a global measure of the discretization error.

5.2.2 IGA formulation

We consider the usual context in which the geometry of the physical domain $\Omega(\mathbf{p})$ is described from CAD tools, that involve B-Spline functions or more generally NURBS functions. Using tensor product spaces with multi-variate functions, these enable to represent complex curves $\mathbf{C}$ (in 1D), surfaces $\mathbf{S}$ (in 2D), or volumes $\mathbf{V}$ (in 3D) from a set $\{N_I\}_{I=1}^n$ (resp. $\{R_I\}_{I=1}^n$) of B-Spline (resp. NURBS) functions. The B-Spline functions

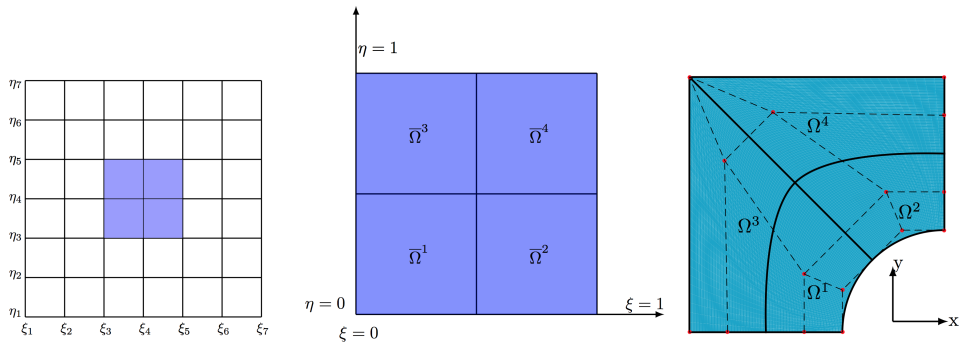

Figure 5.2: Index space (left), parametric space (center) and physical space with control mesh in dashed line (right) in a 2D representation with knot vectors $\boldsymbol{\Xi}^1 = \{0, 0, 0, 0.5, 1, 1, 1\}$ and $\boldsymbol{\Xi}^2 = \{0, 0, 0, 0.5, 1, 1, 1\}$.

are constructed from knot vectors $\boldsymbol{\Xi}$ in each space dimension. The n control points $\mathbf{B}_I$ (with coordinate vector of size $d \times 1$) enable to fully define the geometrical entity, even though they are not interpolatory. A piecewise linear interpolation between these control points defines the so-called control mesh (or polygon). Furthermore, a transformation of the geometrical entity is easily obtained by applying the transformation directly to control points; their coordinates thus define control variables, and they will be directly linked with the geometry parameter vector $\mathbf{p}$ in the remainder of the thesis. We also note that due to the local support of B-Spline and NURBS functions, moving a single control point would modify the geometry only locally.

From a given physical domain Ω with geometry described by the tensorization of d knot vectors $\boldsymbol{\Xi}^j$ $(j = 1, \ldots, d)$ defined in each space dimension, several description spaces may be used (Figure 5.2):

Following the classical isoparametric framework, a geometrical mapping $\mathbf{F}$ transforms coordinates of the parametric space $\overline{\Omega}$ to the physical space Ω, and conversely. In the IGA framework, this mapping is mainly used for numerical integration purposes. In the present work, it will also be intensively used to define the parametrization of domains $\Omega(\mathbf{p})$ (see Section 5.2.3).

In its original formulation, IGA consists of searching an approximate solution to (6.23) by means of a Galerkin formulation and a finite dimensional subspace of $\mathcal{U}_{\mathbf{p}}$ spanned by the same set of B-Splines/NURBS basis functions as these describing the geometry of $\Omega(\mathbf{p})$. We thus introduce the functional space $\mathcal{U}^h_{\mathbf{p}} = \text{Span}\{\varphi_I, 1 \leq I \leq n\} \cap \mathcal{U}_{\mathbf{p}}$, where

functions φ_I correspond to sets $\{N_I\}_{I=1}^n$ or $\{R_I\}_{I=1}^n$. The IGA formulation then reads:

$$\text{Find } u_{\mathbf{p}}^h \in \mathcal{U}_{\mathbf{p}}^h \text{ such that } a_{\mathbf{p}}(u_{\mathbf{p}}^h, v^h) = \ell_{\mathbf{p}}(v^h) \quad \forall v^h \in \mathcal{U}_{\mathbf{p}}^h \tag{5.4}$$

and leads to a linear system to solve.

5.2.3 Parametrized mapping

We now focus on the parametrization of evolving domains $\Omega(\mathbf{p})$. As detailed previously, considering that geometry parameters are directly linked to coordinates of control points $\mathbf{B}_I$, it is natural to involve the isoparametric invertible global mapping $\mathbf{F}_{\mathbf{p}}$ defined as:

$$\mathbf{F}_{\mathbf{p}} : \overline{\Omega} \to \Omega(\mathbf{p}) \quad ; \quad \boldsymbol{\xi} \mapsto \mathbf{x} = \mathbf{F}_{\mathbf{p}}(\boldsymbol{\xi}) = \sum_{I=1}^{n} \mathbf{B}_I(\mathbf{p}) N_I(\boldsymbol{\xi}) \quad (\text{or } = \sum_{I=1}^{n} \mathbf{B}_I(\mathbf{p}) R_I(\boldsymbol{\xi})) \tag{5.5}$$

We introduce the associated Jacobian matrix $\mathbb{J}_{\mathbf{p}} = \partial \mathbf{x} / \partial \boldsymbol{\xi}$ and Jacobian $J_{\mathbf{p}} = \det(\mathbb{J}_{\mathbf{p}})$, which are directly obtained from derivatives of N_I or R_I. Then, noticing that $\Omega(\mathbf{p})$ is the image of the reference parametric domain $\overline{\Omega}$ through the mapping $\mathbf{F}_{\mathbf{p}}$ (see Figure 5.3), the weak formulation (5.4) with moving domain geometry can be mapped back to the fixed domain $\overline{\Omega}$. Introducing the notation $z(\mathbf{x}) = \overline{z}(\boldsymbol{\xi})$, it yields the following formulation:

$$\text{Find } \overline{u}_{\mathbf{p}}^h \in \overline{\mathcal{U}}^h \text{ such that } \overline{a}_{\mathbf{p}}(\overline{u}_{\mathbf{p}}^h, \overline{v}^h) = \overline{\ell}_{\mathbf{p}}(\overline{v}^h) \quad \forall \overline{v}^h \in \overline{\mathcal{U}}^h \tag{5.6}$$

with:

$$\begin{aligned} \overline{a}_{\mathbf{p}}(\overline{u}_{\mathbf{p}}^h, \overline{v}^h) &= \int_{\overline{\Omega}} \mathbb{J}_{\mathbf{p}}^{-T} \nabla_{\boldsymbol{\xi}} \overline{u}_{\mathbf{p}}^h \cdot \mathbb{J}_{\mathbf{p}}^{-T} \nabla_{\boldsymbol{\xi}} \overline{v}^h J_{\mathbf{p}} \mathrm{d}\boldsymbol{\xi} = \int_{\overline{\Omega}} (J_{\mathbf{p}} \mathbb{J}_{\mathbf{p}}^{-1} \mathbb{J}_{\mathbf{p}}^{-T}) \nabla_{\boldsymbol{\xi}} \overline{u}_{\mathbf{p}}^h \cdot \nabla_{\boldsymbol{\xi}} \overline{v}^h \mathrm{d}\boldsymbol{\xi} \\ \overline{\ell}_{\mathbf{p}}(\overline{v}^h) &= \int_{\overline{\Omega}} \overline{f}_d \overline{v}^h J_{\mathbf{p}} \mathrm{d}\boldsymbol{\xi} + \int_{\partial_q \overline{\Omega}} \overline{F}_d \overline{v}^h J_{\mathbf{p}}^S \mathrm{d}S_\xi = \int_{\overline{\Omega}} J_{\mathbf{p}} \overline{f}_d \overline{v}^h \mathrm{d}\boldsymbol{\xi} + \int_{\partial_q \overline{\Omega}} J_{\mathbf{p}}^S \overline{F}_d \overline{v}^h \mathrm{d}S_\xi \end{aligned} \tag{5.7}$$

This formulation thus defines a parameter-dependent PDE on a fixed domain $\overline{\Omega}$, with parametrized symmetric operator $\mathbb{D}_{\mathbf{p}} = J_{\mathbf{p}} \mathbb{J}_{\mathbf{p}}^{-1} \mathbb{J}_{\mathbf{p}}^{-T}$, body force field $J_{\mathbf{p}} \overline{f}_d$ in $\overline{\Omega}$, and Neumann boundary conditions $J_{\mathbf{p}}^S \overline{F}_d$ on $\partial_q \overline{\Omega}$.

Remark. For elasticity problems, the strain operator $\epsilon(\mathbf{u})$ would not enable to get such a simple formulation (5.6) on a fixed domain, as $\epsilon(\mathbf{u}) = \nabla_s \mathbf{u} = \frac{1}{2}(\mathbb{J}^{-T} \nabla_{\boldsymbol{\xi}} \overline{\mathbf{u}} + \nabla_{\boldsymbol{\xi}}^T \overline{\mathbf{u}} \mathbb{J}^{-1})$. To circumvent this issue, a solution consists in using a variational formulation for elasticity involving the full gradient $\nabla \mathbf{u}$ of the displacement $\mathbf{u}$ (and therefore breaking the symmetry of $\epsilon(\mathbf{u})$), the symmetry being then restored by the Hooke tensor when using the Voigt notation.

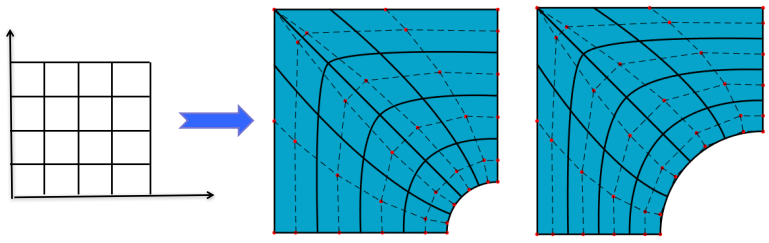

Figure 5.3: Parametrized mapping between the reference domain $\overline{\Omega}$ (IGA parametric space) and the physical domain $\Omega(\mathbf{p})$.

From the use of IGA parametrization, we may expect that the solution $\overline{u}^h_{\mathbf{p}}$ to (5.6) has a regular continuous evolution with respect to $\mathbf{p}$ in the reference parametric space $\overline{\Omega}$. Nevertheless, even defined on a fixed domain, solving (5.6) for any value of $\mathbf{p}$ (i.e. any shape geometry) may still be an expensive and challenging computational task using brute force (grid-based) approaches. This is due to multi-query issues with a possibly large number of geometry parameters. In Section 5.3, we introduce an alternative numerical approach based on PGD model reduction.

5.3 PGD model reduction: computation and post-processing

5.3.1 Approximate PGD solution

The reformulation (5.6) of the parametric problem on a fixed physical domain yields a weak formulation in a tensor product space (product of space functions and parametric functions). This situation is suited to the use of the PGD model reduction technique for the construction of a tensor product approximation (separated representation) of the solution. This technique automatically captures reduced bases of space functions and parametric functions which are optimal for the representation of the solution. It is made computationally tractable by introducing separated representations of variational forms, resulting from separated representations.
The first step of PGD consists in the definition of a global weak formulation over the tensor product space, which is here $\overline{\mathcal{U}}^h \otimes L^2(\mathcal{P})$. It reads:

$$\text{Find } \overline{u}^h \in \overline{\mathcal{U}}^h \otimes L^2(\mathcal{P}) \text{ such that } \overline{A}(\overline{u}^h, \overline{v}^h) = \overline{L}(\overline{v}^h) \quad \forall \overline{v}^h \in \overline{\mathcal{U}}^h \tag{5.8}$$

with:

$$\begin{aligned}\overline{A}(\overline{u}^h,\overline{v}^h) &= \int_{\mathcal{P}} \overline{a}_{\mathbf{p}}(\overline{u}^h,\overline{v}^h)\mathrm{d}\mathbf{p} = \int_{\mathcal{P}}\int_{\overline{\Omega}} (J_{\mathbf{p}}\mathbb{J}_{\mathbf{p}}^{-1}\mathbb{J}_{\mathbf{p}}^{-T})\nabla_{\boldsymbol{\xi}}\overline{u}^h\cdot\nabla_{\boldsymbol{\xi}}\overline{v}^h\mathrm{d}\boldsymbol{\xi}\mathrm{d}\mathbf{p}\\ \overline{L}(\overline{v}^h) &= \int_{\mathcal{P}} \overline{\ell}_{\mathbf{p}}(\overline{v}^h)\mathrm{d}\mathbf{p} = \int_{\mathcal{P}}\left[\int_{\overline{\Omega}} J_{\mathbf{p}}\overline{f}_d\overline{v}^h\mathrm{d}\boldsymbol{\xi} + \int_{\partial_q\overline{\Omega}} J_{\mathbf{p}}^S\overline{F}_d\overline{v}^h\mathrm{d}S_\xi\right]\mathrm{d}\mathbf{p}\end{aligned} \tag{5.9}$$

The basic idea in model reduction using PGD it then to *a priori* construct an approximation of the solution $\overline{u}^h(\boldsymbol{\xi},\mathbf{p})$ as a separated variables representation defined in tensor product spaces (canonical format), i.e. a finite sum of products of separable functions (or modes). We consider here such a representation associated with low-rank separated structure for variables in space $\boldsymbol{\xi}$ and geometry parameters $\mathbf{p}$. It reads:

$$\overline{u}^h(\boldsymbol{\xi},\mathbf{p}) \approx \overline{u}^h_m(\boldsymbol{\xi},\mathbf{p}) = \sum_{i=1}^{m}\overline{\psi}^h_i(\boldsymbol{\xi})G_i(\mathbf{p}) \quad \text{with } \overline{\psi}^h_i \in \overline{\mathcal{U}}^h, G_i(\mathbf{p}) \in L^2(\mathcal{P}) \tag{5.10}$$

$m \in \mathbb{N}^*$ being the rank (or order) of the PGD approximation.

Remark. Even though a discretization over the geometry parameter space $\mathcal{P}$ is introduced to numerically compute and store functions $G_i(\mathbf{p})$, it is not explicitly exhibited as it is not associated with a given numerical approximation method that we would like to adapt. Indeed, the associated mesh size can be taken a small as needed with low CPU cost (no ODE or PDE is solved to get $G_i(\mathbf{p})$). In the numerical results reported in Section 5.5, we will consider a very fine discretization grid over $\mathcal{P}$ in order to safely neglect the error due to the numerical approximation over this space.

Among the various methods which have been introduced so far to compute PGD modes and build an approximate separated representation of the solution $\overline{u}^h$ (see [CAC10, Nou10] for instance), we use a classical one referred to as progressive Galerkin-based PGD method. It operates in an iterative strategy based on the progressive construction of successive order 1 corrections, and defines Galerkin approximations in tensor product spaces from the full weak formulation (6.25). Assuming that an order $(m-1)$ PGD decomposition $\overline{u}^h_{m-1}$ is known, the order m decomposition sum is searched as:

$$\overline{u}^h_m(\boldsymbol{\xi},\mathbf{p}) = \overline{u}^h_{m-1}(\boldsymbol{\xi},\mathbf{p}) + \overline{\psi}^h(\boldsymbol{\xi})G(\mathbf{p}) \tag{5.11}$$

where the new functions $\overline{\psi}^h \in \overline{\mathcal{U}}^h$ and $G \in L^2(\mathcal{P})$ are unknown functions to be determined. The Galerkin approach then implies that these functions verify the following Galerkin orthogonality conditions:

$$\overline{A}(\overline{u}^h_{m-1}+\overline{\psi}^hG,\delta\overline{v}^h) = \overline{L}(\delta\overline{v}^h) \quad \text{with } \delta\overline{v}^h = \delta\overline{\psi}^hG+\overline{\psi}^h\delta G \text{ (tangent space)}\ ,\ \forall\delta\overline{\psi}^h \in \overline{\mathcal{U}}^h, \forall\delta G \in L^2(\mathcal{P}) \tag{5.12}$$

or, equivalently, the following stationarity conditions:

$$\begin{aligned} &\overline{A}(\overline{u}^h_{m-1} + \overline{\psi}^h G, \delta\overline{\psi}^h G) = \overline{L}(\delta\overline{\psi}^h G) \quad \forall \delta\overline{\psi}^h \in \overline{\mathcal{U}}^h \\ &\overline{A}(\overline{u}^h_{m-1} + \overline{\psi}^h G, \overline{\psi}^h \delta G) = \overline{L}(\overline{\psi}^h \delta G) \quad \forall \delta G \in L^2(\mathcal{P}) \end{aligned} \tag{5.13}$$

Problem (5.13) is a complex nonlinear coupled problem which can be interpreted as a pseudo-eigenvalue problem; it may thus be solved using specific iterative algorithms inspired from classical power iterations algorithms dedicated to eigenvalue problems or dominant subspace methods [Nou10]. In the present work, we use the fixed-point iteration method (also called alternating direction algorithm in an optimization context). For each mode $m \in \mathbb{N}^*$, starting from an *ad hoc* initialization $(\overline{\psi}^{h(0)}, G^{(0)})$ at iteration 0, one builds a sequence $(\overline{\psi}^{h(k)}, G^{(k)})_{k\in\mathbb{N}^*}$ with the following power sub-iterations algorithm requiring the solution of a sequence of simple low-dimensional problems at each sub-iteration k:

- compute $G^{(k)} \in L^2(\mathcal{P})$ such that:

$$\overline{A}(\overline{u}^h_{m-1} + \overline{\psi}^{h(k-1)} G^{(k)}, \overline{\psi}^{h(k-1)} \delta G) = \overline{L}(\overline{\psi}^{h(k-1)} \delta G) \quad \forall \delta G \in L^2(\mathcal{P}) \tag{5.14}$$

  Problem (5.14) is associated with a scalar algebraic equation over the geometry parameter space $\mathcal{P}$;

- compute $\psi^{h(k)} \in \overline{\mathcal{U}}^h$ such that:

$$\overline{A}(\overline{u}^h_{m-1} + \overline{\psi}^{h(k)} G^{(k)}, \delta\overline{\psi}^h G^{(k)}) = \overline{L}(\delta\overline{\psi}^h G^{(k)}) \quad \forall \delta\overline{\psi}^h \in \overline{\mathcal{U}}^h \tag{5.15}$$

  Problem (5.15) is associated with the solution of a space IGA problem over the domain $\overline{\Omega}$.

Sub-iterations may be performed until convergence of the fixed point method (up to a given tolerance) is reached. In practice, the power sub-iterations algorithm converges quite fast and generally does not require more than a few iterations to obtain a good approximation. Here, we choose an alternative strategy and stop sub-iterations after a given number k_{max} (we take $k_{max} = 5$ in the numerical experiments shown in Section 5.5). Furthermore, the geometry parameter function $G^{(k)}$ is normalized at each sub-iteration k so that the magnitude of PGD mode m is supported by space function $\psi^{h(k)}$ alone.

Remark. Several possible variants, which will not be considered here, can be introduced in the progressive Galerkin-based PGD approach in order to capture a better approximation of the optimal PGD decomposition (that would be obtained by computing all

modes simultaneously and not progressively). In particular, for any mode $m \in \mathbb{N}^*$: (i) space function ψ_m^h may be orthogonalized with respect to the existing space basis $\{\psi_i^h\}_{i=1}^{m-1}$; (ii) geometry parameter functions G_i associated with previously computed modes $i \leq m-1$ may be updated before starting the power sub-iterations algorithm for computing mode m, in order to satisfy a stronger Galerkin orthogonality condition (this preliminary stage actually corresponds to a low-cost POD step).

For the PGD computation to be effective, all terms appearing in (6.25) should be written with separated form between space variables $\boldsymbol{\xi}$ and geometry parameter variables $\mathbf{p}$. Consequently, and as the Jacobian matrix usually depends on $\boldsymbol{\xi}$ due to the high order of IGA basis functions, we use SVD or HOSVD in order to get:

$$J_{\mathbf{p}}(\boldsymbol{\xi})\mathbb{J}_{\mathbf{p}}^{-1}(\boldsymbol{\xi})\mathbb{J}_{\mathbf{p}}^{-T}(\boldsymbol{\xi}) = \sum_{j=1}^{N_D} T_j^D(\boldsymbol{\xi})S_j^D(\mathbf{p}) \quad ; \quad J_{\mathbf{p}}(\boldsymbol{\xi}) = \sum_{j=1}^{N_J} T_j^J(\boldsymbol{\xi})S_j^J(\mathbf{p}) \quad ; \quad J_{\mathbf{p}}^S(\boldsymbol{\xi}) = \sum_{j=1}^{N_{J_S}} T_j^{J_S}(\boldsymbol{\xi})S_j^{J_S}(\mathbf{p}) \tag{5.16}$$

This enables to compute integrals over separate domains $\overline{\Omega}$ and $\mathcal{P}$. A PGD on a known field could also be used to separate variables.

5.3.2 Post-processing of the PGD solution

We now write more precisely the problems (5.14) and (5.15) to be solved during the fixed-point procedure. For clarity reasons, we do not introduce sub-iteration indices. On the one hand, the geometry parameter problem associated to (5.14) reads:

$$\overline{A}(\overline{\psi}^h G, \overline{\psi}^h \delta G) = \overline{L}(\overline{\psi}^h \delta G) - \overline{A}(\sum_{i=1}^{m-1} \overline{\psi}_i^h G_i, \overline{\psi}^h \delta G) \quad \forall \delta G \in L^2(\mathcal{P}) \tag{5.17}$$

so that:

$$\begin{aligned} \int_{\mathcal{P}} \Bigg[\left(\int_{\overline{\Omega}} \mathbb{D}_{\mathbf{p}} \nabla_{\boldsymbol{\xi}} \overline{\psi}^h \cdot \nabla_{\boldsymbol{\xi}} \overline{\psi}^h \mathrm{d}\boldsymbol{\xi} \right) G + \sum_{i=1}^{m-1} \left(\int_{\overline{\Omega}} \mathbb{D}_{\mathbf{p}} \nabla_{\boldsymbol{\xi}} \overline{\psi}_i^h \cdot \nabla_{\boldsymbol{\xi}} \overline{\psi}^h \mathrm{d}\boldsymbol{\xi} \right) G_i \\ - \int_{\overline{\Omega}} J_{\mathbf{p}} \overline{f}_d \overline{\psi}^h \mathrm{d}\boldsymbol{\xi} - \int_{\partial_q \overline{\Omega}} J_{\mathbf{p}}^S \overline{F}_d \overline{\psi}^h \mathrm{d}S_\xi \Bigg] \delta G \mathrm{d}\mathbf{p} = 0 \quad \forall \delta G \in L^2(\mathcal{P}) \end{aligned} \tag{5.18}$$

On the other hand, the problem in space associated to (5.15) reads:

$$\overline{A}(\overline{\psi}^h G, \delta\overline{\psi}^h G) = \overline{L}(\delta\overline{\psi}^h G) - \overline{A}(\sum_{i=1}^{m-1} \overline{\psi}_i^h G_i, \delta\overline{\psi}^h G) \quad \forall \delta\overline{\psi}^h \in \overline{\mathcal{U}}^h \tag{5.19}$$

so that:

$$\begin{aligned}&\int_{\overline{\Omega}}\left[\left(\int_{\mathcal{P}}\mathbb{D}_{\mathbf{p}}G^2\mathrm{d}\mathbf{p}\right)\nabla_{\boldsymbol{\xi}}\overline{\psi}^h\cdot\nabla_{\boldsymbol{\xi}}\delta\overline{\psi}^h+\sum_{i=1}^{m-1}\left(\int_{\mathcal{P}}\mathbb{D}_{\mathbf{p}}G_iG\mathrm{d}\mathbf{p}\right)\nabla_{\boldsymbol{\xi}}\overline{\psi}_i^h\cdot\nabla_{\boldsymbol{\xi}}\delta\overline{\psi}^h\right]\mathrm{d}\boldsymbol{\xi}\\&-\int_{\overline{\Omega}}\left(\int_{\mathcal{P}}J_{\mathbf{p}}G\mathrm{d}\mathbf{p}\right)\overline{f}_d\delta\overline{\psi}^h\mathrm{d}\boldsymbol{\xi}-\int_{\partial_q\overline{\Omega}}\left(\int_{\mathcal{P}}J_{\mathbf{p}}^SG\mathrm{d}\mathbf{p}\right)\overline{F}_d\delta\overline{\psi}^h\mathrm{d}S_\xi=0\quad\forall\delta\overline{\psi}^h\in\overline{\mathcal{U}}^h\end{aligned}\tag{5.20}$$

Solving elementary space linear problems over the fixed domain $\overline{\Omega}$ and with IGA basis functions, it is straightforward to recover (non-unique) flux fields verifying:

$$\begin{aligned}\int_{\overline{\Omega}}\overline{\mathbf{q}}_j^J\cdot\nabla_{\boldsymbol{\xi}}\delta\overline{\psi}^h\mathrm{d}\boldsymbol{\xi}&=\int_{\overline{\Omega}}T_j^J\overline{f}_d\delta\overline{\psi}^h\mathrm{d}\boldsymbol{\xi}\quad\forall j\in[1,N_J]\\\int_{\overline{\Omega}}\overline{\mathbf{q}}_j^{J_S}\cdot\nabla_{\boldsymbol{\xi}}\delta\overline{\psi}^h\mathrm{d}\boldsymbol{\xi}&=\int_{\partial_q\overline{\Omega}}T_j^{J_S}\overline{F}_d\delta\overline{\psi}^h\mathrm{d}S_\xi\quad\forall j\in[1,N_{J_S}]\end{aligned}\tag{5.21}$$

Consequently, using (5.16), (5.20) can be recast as:

$$\begin{aligned}&\int_{\overline{\Omega}}\left[\left(\int_{\mathcal{P}}\mathbb{D}_{\mathbf{p}}G^2\mathrm{d}\mathbf{p}\right)\nabla_{\boldsymbol{\xi}}\overline{\psi}^h+\sum_{i=1}^{m-1}\left(\int_{\mathcal{P}}\mathbb{D}_{\mathbf{p}}G_iG\mathrm{d}\mathbf{p}\right)\nabla_{\boldsymbol{\xi}}\overline{\psi}_i^h\right.\\&\left.-\sum_{j=1}^{N_J}\left(\int_{\mathcal{P}}S_j^JG\mathrm{d}\mathbf{p}\right)\overline{\mathbf{q}}_j^J-\sum_{j=1}^{N_{J_S}}\left(\int_{\mathcal{P}}S_j^{J_S}G\mathrm{d}\mathbf{p}\right)\overline{\mathbf{q}}_j^{J_S}\right]\cdot\nabla_{\boldsymbol{\xi}}\delta\overline{\psi}^h\mathrm{d}\boldsymbol{\xi}=0\quad\forall\delta\overline{\psi}^h\in\overline{\mathcal{U}}^h\end{aligned}\tag{5.22}$$

This shows that for each mode m_0, and provided sub-iterations of the fixed-point procedure are stopped after solving space problem (5.15), the field $\overline{\mathbf{z}}_{m_0}^h$ defined as:

$$\begin{aligned}\overline{\mathbf{z}}_{m_0}^h=&\left(\int_{\mathcal{P}}\mathbb{D}_{\mathbf{p}}G_{m_0}^2\mathrm{d}\mathbf{p}\right)\nabla_{\boldsymbol{\xi}}\overline{\psi}_{m_0}^h+\sum_{i=1}^{m_0-1}\left(\int_{\mathcal{P}}\mathbb{D}_{\mathbf{p}}G_iG_{m_0}\mathrm{d}\mathbf{p}\right)\nabla_{\boldsymbol{\xi}}\overline{\psi}_i^h\\&-\sum_{j=1}^{N_J}\left(\int_{\mathcal{P}}S_j^JG_{m_0}\mathrm{d}\mathbf{p}\right)\overline{\mathbf{q}}_j^J-\sum_{j=1}^{N_{J_S}}\left(\int_{\mathcal{P}}S_j^{J_S}G_{m_0}\mathrm{d}\mathbf{p}\right)\overline{\mathbf{q}}_j^{J_S}\end{aligned}\tag{5.23}$$

is self-equilibrated (in the approximate IGA sense) over the fixed domain $\overline{\Omega}$. The set $\{\overline{\mathbf{z}}_{m_0}^h\}_{1\leq m_0\leq m}$ will be used in Section 5.4.1.

5.4 Error estimation and adaptive process

In this section, we wish to define tools in order to assess, for any geometry parameter set $\mathbf{p}$, the error between the exact solution $u_{\mathbf{p}}$ to (6.23) and the approximate solution $u_m^h(\cdot,\mathbf{p})$ computed by means of the IGA-PGD numerical method. For this purpose, we propose to introduce the concept of Constitutive Relation Error (CRE) which has been extensively

applied for verification in FEA. The error field is defined as $e_m^h(\mathbf{x},\mathbf{p}) = u_{\mathbf{p}}(\mathbf{x}) - u_m^h(\mathbf{x},\mathbf{p})$; it may be measured either globally using the energy norm:

$$\mathcal{E}_{glob}(\mathbf{p}) = \|e_m^h(\cdot,\mathbf{p})\| \tag{5.24}$$

or locally on outputs of interest Q, which are linear functionals of u:

$$\mathcal{E}_Q(\mathbf{p}) = Q(e_m^h(\cdot,\mathbf{p})) \tag{5.25}$$

Error sources are twofold: discretization in space using the IGA approximation; truncation at order m of the modal PGD representation.

5.4.1 Recovery of equilibrated fields

We now show how a relevant admissible flux field $\hat{\mathbf{q}}_{\mathbf{p}} \in \times\mathcal{S}_{\mathbf{p}}$ can be recovered from the IGA-PGD approximate solution at hand, enabling to compute CRE estimates on $\mathcal{E}_{glob}(\mathbf{p})$ or $\mathcal{E}_Q(\mathbf{p})$. The equilibrium constraint defined over $\Omega(\mathbf{p})$ in (4.6) can be equivalently recast over the reference domain $\overline{\Omega}$, under the form:

$$\int_{\overline{\Omega}} \overline{\boldsymbol{\tau}} \cdot \mathbb{J}_{\mathbf{p}}^{-T} \nabla_{\boldsymbol{\xi}} \overline{v} J_{\mathbf{p}} \mathrm{d}\boldsymbol{\xi} = \int_{\overline{\Omega}} J_{\mathbf{p}} \mathbb{J}_{\mathbf{p}}^{-1} \overline{\boldsymbol{\tau}} \cdot \nabla_{\boldsymbol{\xi}} \overline{v} \mathrm{d}\boldsymbol{\xi} = \int_{\overline{\Omega}} J_{\mathbf{p}} \overline{f}_d \overline{v} \mathrm{d}\boldsymbol{\xi} + \int_{\partial_q \overline{\Omega}} J_{\mathbf{p}}^S \overline{F}_d \overline{v} \mathrm{d}S_\xi \quad \forall \overline{v} \in \overline{\mathcal{U}} \tag{5.26}$$

The procedure uses the classical hybrid-flux (or EET) technique, extensively used in the FEA context and recently extended to the IGA context in [TCHM18]. It leans on equilibrium properties, in the approximate FE or IGA sense, of available fluxes. When considering IGA approximations alone, the computed flux verifies such weak equilibrium properties. Nevertheless, due to the fact that is uses the full weak formulation (6.25) of the problem, the progressive Galerkin-based PGD technique presented in Section 5.3.1 (or any other variant of this PGD technique) provides an approximate solution $\mathbf{q}_m^h = \nabla u_m^h$ that fails to verify equilibrium equations in any weak sense in space. Consequently, a first step is to recover a relevant field $\boldsymbol{\tau}_{\mathbf{p}}^h$ in $\Omega(\mathbf{p})$, or equivalently $\overline{\boldsymbol{\tau}}_{\mathbf{p}}^h$ in $\overline{\Omega}$, verifying equilibrium in the approximate IGA sense; this reads:

$$\int_{\overline{\Omega}} J_{\mathbf{p}} \mathbb{J}_{\mathbf{p}}^{-1} \overline{\boldsymbol{\tau}}_{\mathbf{p}}^h \cdot \nabla_{\boldsymbol{\xi}} \overline{v}^h \mathrm{d}\boldsymbol{\xi} = \int_{\overline{\Omega}} J_{\mathbf{p}} \overline{f}_d \overline{v}^h \mathrm{d}\boldsymbol{\xi} + \int_{\partial_q \overline{\Omega}} J_{\mathbf{p}}^S \overline{F}_d \overline{v}^h \mathrm{d}S_\xi \quad \forall \overline{v}^h \in \overline{\mathcal{U}}^h \tag{5.27}$$

Using (5.16) and (5.21), the external loading can be directly equilibrated (in the IGA weak sense) with a computable field $\overline{\mathbf{q}}_d$, as:

$$\int_{\overline{\Omega}} J_{\mathbf{p}} \overline{f}_d \overline{v}^h \mathrm{d}\boldsymbol{\xi} + \int_{\partial_q \overline{\Omega}} J_{\mathbf{p}}^S \overline{F}_d \overline{v}^h \mathrm{d}S_\xi = \int_{\overline{\Omega}} \overline{\mathbf{q}}_d \cdot \nabla_{\boldsymbol{\xi}} \overline{v}^h \mathrm{d}\boldsymbol{\xi} \quad \forall \overline{v}^h \in \overline{\mathcal{U}}^h \tag{5.28}$$

with

$$\overline{\mathbf{q}}_d = \sum_{j=1}^{N_J} S_j^J(\mathbf{p})\overline{\mathbf{q}}_j^J + \sum_{j=1}^{N_{J_S}} S_j^{J_S}(\mathbf{p})\overline{\mathbf{q}}_j^{J_S} \tag{5.29}$$

Consequently, it is straightforward that:

$$\overline{\boldsymbol{\tau}}_{\mathbf{p}}^h = J_{\mathbf{p}}^{-1}\mathbb{J}_{\mathbf{p}}\left[\overline{\mathbf{q}}_d + \sum_{m_0=1}^{m} \alpha_{m_0}(\mathbf{p})\overline{\mathbf{z}}_{m_0}^h\right] \tag{5.30}$$

verifies (5.27) for any $\mathbf{p}$, where the set $\{\overline{\mathbf{z}}_{m_0}^h\}_{1\leq m_0\leq m}$ is defined in Section 5.3.2, and $\{\alpha_{m_0}\}_{1\leq m_0\leq m}$ is an arbitrary set of geometry parameter functions (to be optimized). The flux $\overline{\boldsymbol{\tau}}_{\mathbf{p}}^h$ is thus obtained from a direct post-processing of the IGA-PGD solution at hand. Then, using the hybrid-flux technique defined in [TCHM18] on individual fluxes $\overline{\mathbf{q}}_d$ and $\overline{\mathbf{z}}_{m_0}^h$ $(1 \leq m_0 \leq m)$, we eventually obtain a flux $\hat{\overline{\mathbf{q}}}_{\mathbf{p}}^h$ veryfing full equilibration (5.26); it reads:

$$\hat{\overline{\mathbf{q}}}_{\mathbf{p}}^h = J_{\mathbf{p}}^{-1}\mathbb{J}_{\mathbf{p}}\left[\hat{\overline{\mathbf{q}}}_d + \sum_{m_0=1}^{m} \alpha_{m_0}(\mathbf{p})\hat{\overline{\mathbf{z}}}_{m_0}^h\right] \tag{5.31}$$

Functions $\alpha_{m_0}(\mathbf{p})$ are in practice optimized in order to minimize the CRE estimate; this leads to a linear problem as the CRE estimate is quadratic in these functions.

Remark. The admissible flux field $\hat{\overline{\mathbf{q}}}_{\mathbf{p}}^h$ could be mapped to the actual geometry $\Omega(\mathbf{p})$, under the form $\hat{\mathbf{q}}_{\mathbf{p}}^h = \hat{\mathbf{q}}_d + \sum_{m_0=1}^{m} \alpha_{m_0}(\mathbf{p})\hat{\mathbf{z}}_{m_0}^h$. Nevertheless, for computational issues, this is not necessary as it is preferable to compute the CRE estimate in the reference domain $\overline{\Omega}$ (IGA parametric space). It reads:

$$E_{CRE}^2(\hat{u}_{\mathbf{p}}, \hat{\mathbf{q}}_{\mathbf{p}}) = \int_{\Omega(\mathbf{p})} (\hat{\mathbf{q}}_{\mathbf{p}} - \nabla\hat{u}_{\mathbf{p}})\cdot(\hat{\mathbf{q}}_{\mathbf{p}} - \nabla\hat{u}_{\mathbf{p}})\mathrm{d}\mathbf{x} = \int_{\overline{\Omega}} (\hat{\overline{\mathbf{q}}}_{\mathbf{p}} - \mathbb{J}_{\mathbf{p}}^{-T}\nabla_{\boldsymbol{\xi}}\hat{\overline{u}}_{\mathbf{p}})\cdot(\hat{\overline{\mathbf{q}}}_{\mathbf{p}} - \mathbb{J}_{\mathbf{p}}^{-T}\nabla_{\boldsymbol{\xi}}\hat{\overline{u}}_{\mathbf{p}})J_{\mathbf{p}}\mathrm{d}\boldsymbol{\xi} \tag{5.32}$$

This integral can then be effectively computed using a separation of variables (SVD/HOSVD) on $J_{\mathbf{p}}$, $J_{\mathbf{p}}\mathbb{J}_{\mathbf{p}}^{-T}$, and $J_{\mathbf{p}}\mathbb{J}_{\mathbf{p}}^{-1}\mathbb{J}_{\mathbf{p}}^{-T}$.

5.4.2 Adaptive algorithm

The error estimate $E_{CRE}(u_m^h(\cdot,\mathbf{p}), \hat{\mathbf{q}}_{\mathbf{p}})$ previously defined (for any geometry parameter set $\mathbf{p}$) takes into account the various error sources inherent to the IGA-PGD. They are twofold:

- the PGD truncation error due to the restriction of the PGD modal representation to a limited (finite) number m of modes;

- the discretization error due to the use of the approximate IGA method with discretization size h to compute the space functions of these PGD modes.

For adaptive purposes (with use of a greedy approach), we wish to assess the relative contribution of each error source. We thus follow a natural procedure which has been already employed in previous works dealing with error estimation and adaptivity within the CRE framework, in particular [CPAL17]. The idea consists of introducing specific error indicators based on the CRE concept applied to admissible fields in the sense of intermediate reference problems (weaker sense compared to the initial model problem). In practice, we consider a new (intermediate) model problem defined after discretization in space of the initial model problem; this corresponds to the problem (5.4) with solution $u^h_{\mathbf{p}}$.

The global error is then split into $\mathcal{E}^2_{glob}(\mathbf{p}) = \Delta^2_{PGD}(\mathbf{p}) + \Delta^2_{dis}(\mathbf{p})$ where $\Delta_{PGD}(\mathbf{p}) = \|u^h_{\mathbf{p}} - u^h_m(\cdot,\mathbf{p})\|$ quantifies the error coming from the PGD truncation alone ($\Delta_{PGD} \to 0$ when $m \to +\infty$), whereas $\Delta_{dis}(\mathbf{p}) = \|u_{\mathbf{p}} - u^h_{\mathbf{p}}\|$ quantifies the error coming from the IGA space discretization alone ($\Delta_{dis} \to 0$ when $h \to 0$). The first part Δ_{PGD} is assessed considering admissible fields in the discretized sense u^h_m and $\boldsymbol{\tau}^h_{\mathbf{p}}$. We then get:

$$\Delta_{PGD}(\mathbf{p}) \approx E_{CRE}(u^h_m(\cdot,\mathbf{p}), \boldsymbol{\tau}^h_{\mathbf{p}}) = \eta_{PGD}(\mathbf{p}) \tag{5.33}$$

where η_{PGD} defines an error indicator on the PGD truncation error. We then deduce the indicator η_{dis} on the discretization error:

$$\eta^2_{dis}(\mathbf{p}) = E^2_{CRE}(u^h_m(\cdot,\mathbf{p}), \hat{\mathbf{q}}^h_{\mathbf{p}}) - \eta^2_{PGD}(\mathbf{p}) \tag{5.34}$$

The previously defined error estimator and indicators can then be used as stopping criteria and adaptation tools in a greedy algorithm in order to construct a suitable PGD approximation u^h_m that minimizes computational costs while complying with a prescribed accuracy level. In practice, after computing each mode m, the adaptive strategy is conducted as follows:

1. we identify the parameter set $\mathbf{p}_{max} = \text{argmax}_{\mathbf{p}\in\mathcal{P}} E_{CRE}(u^h_m(\cdot,\mathbf{p}), \hat{\mathbf{q}}_{\mathbf{p}})$ (worst case scenario) as well as associated error indicators $\eta_{PGD}(\mathbf{p}_{max})$ and $\eta_{dis}(\mathbf{p}_{max})$;

2. we compare the relative contributions of these indicators to the error estimate:
   - if $\eta_{PGD}(\mathbf{p}_{max}) \geq \eta_{dis}(\mathbf{p}_{max})$, the mode $(m+1)$ is computed keeping the same space discretization as for the mode m;

– otherwise, i.e. if $\eta_{PGD}(\mathbf{p}_{max}) < \eta_{dis}(\mathbf{p}_{max})$, the discretization size h is modified in order to recompute the mode m (and next modes) with better accuracy. For that, optimal mesh adaptation techniques based on local contributions of η_{dis}, as well as on asymptotic convergence rates predicted by *a priori* error estimates, are used to reach a given discretization error threshold. In practice, this error threshold is chosen as $\beta\eta_{PGD}(\mathbf{p}_{max})$ with $\beta \in]0,1[$ a scalar parameter to set. We emphasize that the $(m-1)$ modes previously computed with coarser meshes are kept unchanged.

The adaptive procedure is performed until $\max_{\mathbf{p}\in\mathcal{P}} \left(E_{CRE}(u_m^h(\cdot,\mathbf{p}),\hat{\mathbf{q}}_\mathbf{p})/\|u_m^h(\cdot,\mathbf{p})\|\right) \leq \gamma_{tol}$, where γ_{tol} is a predefined error tolerance.

Remark. The identification of the parameter set $\mathbf{p}_{max}$ (corresponding to the parameter values which maximize the global error estimate) is performed depending on the dimension of the geometry parameter space. For low-dimensional geometry parameter spaces, the screening of the parameter domain $\mathcal{P}$ can be easily performed over a multi-dimensional numerical grid using the explicit dependency of $E_{CRE}(u_m^h(\cdot,\mathbf{p}),\hat{\mathbf{q}}_\mathbf{p})$ on $\mathbf{p}$. Conversely, for high-dimensional geometry parameter spaces, it would require dedicated strategies and specific algorithms such as those used for solving nonlinear optimization problems in large dimension (SQP algorithm for instance).

Remark. After performing mesh adaptation, the intermediate reference problem (with discrete space weak formulation) used to compute error indicators is changed. Consequently, for modes computed before mesh adaptation, part of the discretization error (the one which can be captured with the new finer mesh) is transferred into the indicator η_{PGD} of the PGD truncation error. This procedure is consistent with the definition of discretization error, which should tend to zero when the mesh size used for the current PGD mode goes to zero.

Considering goal-oriented error estimation, the same procedure is used to assess the relative contributions of error sources that contribute to the total local error $\mathcal{E}_Q(\mathbf{p})$ on a given quantity of interest Q (i.e. PGD truncation error and discretization error). Indeed, introducing the approximate IGA value $Q(u_\mathbf{p}^h)$ of the output of interest Q obtained from the approximate IGA solution $u_\mathbf{p}^h$, the local error $\mathcal{E}_Q(\mathbf{p})$ can be split into:

$$\mathcal{E}_Q(\mathbf{p}) = \Delta Q_{PGD}(\mathbf{p}) + \Delta Q_{dis}(\mathbf{p}) \tag{5.35}$$

where $\Delta Q_{PGD}(\mathbf{p}) = Q(u_\mathbf{p}^h) - Q(u_m^h(\cdot,\mathbf{p}))$ is part of the error on Q due to truncation in the PGD decomposition alone, whereas $\Delta Q_{dis}(\mathbf{p}) = Q(u_\mathbf{p}) - Q(u_\mathbf{p}^h)$ is the one due to

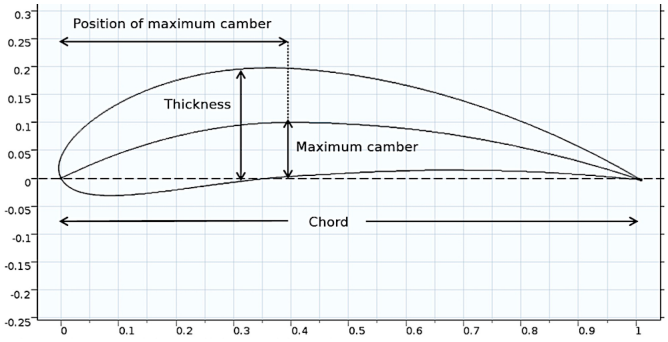

Figure 5.4: Geometry of the NACA profile.

space discretization alone. Both contributions $\Delta Q_{PGD}(\mathbf{p})$ and $\Delta Q_{dis}(\mathbf{p})$ can be easily assessed from the bounding defined in Section **??** and using the admissible fields in the discretized sense u_m^h and $\boldsymbol{\tau}_{\mathbf{p}}^h$. The resulting error indicators $\eta_{PGD}^Q(\mathbf{p})$ and $\eta_{dis}^Q(\mathbf{p})$ are then used to build up a greedy algorithm that aims at controlling the error on a goal-oriented manner. The adaptive strategy is similar to the one developed for the control of global error, with a comparison between η_{PGD}^Q and η_{dis}^Q for a worst-case geometry parameter set $\mathbf{p}_{max}$.

5.5 Numerical results

We illustrate the approach on three numerical experiments exhibiting IGA parametrized geometries: (i) a NACA airfoil 4-digits profile under torsion loading; (ii) an elasticity problem on a plate with a hole with varying radius; (iii) a 3D thermal problem. These examples are typical linear engineering problems with smooth curved domain boundary for which IGA has been proven to be much more effective than FEM.

5.5.1 Computation of the torsion stiffness of a parametrized NACA profile

We consider a parametrized 2D NACA airfoil profile Ω, as studied in [MSH15] in the context of aerospace design. It is described in Figure 5.4. The goal is to evaluate the torsion stiffness of the profile for any geometry configuration.

Geometry parametrization

The shape of NACA airfoil profiles is defined by four digit integers:

- the first digit is the maximum camber m in percentage of the chord;

- the second digit indicates the position p of the maximum camber in tenths of the chord;
- the last two digits describe the maximum thickness t of the airfoil in percentage of the chord.

This generates a family of profiles; for instance choosing $m = 0.02$, $p = 0.4$, and $t = 0.2$ generates the profile NACA 2420.
Introducing the maximum chord c, the mean camber line P_c is defined from the set of coordinates $\{x, y_c\}$ such that:

$$y_c = \begin{cases} m\dfrac{x}{p^2}(2p - \dfrac{x}{c}) & \forall x \in [0, pc] \\ m\dfrac{c-x}{(1-p)^2}(1 + \dfrac{x}{c} - 2p) & \forall x \in [pc, c] \end{cases} \tag{5.36}$$

Next, the thickness distribution P_t above and below the mean camber line is defined by the set of coordinates $\{x, \pm y_t\}$ such that:

$$y_t = 5tc\left[0.2969\sqrt{\frac{x}{c}} - 0.1260\left(\frac{x}{c}\right) - 0.3516\left(\frac{x}{c}\right)^2 + 0.2843\left(\frac{x}{c}\right)^3 - 0.1015\left(\frac{x}{c}\right)^4\right] \tag{5.37}$$

After the above steps, the coordinates of the airfoil upper surface (x_U, y_U) and lower surface (x_L ,y_L) are computed by using the following relations for $x \in [0, c]$:

$$\begin{aligned} x_U &= x - y_t \sin\theta \quad ; \quad y_U = y_c + y_t \cos\theta \quad ; \quad \theta = \arctan(\frac{dy_c}{dx}) \\ x_L &= x + y_t \sin\theta \quad ; \quad y_L = y_c - y_t \cos\theta \end{aligned} \tag{5.38}$$

An illustration of these sets of points for the NACA 2420 airfoil profile is given in Figure 5.5. From this geometry description, two geometry parameters will be considered as design variables in the following: the maximum camber m and the thickness t. Consequently, $\mathbf{p} = \{m, t\}$.

IGA description of the geometry

The airfoil geometry can be parametrized from different representations, such as Ferguson-style cubic splines [SK07] or NURBS [LGTP01, LCLX10]. We use here a representation from B-spline curves. Starting from a knot vector and a set of basis functions, the locations of the associated control points $\mathbf{B}_i$ are chosen through a suitable least square procedure, leading to the solution of a linear system.

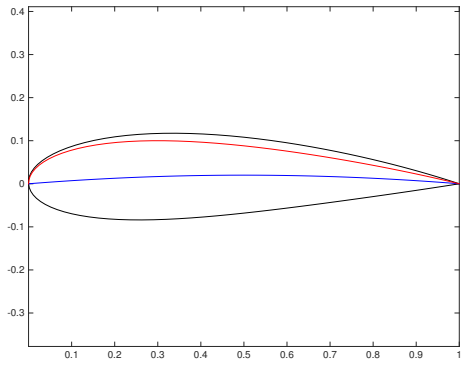

Figure 5.5: Illustration of the mean camber line (in blue), thickness distribution (in red), and upper/lower surfaces (in black) for the NACA 2420 profile.

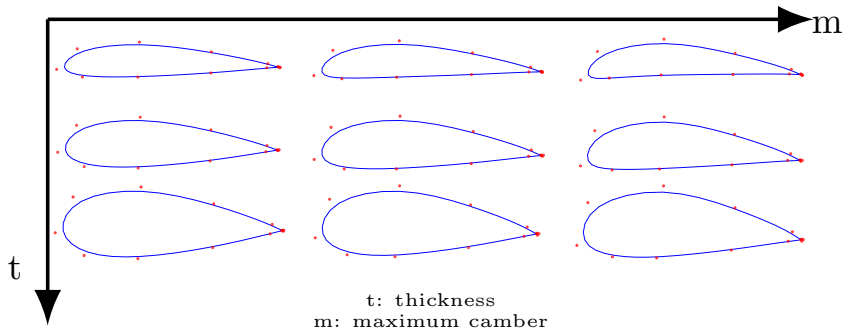

Figure 5.6: Configurations of the parametrized IGA airfoil geometry in the (m, t) system.

Noticing that the values of m and t linearly act on coordinates y_c and y_y, respectively, the parametrization of the B-spline curves with respect to m and t is straightforward. Several configurations of the airfoil geometry, obtained for different values of the pair (m, t) and therefore different control point coordinates, are represented in Figure 5.6. Control meshes for fixed m but varying t are shown in Figure 5.7.

Torsion problem

The problem which is solved on the parametrized physical domain is the classical problem of stress function in torsion. We assume that a torque $\pm C$ is applied at both ends of the wing structure made of an isotropic linear elastic material which shear modulus μ. This loading generates a rotation α per unit length along the wing, and the torsion stiffness

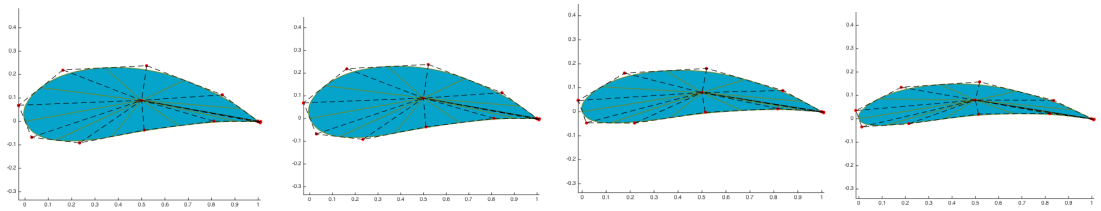

Figure 5.7: Control meshes for several value of the thickness parameter t.

(or modulus) $J = C/\alpha\mu$ is then seen as a quantity of interest for engineering purposes. The stress tensor σ being searched as:

$$\sigma = \alpha\mu \begin{bmatrix} 0 & 0 & u_{,y} \\ 0 & 0 & -u_{,x} \\ u_{,y} & -u_{,x} & 0 \end{bmatrix} \tag{5.39}$$

where u is the torsion function, it is well-known that the problem can be recast as a two-dimensional scalar diffusion problem of the form:

$$\begin{aligned} \Delta u_{\mathbf{p}} &= -2 \quad \text{in } \Omega(\mathbf{p}) \quad \text{(coming from integrability conditions)} \\ u_{\mathbf{p}} &= 0 \quad \text{on } \partial\Omega(\mathbf{p}) \quad \text{(coming from homogeneous Neumann boundary conditions on the profile)} \end{aligned} \tag{5.40}$$

$u_{\mathbf{p}}$ is the torsion function for the parametrized domain $\Omega(\mathbf{p})$. The torsion stiffness can then be calculated from $u_{\mathbf{p}}$ as $J_{\mathbf{p}} = \int_{\Omega(\mathbf{p})} 2u_{\mathbf{p}} \mathrm{d}\Omega$.

PGD solution and adaptive strategy

The problem (5.40) is solved using the previously described IGA-PGD strategy. The domains of variations for the maximum camber and thickness are set to $m \in [0.03, 0.08]$ and $t \in [0.15, 0.35]$, respectively. The first three PGD modes in space (for fixed mesh) and in geometry parameters are displayed in Figure 5.8 and Figure 5.9, respectively. The PGD solution evaluated for $m = 0.07$ and $t \in \{0.15, 0.25, 0.35\}$ is also shown in Figure 5.10. We now investigate *a posteriori* error estimation and adaptivity from the CRE concept. After computing each PGD mode, an equilibrated flux field $\hat{\mathbf{q}}_{\mathbf{p}}$ is recovered and the global error estimate $E_{CRE}(u_m^h(\cdot, \mathbf{p}), \hat{\mathbf{q}}_{\mathbf{p}})$ is computed (see Section 5.4.1). The evolution of this estimate in the geometry parameter space, and after computing the first PGD mode, is shown in Figure 5.11. It shows that maximal errors are made when t is large and m is small, or the reverse. Then, computed indicators η_{PGD} and η_{dis}, an adaptive strategy (with greedy algorithm) can be conducted as described in Section 5.4.2. In Figure 5.12, we show the evolutions of the error estimate and indicators along the

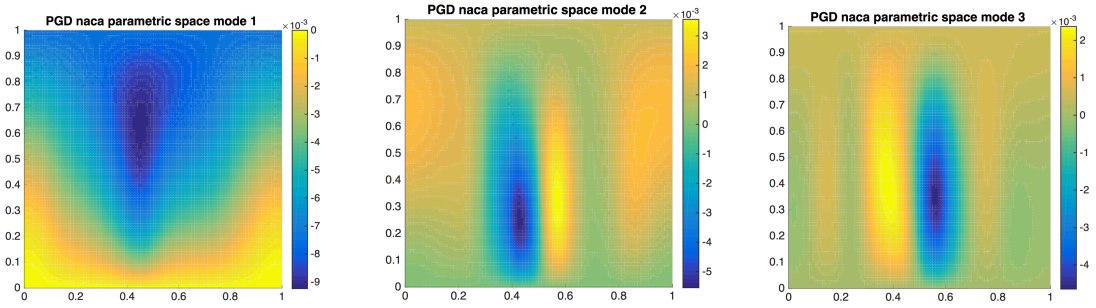

Figure 5.8: First three PGD modes in space (from left to right) in the IGA parametric space $\overline{\Omega}$.

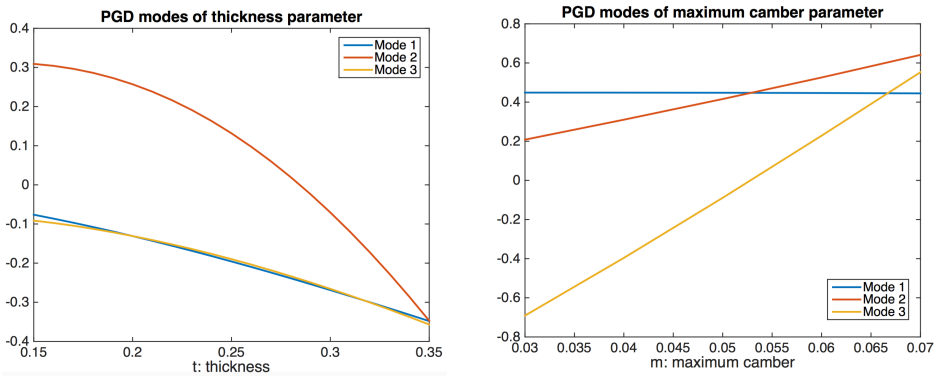

Figure 5.9: First three PGD modes in parameter t (left) and m (right).

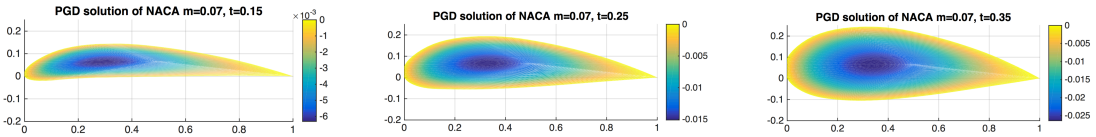

Figure 5.10: Approximate 3-mode PGD solution for various (m, t) couples.

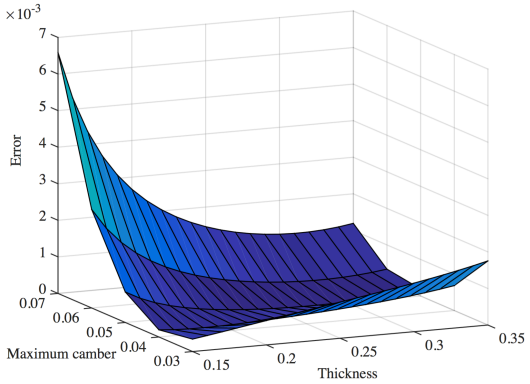

Figure 5.11: Evolution of the estimate $E_{CRE}(u_1^h(\cdot,\mathbf{p}),\hat{\mathbf{q}}_\mathbf{p})$ with respect to $\mathbf{p}=\{t,m\}$.

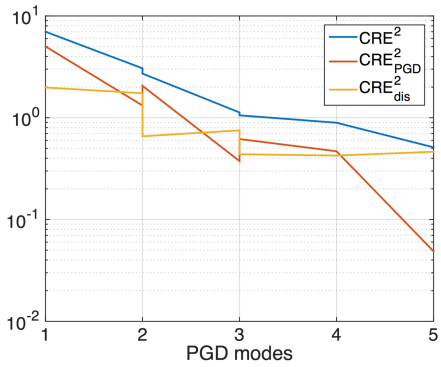

Figure 5.12: Evolution of the global error estimate (in blue), and error indicators on PGD error (in red) and discretization error (in orange) along the adaptive process.

adaptive process. We observe that the mesh is successively refined when computing modes 2 and 3. We show in Figure 5.13 the refined mesh used to compute the mode 3 compared to the initial coarse mesh used to compute the mode 1.

Eventually, considering $Q(u_\mathbf{p})=J_\mathbf{p}$ as the quantity of interest, a similar adaptive procedure is used for goal-oriented error estimation. For this purpose, the adjoint problem associated with $J_\mathbf{p}$ is solved in order to compute the error estimate and indicators ρ_{PGD} and ρ_{dis}. After performing the adaptive algorithm up to $m=5$, the predicted value $Q(u_m^h(\cdot,\mathbf{p}))$ of the quantity of interest as well as upper and lower bounds on the error $\mathcal{E}_Q(\mathbf{p})$ are reported in Figure 5.14 over the definition space of $\mathbf{p}$. They indicate that a very accurate PGD approximation of $J_\mathbf{p}$ is obtained for any value of $\mathbf{p}$, with certification of the prediction within a small error interval (relative error lower than 1%).

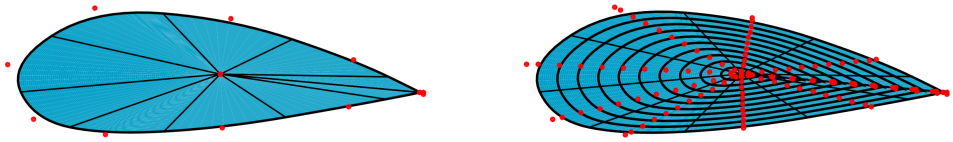

Figure 5.13: Initial coarse mesh (left), and refined mesh obtained for the computation of mode 3 (right) in the physical space.

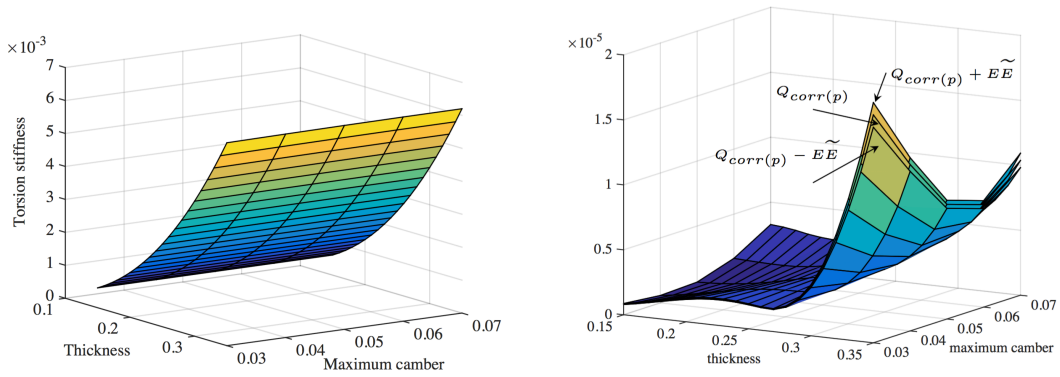

Figure 5.14: PGD approximation $Q(u_m^h(\cdot, \mathbf{p}))$ (left) and error bounds $Q^-(\mathbf{p})$ and $Q^+(\mathbf{p})$ (right) on the quantity of interest $J_\mathbf{p}$ for $m = 5$.

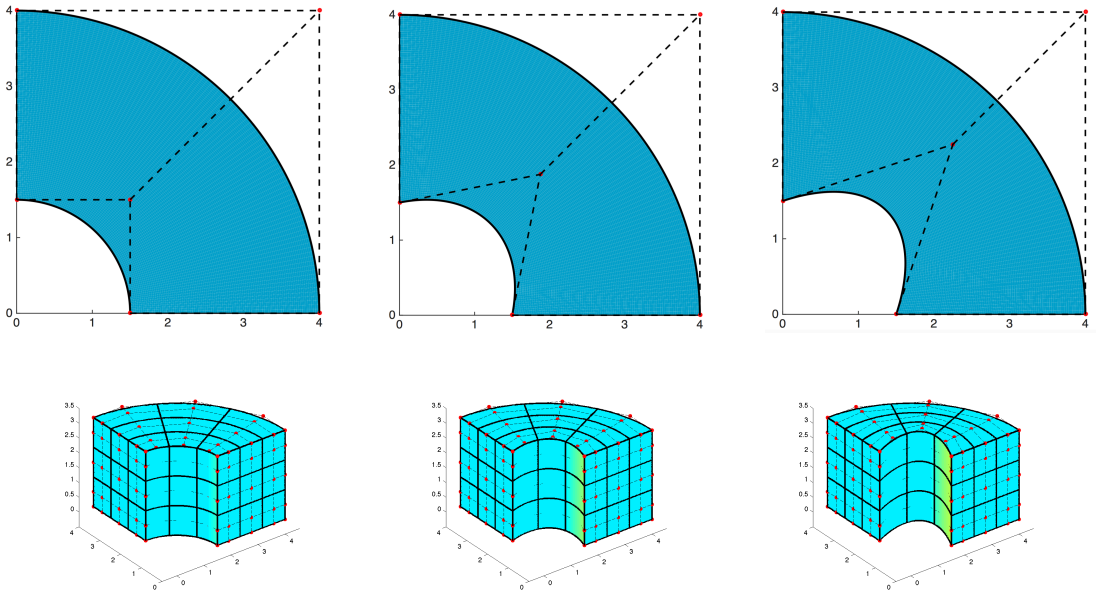

Figure 5.15: Several geometry configurations of the 3D structure, with $\alpha = 1, 1.25, 1.5$ (from left to right).

5.5.2 Parametrized 3D geometry

Eventually, we consider a 3D heat conduction problem on the quarter of a hollow cylinder. The structure is submitted to a homogeneous unit heat source, and homogeneous Dirichlet boundary conditions are applied. In the undeformed geometrical configuration, the cylinder has external radius $R_{ext} = 4$, internal radius $R_{int} = 1.5$, and height $H = 3$. The geometry, represented by NURBS functions, is here parametrized by the radial position $r = 1.5\alpha$ with $\alpha \in [1, 1.5]$ of the middle control point (see Figure 5.15 in which several configurations are shown). The resulting 3D parametrized problem is solved using PGD. The first three PGD modes in space and in the geometry parameter α are displayed in Figure 5.16 and Figure 5.17, respectively. The PGD solution evaluated for $\alpha \in \{1, 1.25, 1.5\}$ is also shown in Figure 5.18.

Here again, *a posteriori* error estimation is performed. After computing the first PGD mode, the evolution of the global error estimate $E_{CRE}(u_m^h(\cdot, \mathbf{p}), \hat{\mathbf{q}}_\mathbf{p})$ with respect to α is reported in Figure 5.19. It shows that the highest error level is made for $\alpha = 1$. The distribution map of the indicator on discretization error η_{dis} is also represented in Figure 5.19. Eventually, we represent in Figure 5.20 the evolution of the global CRE error estimate with respect to the number of PGD modes (for fixed mesh). This indicates that mesh refinement is necessary after computing 2 or 3 PGD modes, which is foreseen

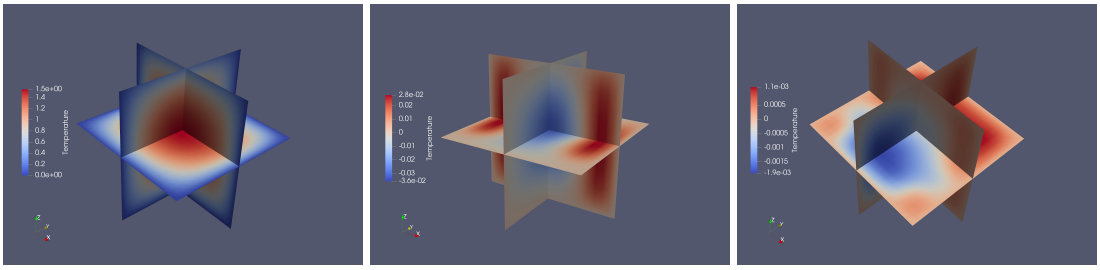

Figure 5.16: First three PGD modes in space (from left to right) in the IGA parametric space $\overline{\Omega}$.

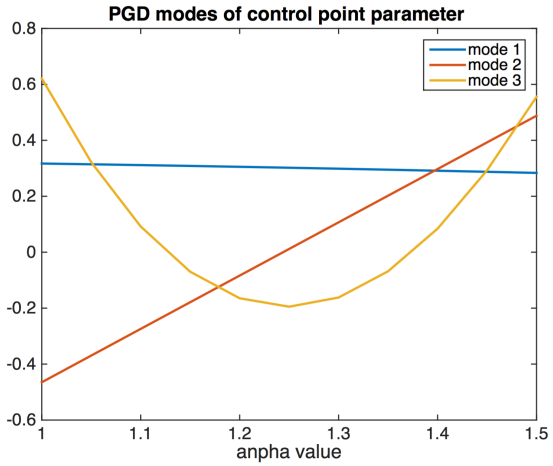

Figure 5.17: First three PGD modes in the geometry parameter α.

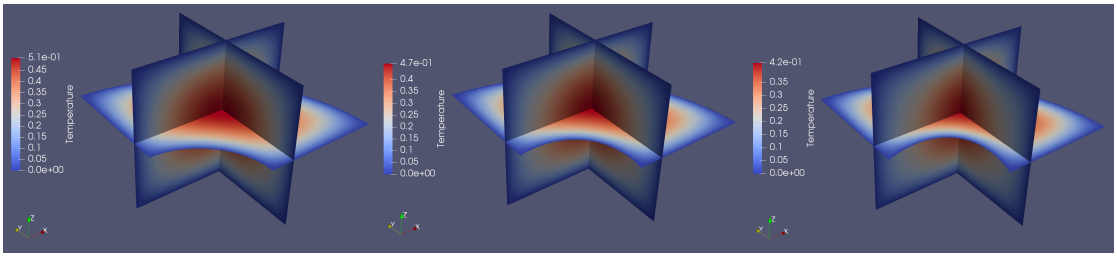

Figure 5.18: Approximate 3-mode PGD solution for various values of α (1, 1.25, and 1.5 from left to right).

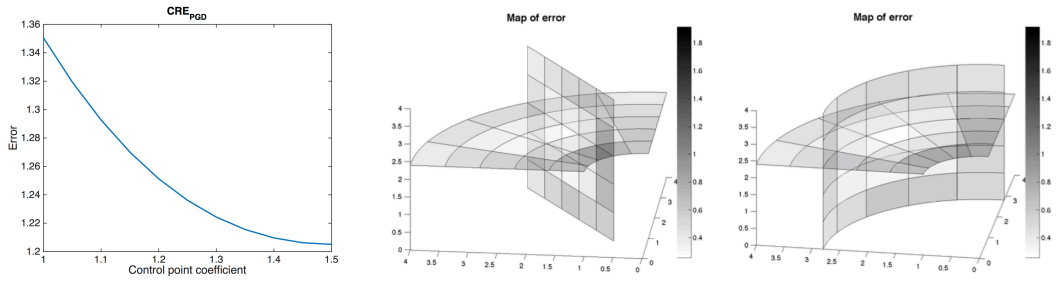

Figure 5.19: Evolution of the estimate $E_{CRE}(u_1^h(\cdot, \mathbf{p}), \hat{\mathbf{q}}_\mathbf{p})$ with respect to α (left), and distribution of the discretization error (right).

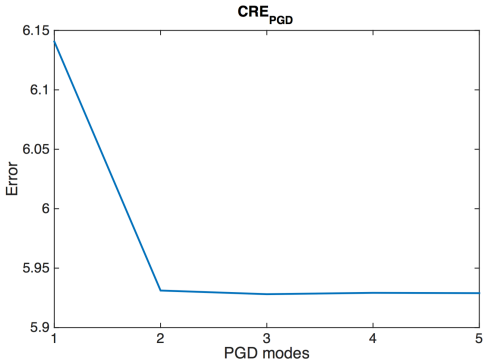

Figure 5.20: Evolution of the CRE error estimate (for fixed mesh) with respect to the number of PGD modes.

by the proposed adaptive process.

5.6 Conclusion

We proposed a general framework for robust and effective shape optimization in structural engineering activities. It is based on three complementary ingredients: isogeometric analysis, PGD model reduction, and CRE error estimation. The first one enables a simple and flexible parametrization of the geometry, and leads to the definition of a parametrized problem which is set in a fixed physical domain with regular dependency of the solution with respect to geometry parameters. The second ingredient, with offline/online steps, aims at computing the manifold of solutions efficiently and obtaining a virtual chart of parametrized solutions that can be evaluated in real-time. Eventually, the last ingredient introduces certification in the quality of the approximate solutions and associated quantities of interest; it drives an adaptive process that defines a trade-

off between solution accuracy and computing cost. The numerical results showed the performance of the approach and its interest for optimization purposes with complex geometries.

Chapter 6

Extension to damage phenomena inside structures with parametrized geometry

Contents

6.1 Introduction 121
6.2 CRE functional for nonlinear material behaviors 122
6.3 CRE for damage problems 125
6.3.1 Example : damage problem on a plate with circular hole . . . 127
6.4 Parametrized reference model with damage behavior 128
6.4.1 The model problem 128
6.5 Procedure for reference model with damage behaviour . . . 130
6.5.1 Step 1: non-damage stage 130
6.5.2 Step 2: Newton method 130
6.5.3 Example : nonlinear problem on a plate with circular hole using PGD 131

6.1 Introduction

We think the coupling between IGA, PGD, and CRE tools is a valuable approach, making scientific advances in the field, and which paves the way for further studies. Here, we thus propose to couple PGD with IGA for nonlinear damage problems with parametrized

geometry. In this approach, PGD extra-coordinates are then related to the coordinates of control points at the coarsest mesh level.

First, we study damage problem with specific geometry using IGA. The problem is solved using a classical incremental procedure. The same damage problem with parametrized geometry is solved by PGD. To build-up the PGD approximated solution, we considered a Newton linearization approach [PCA10, AND+10]. With this approach, we first linearize the governing equation and then apply the PGD at each Newton iteration. The increment δu is the solution of the linearized problem.
We notice that an alternative approach to apply PGD for nonlinear problems is the large time increment (LATIN) solver [Lad99]] in which his so called 'radial approximations' use a space-time separated representation of the form. This method can be thought of as a space-time PGD. This method allows one to employ non-incremental time integration which can be a huge computational saving. The synergy between the LATIN solver and the PGD was highlighted in [LP10]. In the following, we rather prefer the incremental approach that enables to apply in a more straightforward manner the tools developed in the previous chapters.

6.2 CRE functional for nonlinear material behaviors

From its original definition for linear thermal or elasticity problems [LL83], several extended formulations of the CRE concept have been proposed over the years in the case of nonlinear behaviors [LP05]. We focus here on the one described in [LMD99, Lad01], which applies to the large class of material behaviors with standard formulation (such as (visco-)plasticity), and which is suited to material behaviors with softening.

The starting point is the formulation of the nonlinear material behavior in terms of state equations and evolution laws [GNS83, HN75]. Using the thermodynamical framework, we introduce the Helmholtz free energy potential ψ:

$$\psi := \psi(T, \boldsymbol{\varepsilon}, \boldsymbol{\varepsilon}_p, \mathbf{V}) = \psi(T, \boldsymbol{\varepsilon}_e, \mathbf{V}) \tag{6.1}$$

that depends on state variables, i.e. observable variables (temperature T and strain tensor $\boldsymbol{\varepsilon}$) and internal variables: (i) the inelastic part $\boldsymbol{\varepsilon}_p$ of the strain tensor, such that $\boldsymbol{\varepsilon} = \boldsymbol{\varepsilon}_e + \boldsymbol{\varepsilon}_p$; (ii) additional internal variables V_i gathered in a vector $\mathbf{V}$. Then, the two first principles of thermodynamics lead to the Clausius-Duhem inequality (6.2):

$$\left(\boldsymbol{\sigma} - \rho\frac{\partial\psi}{\partial\boldsymbol{\varepsilon}_e}\right) : \dot{\boldsymbol{\varepsilon}}_e - \rho\left(s + \frac{\partial\psi}{\partial T}\right)\dot{T} - \sum_i \rho\frac{\partial\psi}{\partial V_i} \circ \dot{V}_i + \boldsymbol{\sigma} : \dot{\boldsymbol{\varepsilon}}_p - \frac{\mathbf{q}\cdot\nabla T}{T} \geq 0 \tag{6.2}$$

where ρ is the density, s is the entropy, and $\mathbf{q}$ is the thermal flux. Consequently, considering particular non-dissipative transformations leads to the relations:

$$\boldsymbol{\sigma} = \partial_{\boldsymbol{\varepsilon}_e} \rho\psi \quad ; \quad s = -\partial_T \psi \tag{6.3}$$

Similarly, we can introduce thermodynamical loads Y_i (gathered in a vector $\mathbf{Y}$) associated with internal variables V_i:

$$Y_i = \partial_{V_i} \psi \tag{6.4}$$

so that (6.2) can be recast in the following condensed format:

$$\boldsymbol{\sigma} : \dot{\boldsymbol{\varepsilon}}_p - \mathbf{Y} \cdot \dot{\mathbf{V}} - \frac{\mathbf{q} \cdot \nabla T}{T} \geq 0 \tag{6.5}$$

We mention that (6.3) and (6.4) constitute the state equations of the material behavior.

Remark. By duality, we can define the Gibbs free energy potential, denoted $\psi^\star$, as the Legendre-Fenchel transform of the Helmholtz free energy (6.1):

$$\psi^\star\left(T, \boldsymbol{\sigma}, \mathbf{Y}\right) = \sup_{\boldsymbol{\varepsilon}_e, \mathbf{V}} \left(\boldsymbol{\sigma} : \boldsymbol{\varepsilon}_e + \mathbf{Y} \cdot \mathbf{V} - \psi\left(T, \boldsymbol{\varepsilon}_e, \mathbf{V}\right)\right) \tag{6.6}$$

so that $\psi\left(T, \boldsymbol{\varepsilon}_e, \mathbf{V}\right) + \psi^\star\left(T, \boldsymbol{\sigma}, \mathbf{Y}\right) - \boldsymbol{\sigma} : \boldsymbol{\varepsilon}_e - \mathbf{Y} \cdot \mathbf{V} \geq 0$.

Then, it can be shown using convex analysis [Lad01] that state equations can be equivalently recast as:

$$\psi\left(T, \boldsymbol{\varepsilon}_e, \mathbf{V}\right) + \psi^\star\left(T, \boldsymbol{\sigma}, \mathbf{Y}\right) - \left\langle \left(\boldsymbol{\sigma}, \mathbf{Y}\right), \left(\boldsymbol{\varepsilon}_e, \mathbf{V}\right) \right\rangle = 0 \tag{6.7}$$

where we introduced the notation $\left\langle \left(\boldsymbol{\sigma}, \mathbf{Y}\right), \left(\boldsymbol{\varepsilon}_e, \mathbf{V}\right) \right\rangle = \boldsymbol{\sigma} : \boldsymbol{\varepsilon}_e + \mathbf{Y} \cdot \mathbf{V}$.

The inequality (6.5) reflects the dissipative evolution phenomena associated with the nonlinear material behavior. In particular, it imposes a consistency condition on the pair of variables $((\boldsymbol{\varepsilon}_p, \mathbf{V}), (\boldsymbol{\sigma}, \mathbf{Y}))$ in order to ensure that the intrinsic part $\boldsymbol{\sigma} : \dot{\boldsymbol{\varepsilon}}_p - \mathbf{Y} \cdot \dot{\mathbf{V}}$ of the dissipation remains positive. To satisfy the previous condition, it is usual and convenient to introduce a dissipation pseudo-potential, denoted $\varphi(\dot{\boldsymbol{\varepsilon}}_p, -\dot{\mathbf{V}})$, as well as its dual potential (defined using the Legendre-Fenchel transform):

$$\varphi^\star(\boldsymbol{\sigma}, \mathbf{Y}) = \sup_{\dot{\boldsymbol{\varepsilon}}_p, \dot{\mathbf{V}}} \left(\left\langle \left(\boldsymbol{\sigma}, \mathbf{Y}\right), \left(\dot{\boldsymbol{\varepsilon}}_p, -\dot{\mathbf{V}}\right) \right\rangle - \varphi\left(\dot{\boldsymbol{\varepsilon}}_p, -\dot{\mathbf{V}}\right) \right) \tag{6.8}$$

Then, evolution laws are defined from the gradients of potential φ (or $\varphi^\star$), involving an operator $\mathcal{B}$:

$$\begin{bmatrix} -\dot{\mathbf{V}} \\ \dot{\boldsymbol{\varepsilon}}_p \end{bmatrix} = \mathcal{B}\left(\begin{bmatrix} \mathbf{Y} \\ \boldsymbol{\sigma} \end{bmatrix} \right) = \partial_{(\boldsymbol{\sigma}, \mathbf{Y})} \varphi^\star(\boldsymbol{\sigma}, \mathbf{Y}) \tag{6.9}$$

so that the Clausius-Duhem inequality (6.5), which comes down to positive definite properties of the operator $\mathcal{B}$:

$$\begin{bmatrix} \mathbf{Y} \\ \boldsymbol{\sigma} \end{bmatrix} \cdot \mathcal{B}\left(\begin{bmatrix} \mathbf{Y} \\ \boldsymbol{\sigma} \end{bmatrix} \right) \geq 0 \tag{6.10}$$

is naturally satisfied when dissipation pseudo-potentials are chosen convex, with $\varphi(\mathbf{0},\mathbf{0}) = \varphi^*(\mathbf{0},\mathbf{0}) = 0$.

From the previous thermodynamical formulation of nonlinear behaviors, a general CRE measure was derived in [LMD99] from residuals on: (i) the state equations; (ii) the evolution laws. These residuals are defined using the Legendre-Fenchel inequality applied to the corresponding thermodynamical potentials. They read:

- residual on the state equations:

$$\eta_\psi(\boldsymbol{\varepsilon}_e, \mathbf{V}, \boldsymbol{\sigma}, \mathbf{Y}) = \psi(\boldsymbol{\varepsilon}_e, \mathbf{V}) + \psi^\star(\boldsymbol{\sigma}, \mathbf{Y}) - \langle (\boldsymbol{\sigma}, \mathbf{Y}) \, , \, (\boldsymbol{\varepsilon}_e, \mathbf{V}) \rangle \geq 0 \tag{6.11}$$

- residual on the evolution laws:

$$\eta_\varphi(\dot{\boldsymbol{\varepsilon}}_p, -\dot{\mathbf{V}}, \boldsymbol{\sigma}, \mathbf{Y}) = \varphi(\dot{\boldsymbol{\varepsilon}}_p, -\dot{\mathbf{V}}) + \varphi^\star(\boldsymbol{\sigma}, \mathbf{Y}) - \left\langle (\boldsymbol{\sigma}, \mathbf{Y}) \, , \, (\dot{\boldsymbol{\varepsilon}}_p, -\dot{\mathbf{V}}) \right\rangle \geq 0 \tag{6.12}$$

We notice again that convex analysis yields $\eta_\psi = 0$ (resp. $\eta_\varphi = 0$) when state equations (resp. evolution laws) are satisfied.

Remark. For nonlinear problems, when the material behavior is described using internal variables, the state laws may be seen as "internal" equilibrium relations and thus included in the definition of admissibility, or seen as constitutive law like the evolution laws and thus included in the CRE residual The first choice was investigated in [LM98]. This choice leads to the terminology of dissipation error since the error is measured through the residuals of the sole evolution laws, the state laws being a priori satisfied. An alternative is to consider the state laws as part of the CRE functional; in this case the error estimate involves the residuals associated to both the state and evolution laws. We shall see that this second choice allows to fit elasticity, plasticity, viscoplasticity with or without softening in the same framework. The dissipation error is recovered as a particular case by enforcing strongly the state laws.

For the sake of simplicity, we denote $\boldsymbol{\Sigma} = (\boldsymbol{\varepsilon}_e, \boldsymbol{\varepsilon}_p, \mathbf{V}, \boldsymbol{\sigma}, \mathbf{Y})$ the whole set of variables. From the two residuals (6.11,6.12), the local in space and time CRE measure e_{CRE} is defined as: •

$$e^2_{CRE}(\boldsymbol{\Sigma}) = \eta_\psi(\boldsymbol{\Sigma}) + \int_0^t \eta_\varphi(\boldsymbol{\Sigma}) \, \mathrm{d}t \quad \forall \mathbf{x} \in \Omega, \forall t \in I_t \tag{6.13}$$

and a global measure can be obtained by integration over the space-time domain.

6.3 CRE for damage problems

The considered damage law involves a delay effect in order to circumvent numerical issues due to localization phenomena and mesh dependency. Such a model, described in [AD97, LMD99, Lad01], has been extensively used for composite materials. Following the general framework given in Section 6.2, the material is split in two parts:

- state equations:

$$\begin{aligned} \sigma &= (1-d)\mathbf{K}_0\epsilon = \partial_\epsilon \psi^* \quad (0 \leq d \leq 1) \\ Y &= \frac{1}{2}\mathbf{K}_0\epsilon : \epsilon = \partial_d \psi \\ \beta &= (Y_c - Y_0)\alpha^2 = \omega(\alpha) = \partial_\alpha \psi \end{aligned} \tag{6.14}$$

  where d is the damage parameter, Y is the energy release rate, Y_0 is a threshold for damage appearing, Y_c is the critical threshold from which the material breaks, α is an additional internal variable, and β is the associated dual internal variable. The behavior law $\beta = \omega(\alpha)$, with $\omega(0) = 0$ and $\omega'(x) \geq 0$, takes an hardening effect into account. In this framework, the dissipation reads $Y\dot{d} - \beta\dot{\alpha}$, and potentials ψ and ψ^* are defined as:

$$\begin{aligned} \psi(\sigma, d, \alpha) &= \frac{1}{2}\frac{\mathbf{K}_0^{-1}\sigma : \sigma}{(1-d)} + \Psi_{d\leq 1} + Y_c\frac{|\alpha|^3}{3} \\ \psi^*(\epsilon, Y, \beta) &= Y + \Psi_{C_d}(\epsilon, Y) + \frac{2}{3}Y_c\left(\frac{|\beta|}{Y_c}\right)^{3/2} \end{aligned} \tag{6.15}$$

  where Ψ is the indicatrix function.

- evolution laws:

$$\begin{aligned} \dot{d} &= \frac{k}{a}\left(1 - exp(-a\langle\frac{Y - Y_0 - \beta}{Y_c - Y_0}\rangle_+)\right) = -h'(\langle Y - Y_0 - \beta\rangle_+) = \partial_Y \varphi^* \\ -\dot{\alpha} &= -\dot{d} = \partial_\beta \varphi^* \\ d &= \alpha = 0 \quad \text{at } t = 0 \end{aligned} \tag{6.16}$$

  with $h'(0) = 0$ and $h'(x) \geq 0$. The dissipation potential φ^* are defined as:

$$\begin{aligned} \varphi(\dot{d}, -\dot{\alpha}) &= \dot{d}\frac{(a-1)Y_0 + Y_c}{a} + (\frac{k}{a} - \dot{d})\ln(1 - \frac{a}{k}\dot{d}) \\ \varphi^*(Y, \beta) &= \frac{k}{a}\left[\langle Y - Y_0 - \beta\rangle_+ + \frac{Y_c - Y_0}{a}(exp(-\frac{a}{Y_c - Y_0}\langle Y - Y_0 - \beta\rangle_+) - 1)\right] \end{aligned} \tag{6.17}$$

As detailed in Section 6.2, the residuals on state equations and evolution laws read, respectively:

$$\begin{aligned} \eta_\psi(\epsilon, Y, \beta; \sigma, d, \alpha) &= \psi(\sigma, d, \alpha) + \psi^*(\epsilon, Y, \beta) - \sigma : \cdot\epsilon - Yd - \beta\alpha \geq 0 \\ \eta_\varphi(\dot{d}, -\dot{\alpha}; Y, \beta) &= \varphi(\dot{d}, -\dot{\alpha}) + \varphi^*(Y, \beta) - Y\dot{d} + \beta\dot{\alpha} \geq 0 \end{aligned} \tag{6.18}$$

Remark. We notice that alternative methods exist to introduce a characteristic length and avoid the previously described numerical issues. Let us quote nonlocal models (with average of Y), models with gradients (of ϵ and d), or viscous effects models (viscosity in the evolution law of d).

Remark. Gathering σ with variable d enables to obtain a convex potential $\psi(\sigma, d, \alpha)$. This would not be the case gathering ϵ with d as $\psi(\epsilon, d) = \frac{1}{2}\epsilon(1-d)\mathbf{K}_0\epsilon$ is not a convex function.

After computing an admissible set $\hat{\mathbf{\Sigma}}_h = (\hat{\epsilon}_h, \hat{Y}_h, \hat{\beta}_h, \hat{\sigma}_h, \hat{d}_h, \hat{\alpha}_h)$ from the approximate IGA solution, the CRE error estimate is defined as:

$$E^2_{CRE}(\hat{\mathbf{\Sigma}}_h) = \int_\Omega \left[\eta_\psi \left(\hat{\mathbf{\Sigma}}_h \right) + \int_0^T \eta_\varphi \left(\hat{\mathbf{\Sigma}}_h \right) \mathrm{d}t \right] \mathrm{d}\mathbf{x} \tag{6.19}$$

In practice, the procedure to recover the admissible set $\hat{\mathbf{\Sigma}}_h$ follows that described in [LMD99]; it uses the incremental solution of the problem, as well as the general procedure given in Section 5.4.1 for the recovery of an equilibrated stress field $\hat{\sigma}_h$. At each increment point k:

- we choose $\hat{\mathbf{u}}_h^{(k)} = \mathbf{u}_h^{(k)}$, i.e. $\hat{\epsilon}_h^{(k)} = \epsilon_h^{(k)}$;
- we construct $\hat{\sigma}_h^{(k)}$ from a post-processing of $\sigma_h^{(k)}$ using the procedure described in Section 5.4.1.

A linear interpolation between increment points is then performed to define fields $\hat{\epsilon}_h$ and $\hat{\sigma}_h$ over the whole time-space domain. Eventually, admissible internal variables $\hat{Y}_h$, $\hat{\beta}_h$, $\hat{d}_h$, and $\hat{\alpha}_h$ are chosen in order to minimize the CRE estimate. This constrained minimization procedure is cheap as it is performed locally at each integration point, and incrementally in time considering piecewise linear evolutions.

6.3.1 Example : damage problem on a plate with circular hole

As an example, we consider a nonlinear damage problem (elasticity with isotropic softening) on a plate with circular hole under in-plane tension, as described in [VGJS11]. The geometry and boundary conditions are given in Figure 6.1. We assume a plane stress behavior. Specific boundary conditions are prescribed.

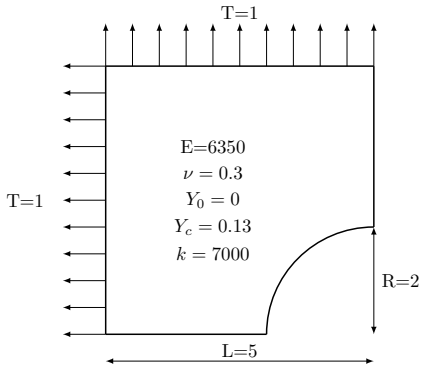

Figure 6.1: The considered problem.

The problem is solved using a classical incremental procedure. The approximate damage fields at two different increments are represented in Fig. 6.2.

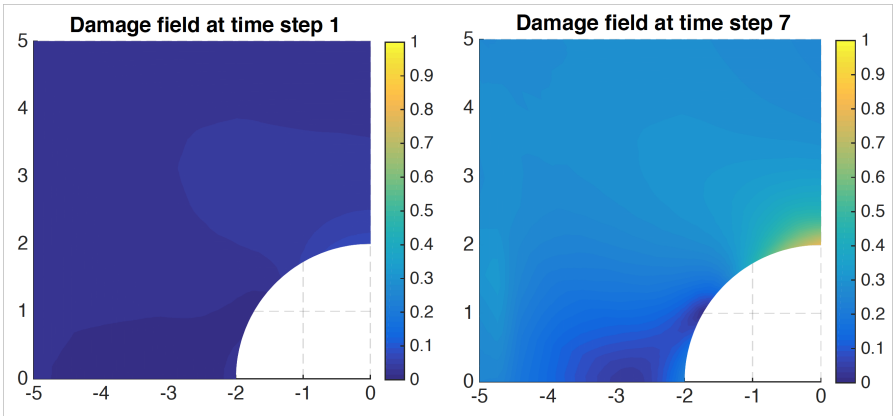

Figure 6.2: Approximate damage fields at increasing increments (from left to right).

The obtained admissible stress field (at step 7) is represented in Figure 6.3, whereas the spatial map of the CRE estimate (in terms of error density, as local contributions to the CRE estimate are normalized by the element size) as well as its evolution with step increments are given in Figure 6.4.

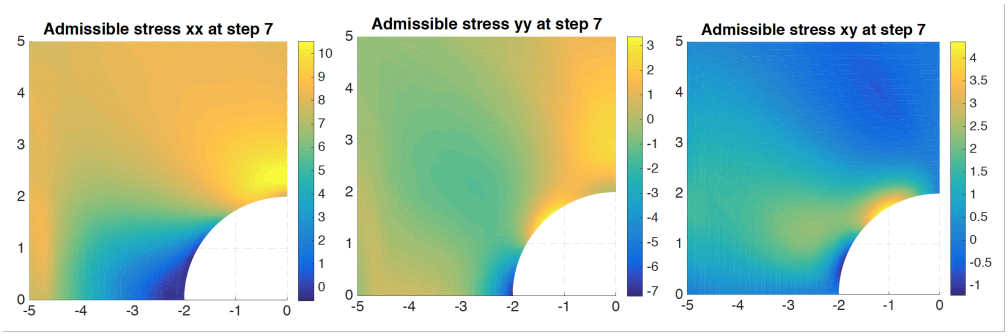

Figure 6.3: Admissible stress field: σ_{xx} (left), σ_{yy} (center), and σ_{xy} (right).

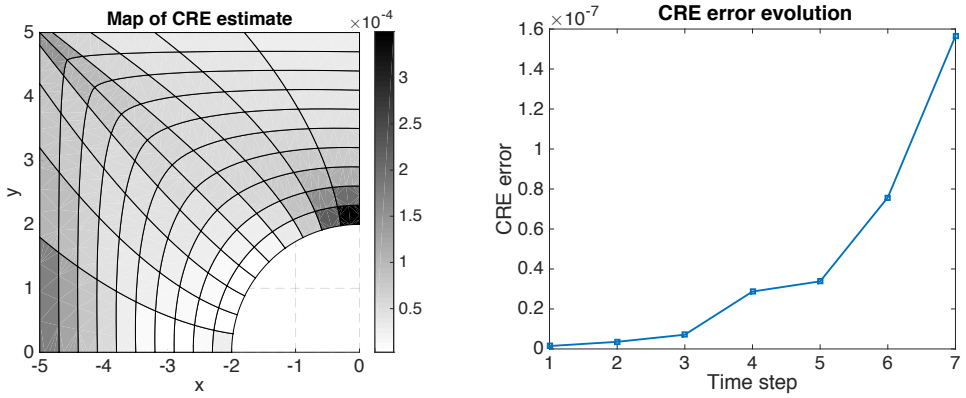

Figure 6.4: Map of the CRE estimate (left) and evolution with step increments (right).

Here again, the results obtained from the CRE error estimate are consistent, with larger error in the vicinity of the damage zone and boundary conditions, and are useful indication for quantitative error assessment and mesh refinement.

6.4 Parametrized reference model with damage behavior

6.4.1 The model problem

We consider a family of physical open bounded domains $\Omega(\mathbf{p}) \in \mathbb{R}^d$ (d=2 or 3), with boundary $\partial\Omega(\mathbf{p})$, whose geometry is parametrized by a finite-dimensional vector $\mathbf{p} \in \mathcal{P}$ of parameters which drive the variations of the geometry. Over this parametrized domain, and under quasi-static and isothermal evolutions, we define a mechanical problem with prescribed time-dependent loading. We assume that homogeneous Dirichlet boundary conditions are prescribed on a non-zero part $\partial_u\Omega(\mathbf{p}) \subset \partial\Omega(\mathbf{p})$, while Neumann boundary

conditions with given stress vector $\mathbf{F}_d \in [L^2(\partial_q\Omega)]^d$ are prescribed on the complementary part $\partial_F\Omega(\mathbf{p}) \subset \partial\Omega(\mathbf{p})$. A given source term $\mathbf{f}_d \in L^2(\Omega)$ may also be active in $\Omega(\mathbf{p})$. The material behavior is chosen as elastic with softening. The problem thus consists in finding, for any value of the parameter set $\mathbf{p}$, the displacement field $\mathbf{u_p}$ and stress field $\sigma_\mathbf{p}$ verifying:

1. the kinematic constraints
$$\mathbf{u} = \mathbf{0} \quad \text{on } \partial_u\Omega(\mathbf{p}) \tag{6.20}$$

2. the balance equations
$$\begin{cases} \operatorname{div}\sigma_\mathbf{p} + \mathbf{f}_d = \mathbf{0} & \text{in } \Omega(\mathbf{p}) \\ \sigma_\mathbf{p}\cdot\mathbf{n} = \mathbf{F}_d & \text{on } \partial_F\Omega(\mathbf{p}) \end{cases} \quad \text{or} \quad \int_{\Omega(\mathbf{p})} \sigma_\mathbf{p} : \epsilon(\mathbf{v}) = \int_{\Omega(\mathbf{p})} \mathbf{f}_d\cdot\mathbf{v} + \int_{\partial_F\Omega(\mathbf{p})} \mathbf{F}_d\cdot\mathbf{v} \quad \forall\mathbf{v} \tag{6.21}$$

3. the (nonlinear) constitutive relation:
$$\sigma_{\mathbf{p}|t} = \boldsymbol{\mathcal{A}}(\dot{\epsilon}_{|\tau}, \tau \le t) \tag{6.22}$$

where $\epsilon = \boldsymbol{\nabla}^S(\mathbf{u})$ denotes the linearized strain tensor. The problem is complemented with initial conditions which are supposed to be zero.

Introducing the functional space $\mathcal{U}_\mathbf{p} = [H_0^1(\Omega(\mathbf{p}))]^d$, the weak formulation of the problem reads:
$$\text{Find } \mathbf{u_p} \in \mathcal{U}_\mathbf{p} \text{ such that } a_\mathbf{p}(\mathbf{u_p};\mathbf{v}) = \ell_\mathbf{p}(\mathbf{v}) \quad \forall\mathbf{v} \in \mathcal{U}_\mathbf{p} \tag{6.23}$$
where the parametrized form $a_\mathbf{p}(\mathbf{u_p};\mathbf{v})$ is linear in $\mathbf{v}$ but nonlinear in $\mathbf{u_p}$. In practice, this nonlinear problem may be solved incrementaly and using an iterative Newton method; for a given loading increment and at iteration k, the solution if written as $\mathbf{u}_\mathbf{p}^{(k+1)} = \mathbf{u}_\mathbf{p}^{(k)} + \delta\mathbf{u}_\mathbf{p}^{(k)}$ where the correction term $\delta\mathbf{u}_\mathbf{p}^{(k)}$ is the solution to the linear problem:
$$R'_\mathbf{p}(\mathbf{u}_\mathbf{p}^{(k)}; \delta\mathbf{u}_\mathbf{p}^{(k)}, \mathbf{v}) = -R_\mathbf{p}(\mathbf{u}_\mathbf{p}^{(k)}; \mathbf{v}) \quad \forall\mathbf{v} \in \mathcal{U}_\mathbf{p} \tag{6.24}$$
where $R_\mathbf{p}(\mathbf{u};\mathbf{v}) = \ell_\mathbf{p}(\mathbf{v}) - a_\mathbf{p}(\mathbf{u};\mathbf{v})$ and $R'_\mathbf{p}$ is the Gateaux derivative of $R_\mathbf{p}$.

6.5 Procedure for reference model with damage behaviour

6.5.1 Step 1: non-damage stage

The procedure starts with non-damage stage for the reference model. A global weak formulation over the tensor product space, which is here $\overline{\mathcal{U}}^h \otimes L^2(\mathcal{P})$. It reads:

$$\text{Find } \overline{u}^h \in \overline{\mathcal{U}}^h \otimes L^2(\mathcal{P}) \text{ such that } \overline{A}(\overline{u}^h, \overline{v}^h) = \overline{L}(\overline{v}^h) \quad \forall \overline{v}^h \in \overline{\mathcal{U}}^h \tag{6.25}$$

with:

$$\begin{aligned} \overline{A}(\overline{u}^h, \overline{v}^h) &= \int_{\mathcal{P}} \overline{a}_{\mathbf{p}}(\overline{u}^h, \overline{v}^h) \mathrm{d}\mathbf{p} = \int_{\mathcal{P}} \int_{\overline{\Omega}} (J_{\mathbf{p}} \mathbb{J}_{\mathbf{p}}^{-1} \mathbb{J}_{\mathbf{p}}^{-T}) \nabla_{\boldsymbol{\xi}} \overline{u}^h \cdot \nabla_{\boldsymbol{\xi}} \overline{v}^h \mathrm{d}\boldsymbol{\xi} \mathrm{d}\mathbf{p} \\ \overline{L}(\overline{v}^h) &= \int_{\mathcal{P}} \overline{\ell}_{\mathbf{p}}(\overline{v}^h) \mathrm{d}\mathbf{p} = \int_{\mathcal{P}} \left[\int_{\overline{\Omega}} J_{\mathbf{p}} \overline{f}_d \overline{v}^h \mathrm{d}\boldsymbol{\xi} + \int_{\partial_q \overline{\Omega}} J_{\mathbf{p}}^S \overline{F}_d \overline{v}^h \mathrm{d}S_\xi \right] \mathrm{d}\mathbf{p} \end{aligned} \tag{6.26}$$

The PGD solution with non-damage is defined as:

$$\overline{u}^h(\boldsymbol{\xi}, \mathbf{p}) \approx \overline{u}^h_m(\boldsymbol{\xi}, \mathbf{p}) = \sum_{i=1}^{m} \overline{\psi}_i^h(\boldsymbol{\xi}) G_i(\mathbf{p}) \quad \text{with } \overline{\psi}_i^h \in \overline{\mathcal{U}}^h, G_i(\mathbf{p}) \in L^2(\mathcal{P}) \tag{6.27}$$

$m \in \mathbb{N}^*$ being the rank (or order) of the PGD approximation.

6.5.2 Step 2: Newton method

After computing m PGD modes, we obtain the solution u_m for all values of parameters. One value of parameters corresponds to one geometry and one approaximate solution. Then, we can compute damage at all Gauss points in order to constitute a damage matrix for all values of parameters.

The damage at a gauss point can be obtained by the following formula:

$$Y = \frac{1}{2} Tr\left[\mathbb{K}_0 \varepsilon \varepsilon\right] \tag{6.28}$$

$$\beta = (Y_0 - Y_c)\alpha^2 \tag{6.29}$$

$\alpha = 0, d = 0 \quad at \quad t = 0$

$$\dot{d} = \left(\frac{k}{a}\right)\left(1 - e^{-a\left\langle \frac{Y - Y_0 - \beta}{Y_c - Y_0} \right\rangle_+}\right) \tag{6.30}$$

Damage can be then computed by $d = 0 + \dot{d} * t$.

Using SVD, the damage field can be separated as:

$$1 - damage = \sum_{1}^{SVD} da_\xi da_p \tag{6.31}$$

The geometry parameter problem with damage associated to (5.14) reads:

$$\overline{A_d}(\overline{\psi}^h G, \overline{\psi}^h \delta G) = \overline{L}(\overline{\psi}^h \delta G) - \overline{A_d}(\sum_{i=1}^{m-1} \overline{\psi}_i^h G_i, \overline{\psi}^h \delta G) \quad \forall \delta G \in L^2(\mathcal{P}) \tag{6.32}$$

so that:

$$\begin{aligned} \int_{\mathcal{P}} \Bigg[\left(\int_{\overline{\Omega}} \mathbb{D}_{\mathbf{p}}^d \nabla_{\boldsymbol{\xi}} \overline{\psi}^h \cdot \nabla_{\boldsymbol{\xi}} \overline{\psi}^h \mathrm{d}\boldsymbol{\xi} \right) G + \sum_{i=1}^{m-1} \left(\int_{\overline{\Omega}} \mathbb{D}_{\mathbf{p}}^d \nabla_{\boldsymbol{\xi}} \overline{\psi}_i^h \cdot \nabla_{\boldsymbol{\xi}} \overline{\psi}^h \mathrm{d}\boldsymbol{\xi} \right) G_i \\ - \int_{\overline{\Omega}} J_{\mathbf{p}} \overline{f}_d \overline{\psi}^h \mathrm{d}\boldsymbol{\xi} - \int_{\partial_q \overline{\Omega}} J_{\mathbf{p}}^S \overline{F}_d \overline{\psi}^h \mathrm{d}S_\xi \Bigg] \delta G \mathrm{d}\mathbf{p} = 0 \quad \forall \delta G \in L^2(\mathcal{P}) \end{aligned} \tag{6.33}$$

Similarly, the problem in space with damage associated to (5.15) reads:

$$\overline{A_d}(\overline{\psi}^h G, \delta\overline{\psi}^h G) = \overline{L}(\delta\overline{\psi}^h G) - \overline{A_d}(\sum_{i=1}^{m-1} \overline{\psi}_i^h G_i, \delta\overline{\psi}^h G) \quad \forall \delta\overline{\psi}^h \in \overline{\mathcal{U}}^h \tag{6.34}$$

$$\begin{aligned} \int_{\overline{\Omega}} \left[\left(\int_{\mathcal{P}} \mathbb{D}_{\mathbf{p}}^d G^2 \mathrm{d}\mathbf{p} \right) \nabla_{\boldsymbol{\xi}} \overline{\psi}^h \cdot \nabla_{\boldsymbol{\xi}} \delta\overline{\psi}^h + \sum_{i=1}^{m-1} \left(\int_{\mathcal{P}} \mathbb{D}_{\mathbf{p}} G_i G \mathrm{d}\mathbf{p} \right) \nabla_{\boldsymbol{\xi}} \overline{\psi}_i^h \cdot \nabla_{\boldsymbol{\xi}} \delta\overline{\psi}^h \right] \mathrm{d}\boldsymbol{\xi} \\ - \int_{\overline{\Omega}} \left(\int_{\mathcal{P}} J_{\mathbf{p}} G \mathrm{d}\mathbf{p} \right) \overline{f}_d \delta\overline{\psi}^h \mathrm{d}\boldsymbol{\xi} - \int_{\partial_q \overline{\Omega}} \left(\int_{\mathcal{P}} J_{\mathbf{p}}^S G \mathrm{d}\mathbf{p} \right) \overline{F}_d \delta\overline{\psi}^h \mathrm{d}S_\xi = 0 \quad \forall \delta\overline{\psi}^h \in \overline{\mathcal{U}}^h \end{aligned} \tag{6.35}$$

Solving space and parameter problems with damage over the fixed point method, we can acquire the damage solution $\overline{u}_m^d(\boldsymbol{\xi}, \mathbf{p})$. With the new solution $\overline{u}_m^d(\boldsymbol{\xi}, \mathbf{p})$, the Newton method compute iteratively the new damage field until reaching the iteration tolerance.

$$tolerance = \frac{\overline{u}_m^{d,n+1}(\boldsymbol{\xi}, \mathbf{p}) - \overline{u}_m^{d,n}(\boldsymbol{\xi}, \mathbf{p})}{\overline{u}_m^{d,n}(\boldsymbol{\xi}, \mathbf{p})} \tag{6.36}$$

6.5.3 Example : nonlinear problem on a plate with circular hole using PGD

Results of step 1

We now consider an elasticity problem over a plate with a hole at the center, and submitted to a biaxial traction loading (Figure 6.1). The material is supposed to be linear and isotropic, and the plane stress assumption is made. Due to symmetry conditions,

only a quarter of the plate is studied. We assume that the hole radius R is a geometry parameter, with $R \in [1, 2]$. After representing the geometry with NURBS functions, a change in the radius R is directly interpreted as a change in the coordinates of control points, and the IGA mesh is automatically adapted (see Figure 6.5).

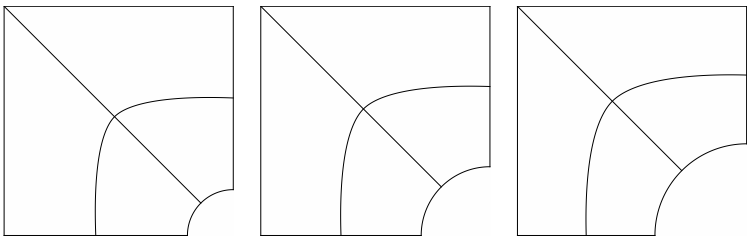

Figure 6.5: Configuration of the initial coarse IGA mesh for different values of R.

The elasticity problem with evolving geometry is again solved using PGD. The first three PGD modes in space and in geometry parameters are displayed in Figure 6.6 and Figure 6.7, respectively. The PGD solution evaluated for $R \in \{1, 1.5, 2\}$ is also shown in Figure 6.8.

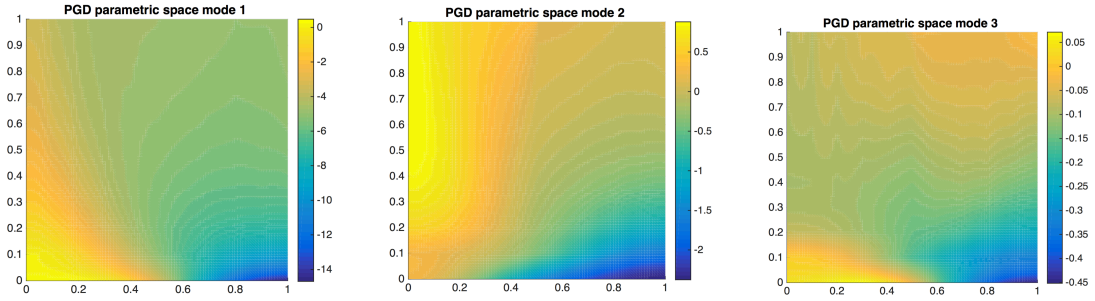

Figure 6.6: First three PGD modes in space (from left to right) in the IGA parametric space $\overline{\Omega}$.

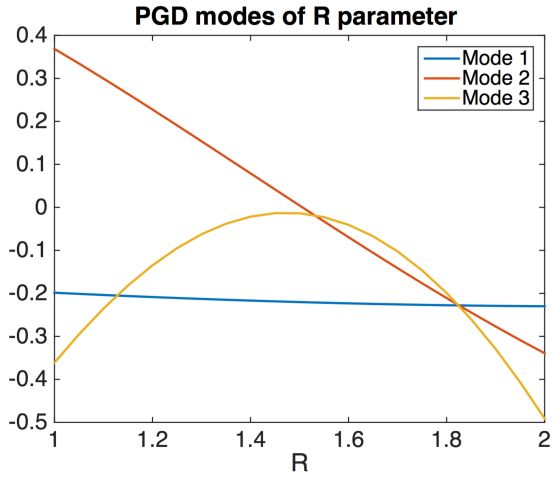

Figure 6.7: First three PGD modes in parameter R.

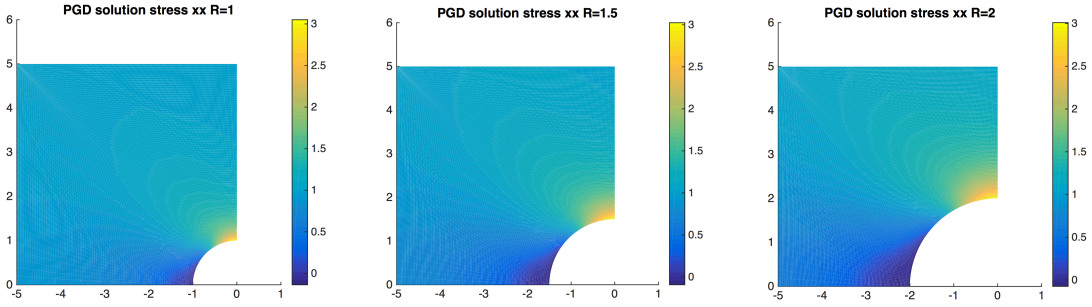

Figure 6.8: Approximate 3-mode PGD solution for various values of R.

Results of step 2

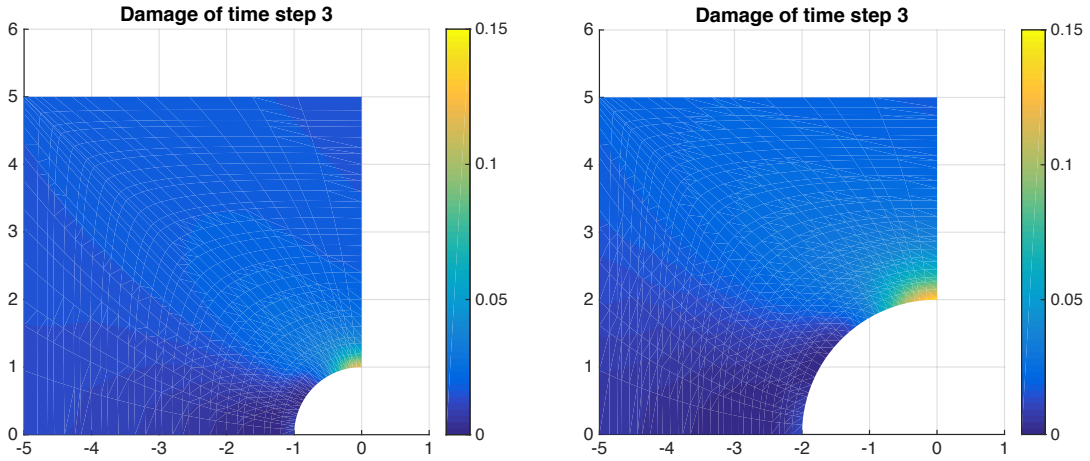

Figure 6.9: Damage field obtain from PGD with various radius values.

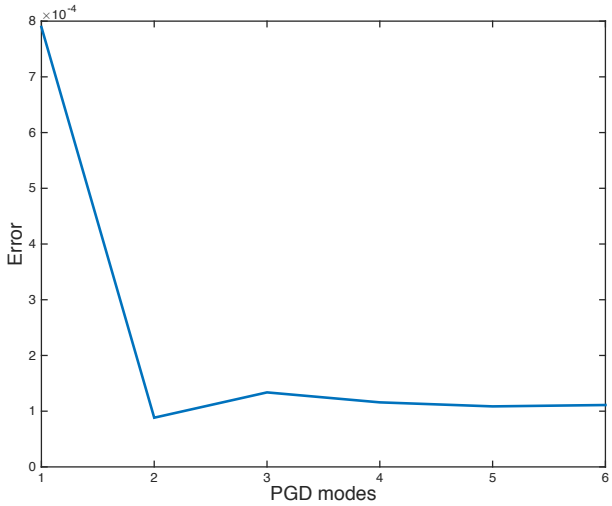

Figure 6.10: PGD error for damage problem.

These results, even though preliminary, confirm that proposed CRE and PGD tools can be extended to IGA-based solution of nonlinear problems.

Chapter 7

Conclusions and prospects

Contents

7.1 General conclusions 135
7.2 Prospects 136

7.1 General conclusions

This research work investigated for the first time the use of theCRE method in the IGA framework; an advantage of the method is that it applies for a wide range of problems from linear to non-linear states. Considering first linear problems, the CRE method was based on the construction of admissible fields using a prolongation condition as in FEA. Due to this condition, the principal issue dealt with the larger spans of IGA basis functions compared to FEA. A new procedure was proposed to solve the resulting larger systems. Numerical examples showed that the method can efficiently detect local errors for adaptive purposes. Also, effectivity indices proved that CRE is a robust tool for reliable error estimation. Furthermore, it was shown that after operating local refinement of an initial IGA mesh, the CRE method could recover better estimates.

The second novelty of this work was coupling IGA and PGD model reduction for parametrized geometries and shape optimization. From a shape optimization point of view, IGA is indeed a natural tool of choice due to its ability to represent complex shapes. The IGA geometry is controlled by few design variables and its tight connection between analysis and geometry models, so that the accurate geometry is maintained throughout the optimization. The key paradigm for the coupling between IGA and PGD was separating design variables with space variables in the IGA framework. SVD

and HOSVD were used as the tool for separating these variables. Numerical examples with one and two geometry parameters were solved with a few PGD modes. The CRE method was also applied in this context in order to identify major sources of error in order to save computation cost and certify the solution accuracy.

The third novelty of this thesis was the extension of error estimation and PGD for IGA in nonlinear problems. From the thermo-dynamical formulation of nonlinear behaviors, a general CRE was derived from residuals on the state equations and the evolution laws. Numerical examples only considered isotropic damage. Due to the more accurate stress field in IGA, the results showed the great potential of IGA in solving isotropic damage. When applying PGD for parametrized geometry with isotropic damage, the damage was considered as the new extra coordinate, and results showed the convergence to the reference solution with a couple of modes.

7.2 Prospects

We think the coupling between IGA, PGD, and CRE tools is a valuable approach, making scientific advances in the field, and which paves the way for further studies. Following this research work, several studies listed above could be pursued in the future:

- The application to nonlinear problems could be studied in more details, focusing in particular on quantities of interest (goal-oriented strategy);
- For all numerical examples, a homemade Matlab code was employed to simulate the IGA problems and introduce CRE and PGD tools. In order to run more complex problems, a future work could deal with the implementation of the proposed tools into existing commercial FE software such as Abaqus or Samcef. For that purpose, we believe that the Bezier extraction (linking IGA and FEA) is an interesting option, and it would be fruitful to investigate how CRE and PGD can be coupled with this framework;
- Also, all considered problems in this work consisted of one IGA patch. A future work would consist in applying to multiple IGA patches which have the ability to present a complex geometry with several circles. Let us mention that for matching multiple patches with non-crossing boundaries, it is necessary to use the Lagrange multiplier method;
- In the IGA-PGD method, separating design variables with space variables using SVD is not suitable when considering problems with a large number of geometry parameters. To adapt IGA-PGD to this context, a new strategy is required.

Furthermore, IGA generates new control points from a few initial control points with a simple formula. This means that it may be possible to obtain directly the separation function of the Jacobian matrix. Eventually, using PGD for a large number of parameters is still a research work in progress;

- The IGA-PGD tool allows one to obtain all approximate solutions of any geometry in a very efficient manner. Consequently, it seems to be a tool of choice for shape optimization. A further work would thus consist in the coupling with optimization algorithms, in order to evaluate cost functions and perform the whole shape optimization process;

- An interesting extension could deal with multiscale modeling with complex geometries. Such a modeling addresses the solution of problems which have important features at multiple scales of time and/or space. It includes p multiscale modeling of fluids, solids, and polymers, and the coupling with IGA-CRE and IGA-PGD may have potential industrial applications;

- Another field of extension is fluid–structure interaction, which is the interaction of some movable or deformable structures with an internal or surrounding fluid flow. The Newton–Raphson method or fixed-point iterations can be used to solve fluid–structure interaction problems without knowledge of the Jacobian matrix;

- Eventually, the proposed approach could be extended to topology optimization methods in which the requirement that the geometry be described explicitly by the domain boundary, with fixed topology, is removed. Instead, an implicit description using methods such as level sets or phase-fields is used.

Bibliography

[ACDH10] A. Ammar, F. Chinesta, P. Diez, and A. Huerta. An error estimator for separated representations of highly multidimensional models. *Computer Methods in Applied Mechanics and Engineering*, 199(25):1872–1880, May 2010.

[ACH+12] F. Auricchio, F. Calabrò, T. J. R. Hughes, A. Reali, and G. Sangalli. A simple algorithm for obtaining nearly optimal quadrature rules for NURBS-based isogeometric analysis. *Computer Methods in Applied Mechanics and Engineering*, 249-252:15–27, December 2012.

[ACL18] P-E. Allier, L. Chamoin, and P. Ladevèze. Towards simplified and optimized a posteriori error estimation using PGD reduced models. *International Journal for Numerical Methods in Engineering*, 113(6):967–998, February 2018.

[AD97] O. Allix and J.-F. Deü. Delayed-Damage Modelling for Fracture Prediction of Laminated Composites under Dynamic Loading. *Engineering Transactions*, 45(1):29–46, 1997.

[AG19] V. Agrawal and S.S. Gautam. Varying-order NURBS discretization: An accurate and efficient method for isogeometric analysis of large deformation contact problems. *CoRR*, abs/1903.05859, 2019.

[AGZ+15] I. Alfaro, D. González, S. Zlotnik, P. Díez, E. Cueto, and F. Chinesta. An error estimator for real-time simulators based on model order reduction. *Advanced Modeling and Simulation in Engineering Sciences*, 2(1):30, November 2015.

[AHC+14] A. Ammar, A. Huerta, F. Chinesta, E. Cueto, and A. Leygue. Parametric solutions involving geometry: A step towards efficient shape optimization. *Computer Methods in Applied Mechanics and Engineering*, 268:178–193, January 2014.

[Alm13] J. P. M. Almeida. A basis for bounding the errors of proper generalised decomposition solutions in solid mechanics. *International Journal for Numerical Methods in Engineering*, 94(10):961–984, June 2013.

[AM17] J. P. M. Almeida and E. a. W. Maunder. Equilibrium Finite Element Formulations, 2017.

[AMCK06] A. Ammar, B. Mokdad, F. Chinesta, and R. Keunings. A new family of solvers for some classes of multidimensional partial differential equations encountered in kinetic theory modeling of complex fluids. *Journal of Non-Newtonian Fluid Mechanics*, 139(3):153–176, December 2006.

[AND+10] A. Ammar, M. Normandin, F. Daim, D. Gonzalez, E. Cueto, and F. Chinesta. Non-Incremental Strategies Based on Separated Representations : Applications in Computational Rheology. *Communications in Mathematical Sciences*, 8(3):671–695, 2010.

[AO93] M. Ainsworth and J.T. Oden. A unified approach to a posteriori error estimation using element residual methods. *Numerische Mathematik*, 65(1):23–50, December 1993.

[AO97] M. Ainsworth and J.T. Oden. A posteriori error estimation in finite element analysis. *Computer Methods in Applied Mechanics and Engineering*, 142(1):1–88, March 1997.

[BBDVC+06] Y. Bazilevs, L. Beirão Da Veiga, J. A. Cottrell, T. J. R. Hughes, and G. Sangalli. Isogeometric analysis: Approximation, stability and error estimates for h-refined meshes. *Mathematical Models and Methods in Applied Sciences*, 16(07):1031–1090, July 2006.

[BBHH10] D. J. Benson, Y. Bazilevs, M. C. Hsu, and T. J. R. Hughes. Isogeometric shell analysis: The Reissner–Mindlin shell. *Computer Methods in Applied Mechanics and Engineering*, 199(5):276–289, January 2010.

[BBHH11] D. J. Benson, Y. Bazilevs, M. C. Hsu, and T. J. R. Hughes. A large deformation, rotation-free, isogeometric shell. *Computer Methods in Applied Mechanics and Engineering*, 200(13):1367–1378, March 2011.

[BCHZ08] Y. Bazilevs, V. M. Calo, T. J. R. Hughes, and Y. Zhang. Isogeometric fluid-structure interaction: theory, algorithms, and computations. *Computational Mechanics*, 43(1):3–37, December 2008.

[BdVBL+12] L. Beirão da Veiga, A. Buffa, C. Lovadina, M. Martinelli, and G. Sangalli. An isogeometric method for the Reissner–Mindlin plate bending problem. *Computer Methods in Applied Mechanics and Engineering*, 209-212:45–53, February 2012.

[BdVBRS11] L. Beirão da Veiga, A. Buffa, J. Rivas, and G. Sangalli. Some estimates for h–p–k-refinement in Isogeometric Analysis. *Numerische Mathematik*, 118(2):271–305, June 2011.

[BEC15] R. Bouclier, T. Elguedj, and A. Combescure. An isogeometric locking-free NURBS-based solid-shell element for geometrically nonlinear analysis. *International Journal for Numerical Methods in Engineering*, 101(10):774–808, March 2015.

[BHB+13] D. J. Benson, S. Hartmann, Y. Bazilevs, M. C. Hsu, and T. J. R. Hughes. Blended isogeometric shells. *Computer Methods in Applied Mechanics and Engineering*, 255:133–146, March 2013.

[Boy08] S. Boyaval. Reduced-Basis Approach for Homogenization beyond the Periodic Setting. *Multiscale Modeling & Simulation*, 7(1):466–494, January 2008.

[BPS09] D. Braess, V. Pillwein, and J. Schöberl. Equilibrated residual error estimates are p-robust. *Computer Methods in Applied Mechanics and Engineering*, 198(13):1189–1197, March 2009.

[BR01] R. Becker and R. Rannacher. An optimal control approach to a posteriori error estimation in finite element methods. *Acta Numerica*, 10:1–102, May 2001.

[BS93] R. Bank and R. Smith. A Posteriori Error Estimates Based on Hierarchical Bases. *SIAM Journal on Numerical Analysis*, 30(4):921–935, August 1993.

[BS01] I. Babuska and T. Strouboulis. *The Finite Element Method and its Reliability*. Numerical Mathematics and Scientific Computation. Oxford University Press, Oxford, New York, August 2001.

[BSEH11] M.J. Borden, M. A. Scott, J.A. Evans, and T.J.R. Hughes. Isogeometric finite element data structures based on Bézier extraction of NURBS. *International Journal for Numerical Methods in Engineering*, 87(1-5):15–47, 2011.

[BSU+94] I. Babuška, T. Strouboulis, C. S. Upadhyay, S. K. Gangaraj, and K. Copps. Validation of a posteriori error estimators by numerical approach. *International Journal for Numerical Methods in Engineering*, 37(7):1073–1123, January 1994.

[BSV10] A. Buffa, G. Sangalli, and R. Vázquez. Isogeometric analysis in electromagnetics: B-splines approximation. *Computer Methods in Applied Mechanics and Engineering*, 199(17):1143–1152, March 2010.

[CAC10] F. Chinesta, A. Ammar, and E. Cueto. Recent Advances and New Challenges in the Use of the Proper Generalized Decomposition for Solving Multidimensional Models. *Archives of Computational Methods in Engineering*, 17(4):327–350, 2010.

[Can07] T. Canuto, C.and Kozubek. A fictitious domain approach to the numerical solution of PDEs in stochastic domains. *Numerische Mathematik*, 107(2):257, May 2007.

[CDH09] R. Cottereau, P. Díez, and A. Huerta. Strict error bounds for linear solid mechanics problems using a subdomain-based flux-free method. *Computational Mechanics*, 44(4):533–547, September 2009.

[CEG15] A. Chemin, T. Elguedj, and A. Gravouil. Isogeometric local h-refinement strategy based on multigrids. *Finite Elements in Analysis and Design*, 100:77–90, August 2015.

[CF99] C. Carstensen and S. Funken. Fully Reliable Localized Error Control in the FEM. *SIAM Journal on Scientific Computing*, 21(4):1465–1484, January 1999.

[CHB09] J. A Cottrell, T. J. R. Hughes, and Y Bazilevs. Isogeometric Analysis: Toward Integration of CAD and FEA. *Wiley.com*, 2009.

[CHRW17] F. Chinesta, A. Huerta, G. Rozza, and K. Willcox. Model Reduction Methods. In *Encyclopedia of Computational Mechanics Second Edition*, pages 1–36. American Cancer Society, 2017.

[CKL14] F. Chinesta, R. Keunings, and A. Leygue. *The Proper Generalized Decomposition for Advanced Numerical Simulations: A Primer*. SpringerBriefs in Applied Sciences and Technology. Springer International Publishing, 2014.

[CL07] L. Chamoin and P. Ladevèze. Bounds on history-dependent or independent local quantities in viscoelasticity problems solved by approximate methods. *International Journal for Numerical Methods in Engineering*, 71(12):1387–1411, September 2007.

[CL08] L. Chamoin and P. Ladevèze. A non-intrusive method for the calculation of strict and efficient bounds of calculated outputs of interest in linear viscoelasticity problems. *Computer Methods in Applied Mechanics and Engineering*, 197(9):994–1014, February 2008.

[CL12] L. Chamoin and P. Ladevèze. Robust control of PGD-based numerical simulations. *European Journal of Computational Mechanics*, 21(3-6):195–207, December 2012.

[CL14] Francisco Chinesta and Pierre Ladevèze, editors. *Separated Representations and PGD-Based Model Reduction: Fundamentals and Applications*. CISM International Centre for Mechanical Sciences. Springer-Verlag, Wien, 2014.

[CLB+13] F. Chinesta, A. Leygue, F. Bordeu, J. V. Aguado, E. Cueto, D. Gonzalez, I. Alfaro, A. Ammar, and A. Huerta. PGD-Based Computational Vademecum for Efficient Design, Optimization and Control. *Archives of Computational Methods in Engineering*, 20(1):31–59, March 2013.

[CLC11] F. Chinesta, P. Ladevèze, and E. Cueto. A Short Review in Model Order Reduction Based on Proper Generalized Decomposition. *Archives of Computational Methods in Engineering*, 18(4):395–404, 2011.

[CNLB16] A. Courard, D. Néron, P. Ladevèze, and L. Ballere. Integration of PGD-virtual charts into an engineering design process. *Computational Mechanics*, 57(4):637–651, April 2016.

[CNS13] M. Chevreuil, A. Nouy, and E. Safatly. A multiscale method with patch for the solution of stochastic partial differential equations with localized uncertainties. *Computer Methods in Applied Mechanics and Engineering*, 255:255–274, March 2013.

[CPAL17] L. Chamoin, F. Pled, P-E Allier, and P. Ladevèze. A posteriori error estimation and adaptive strategy for PGD model reduction applied to parametrized linear parabolic problems. *Computer Methods in Applied Mechanics and Engineering*, 327:118–146, December 2017.

[CRBH06] J. A. Cottrell, A. Reali, Y. Bazilevs, and T. J. R. Hughes. Isogeometric analysis of structural vibrations. *Computer Methods in Applied Mechanics and Engineering*, 195(41):5257–5296, August 2006.

[DB01] C. De Boor. *A Practical Guide to Splines*. Springer-Verlag, New York, 2001.

[DCV+16] L. Dalcin, N. Collier, P. Vignal, A. M. A. Côrtes, and V. M. Calo. PetIGA: A framework for high-performance isogeometric analysis. *Computer Methods in Applied Mechanics and Engineering*, 308:151–181, August 2016.

[DJS10] M.R. Dörfel, B. Jüttler, and B. Simeon. Adaptive isogeometric analysis by local h-refinement with T-splines. *Computer Methods in Applied Mechanics and Engineering*, 199(5):264–275, January 2010.

[DKYB15] X. Deng, A. Korobenko, J. Yan, and Y. Bazilevs. Isogeometric analysis of continuum damage in rotation-free composite shells. *Computer Methods in Applied Mechanics and Engineering*, 284:349–372, February 2015.

[DLWZ12] L. De Lorenzis, P. Wriggers, and G. Zavarise. A mortar formulation for 3d large deformation contact using NURBS-based isogeometric analysis and the augmented Lagrangian method. *Computational Mechanics*, 49(1):1–20, January 2012.

[DM99] P. Destuynder and B. Métivet. Explicit Error Bounds in a Conforming Finite Element Method. *Mathematics of Computation*, 68(228):1379–1396, 1999.

[EBBH09] J. A. Evans, Y. Bazilevs, I. Babuška, and T.J.R. Hughes. n-Widths, sup–infs, and optimality ratios for the k-version of the isogeometric finite

element method. *Computer Methods in Applied Mechanics and Engineering*, 198(21):1726–1741, May 2009.

[EBCH08] T. Elguedj, Y. Bazilevs, V. M. Calo, and T.J.R. Hughes. B-bar and F-bar projection methods for nearly incompressible linear and non-linear elasticity and plasticity using higher-order NURBS elements. *Computer Methods in Applied Mechanics and Engineering*, 197(33-40):2732–2762, February 2008.

[EOB13] R. Echter, B. Oesterle, and M. Bischoff. A hierarchic family of isogeometric shell finite elements. *Computer Methods in Applied Mechanics and Engineering*, 254:170–180, February 2013.

[EV10] A. Ern and M. Vohralík. A Posteriori Error Estimation Based on Potential and Flux Reconstruction for the Heat Equation. *SIAM Journal on Numerical Analysis*, 48(1):198–223, January 2010.

[FSV15] D. Fußeder, B. Simeon, and A. V. Vuong. Fundamental aspects of shape optimization in the context of isogeometric analysis. *Computer Methods in Applied Mechanics and Engineering*, 286:313–331, April 2015.

[Gal09] L. Gallimard. A constitutive relation error estimator based on traction-free recovery of the equilibrated stress. *International Journal for Numerical Methods in Engineering*, 78(4):460–482, April 2009.

[GCBH08] H. Gómez, V. M. Calo, Y. Bazilevs, and T.J.R. Hughes. Isogeometric analysis of the Cahn–Hilliard phase-field model. *Computer Methods in Applied Mechanics and Engineering*, 197(49):4333–4352, September 2008.

[GJS+12] D. Großmann, B. Jüttler, H. Schlusnus, J. Barner, and A.V Vuong. Isogeometric simulation of turbine blades for aircraft engines. *Computer Aided Geometric Design*, 29(7):519–531, October 2012.

[GNS83] P. Germain, Q. S. Nguyen, and P. Suquet. Continuum Thermodynamics. *Journal of Applied Mechanics*, 50(4b):1010–1020, December 1983.

[GS02] M.B. Giles and E. Süli. Adjoint methods for PDEs: a posteriori error analysis and postprocessing by duality. *Acta Numerica*, 11, January 2002.

[GYVL+18] J. Gu, T. Yu, L. Van Lich, T-T. Nguyen, and T-Q. Bui. Adaptive multi-patch isogeometric analysis based on locally refined B-splines. *Computer*

Methods in Applied Mechanics and Engineering, 339:704–738, September 2018.

[HCB05] T. J. R. Hughes, J. A. Cottrell, and Y. Bazilevs. Isogeometric analysis: CAD, finite elements, NURBS, exact geometry and mesh refinement. *Computer Methods in Applied Mechanics and Engineering*, 194(39):4135–4195, October 2005.

[HM03] J. Haslinger and R. Mäkinen. *Introduction to shape optimization. Theory, approximation, and computation.* 01 2003.

[HN75] B. Halphen and Q. Nguyen. Sur les Matériaux Standard Généralisés. *Journal de Mécanique*, 14:39–63, January 1975.

[HRS10] T. J. R. Hughes, A. Reali, and G. Sangalli. Efficient quadrature for NURBS-based isogeometric analysis. *Computer Methods in Applied Mechanics and Engineering*, 199(5):301–313, January 2010.

[HRVB15] S. Hosseini, J.J. C. Remmers, C.V. Verhoosel, and R. Borst. Propagation of delamination in composite materials with isogeometric continuum shell elements. *International Journal for Numerical Methods in Engineering*, 102(3-4):159–179, April 2015.

[JKK] K. A. Johannessen, M. Kumar, and year = 2015 file = Full Text PDF:/Users/phuong/Zotero/storage/5V33BDDK/Johannessen et al. - 2015 - Divergence-conforming discretization for Stokes pr.pdf:application/pdf;Snapshot:/Users/phuong/Zotero/storage/B9B4QWRL/2498413.htm Kvamsdal, T. Divergence-conforming discretization for Stokes problem on locally refined meshes using LR B-splines. *38-70*.

[KBLW09] J. Kiendl, K. U. Bletzinger, J. Linhard, and R. Wüchner. Isogeometric shell analysis with Kirchhoff–Love elements. *Computer Methods in Applied Mechanics and Engineering*, 198(49):3902–3914, November 2009.

[KFB98] P. Kagan, A. Fischer, and P.Z. Bar-Yoseph. New B-Spline Finite Element approach for geometrical design and mechanical analysis. *International Journal for Numerical Methods in Engineering*, 41(3):435–458, February 1998.

[KKJ17] M. Kumar, T. Kvamsdal, and K. A. Johannessen. Superconvergent patch recovery and a posteriori error estimation technique in adaptive isogeo-

metric analysis. *Computer Methods in Applied Mechanics and Engineering*, 316:1086–1156, April 2017.

[KNTDLH15] R. Kruse, N. Nguyen-Thanh, L. De Lorenzis, and T. J. R. Hughes. Isogeometric collocation for large deformation elasticity and frictional contact problems. *Computer Methods in Applied Mechanics and Engineering*, 296:73–112, November 2015.

[KT15] S.K. Kleiss and S.K. Tomar. Guaranteed and sharp a posteriori error estimates in isogeometric analysis. *Computers & Mathematics with Applications*, 70(3):167–190, August 2015.

[KVvdZvB14] G. Kuru, C. V. Verhoosel, K. G. van der Zee, and E. H. van Brummelen. Goal-adaptive Isogeometric Analysis with hierarchical splines. *Computer Methods in Applied Mechanics and Engineering*, 270:270–292, March 2014.

[Lad99] P. Ladevèze. *Nonlinear Computational Structural Mechanics: New Approaches and Non-Incremental Methods of Calculation*. Mechanical Engineering Series. Springer-Verlag, New York, 1999.

[Lad01] P. Ladevèze. Constitutive relation errors for F.E. analysis considering (visco-) plasticity and damage. *International Journal for Numerical Methods in Engineering*, 52(5-6):527–542, October 2001.

[Lad08] P. Ladevèze. Strict upper error bounds on computed outputs of interest in computational structural mechanics. *Computational Mechanics*, 42(2):271–286, July 2008.

[LC11] P. Ladevèze and L. Chamoin. On the verification of model reduction methods based on the proper generalized decomposition. *Computer Methods in Applied Mechanics and Engineering*, 200(23):2032–2047, June 2011.

[LC12] P. Ladevèze and L. Chamoin. Toward guaranteed PGD-reduced models. In G. Zavarise and D. P. Boso, editors, *Bytes and Science*. CIMNE, Barcelona, 2012.

[LC15] P. Ladevèze and L. Chamoin. The constitutive relation error method: A general verification tool. verifying calculations – forty years on an

overview of classical verification techniques for fem simulations. *Springer Briefs*, (13):59–94, 2015.

[LCF10] P. Ladevèze, L. Chamoin, and É. Florentin. A new non-intrusive technique for the construction of admissible stress fields in model verification. *Computer Methods in Applied Mechanics and Engineering*, 199(9):766–777, January 2010.

[LCLX10] Y. Liang, X. Cheng, Z. Li, and J. Xiang. Multi-objective robust airfoil optimization based on non-uniform rational B-spline (NURBS) representation. *Science China Technological Sciences*, 53(10):2708–2717, October 2010.

[LEB+10] S. Lipton, J. A. Evans, Y. Bazilevs, T. Elguedj, and T. J. R. Hughes. Robustness of isogeometric structural discretizations under severe mesh distortion. *Computer Methods in Applied Mechanics and Engineering*, 199(5):357–373, January 2010.

[LGTP01] J. Lepine, F. Guibault, J-Y. Trépanier, and F. Pepin. Optimized nonuniform rational b-spline geometrical representation for aerodynamic design of wings. *AIAA Journal*, 39:2033–2041, 01 2001.

[LL83] P. Ladevèze and D. Leguillon. Error Estimate Procedure in the Finite Element Method and Applications. *SIAM Journal on Numerical Analysis*, 20(3):485–509, June 1983.

[LM96] P. Ladevèze and E. A. W. Maunder. A general method for recovering equilibrating element tractions. *Computer Methods in Applied Mechanics and Engineering*, 137(2):111–151, October 1996.

[LM98] P. Ladevèze and N. Moës. A new a posteriori error estimation for nonlinear time-dependent finite element analysis. *Computer Methods in Applied Mechanics and Engineering*, 157(1):45–68, April 1998.

[LMD99] P. Ladevèze, N. Moës, and B. Douchin. Constitutive relation error estimators for (visco)plastic finite element analysis with softening. *Computer Methods in Applied Mechanics and Engineering*, 176(1):247–264, July 1999.

[LP05] P. Ladevèze and J. P. Pelle. *Mastering Calculations in Linear and Nonlinear Mechanics*. Mechanical Engineering Series. Springer-Verlag, New York, 2005.

[LP10] P. Ladevèze and D. Passieux, J-C.and Néron. The LATIN multiscale computational method and the Proper Generalized Decomposition. *Computer Methods in Applied Mechanics and Engineering*, 199(21-22):1287–1296, April 2010.

[LQ11] K. Li and X. Qian. Isogeometric analysis and shape optimization via boundary integral. *Computer-Aided Design*, 43(11):1427–1437, November 2011.

[LR97] P. Ladevèze and Ph. Rougeot. New advances on a posteriori error on constitutive relation in f.e. analysis. *Computer Methods in Applied Mechanics and Engineering*, 150(1):239–249, December 1997.

[LR10] T. Lassila and G. Rozza. Parametric free-form shape design with PDE models and reduced basis method. *Computer Methods in Applied Mechanics and Engineering*, 199(23):1583–1592, April 2010.

[LT03] E. Laporte and P. L. Tallec. *Numerical Methods in Sensitivity Analysis and Shape Optimization*. Modeling and Simulation in Science, Engineering and Technology. Birkhäuser Basel, 2003.

[LV10] A. Leygue and E. Verron. A First Step Towards the Use of Proper General Decomposition Method for Structural Optimization. *Archives of Computational Methods in Engineering*, 17(4):465–472, December 2010.

[LWH14] L-D. Lorenzis, P. Wriggers, and T.J. R. Hughes. Isogeometric contact: a review. *GAMM-Mitteilungen*, 37(1):85–123, 2014.

[LWW+17] S. Li, Z. Wu, D. Wang, W. Zhang, and J. Trevelyan. An isogeometric boundary element reanalysis framework based on proper generalized decomposition. In *2017 8th International Conference on Mechanical and Aerospace Engineering (ICMAE)*, pages 272–280, July 2017.

[MMP00] L. Machiels, Y. Maday, and A.T. Patera. A "flux-free" nodal Neumann subproblem approach to output bounds for partial differential equations. *Comptes Rendus de l'Académie des Sciences - Series I - Mathematics*, 330(3):249–254, February 2000.

[MQR12] A. Manzoni, A. Quarteroni, and G. Rozza. Shape optimization for viscous flows by reduced basis methods and free-form deformation. *International Journal for Numerical Methods in Fluids*, 70(5):646–670, October 2012.

[MSH15] A. Manzoni, F. Salmoiraghi, and L. Heltai. Reduced Basis Isogeometric Methods (RB-IGA) for the real-time simulation of potential flows about parametrized NACA airfoils. 2015.

[NABR15] V. P. Nguyen, C. Anitescu, S. P. A. Bordas, and T. Rabczuk. Isogeometric analysis: An overview and computer implementation aspects. *Mathematics and Computers in Simulation*, 117:89–116, November 2015.

[NCS11] A. Nouy, M. Chevreuil, and E. Safatly. Fictitious domain method and separated representations for the solution of boundary value problems on uncertain parameterized domains. *Computer Methods in Applied Mechanics and Engineering*, 200(45-46):3066–3082, 2011.

[Ngu08] N. C. Nguyen. A multiscale reduced-basis method for parametrized elliptic partial differential equations with multiple scales. *Journal of Computational Physics*, 227(23):9807–9822, December 2008.

[Nou10] A. Nouy. A priori model reduction through Proper Generalized Decomposition for solving time-dependent partial differential equations. *Computer Methods in Applied Mechanics and Engineering*, 199(23):1603–1626, April 2010.

[NP18] A. Nouy and F. Pled. A multiscale method for semi-linear elliptic equations with localized uncertainties and non-linearities. *ESAIM: Mathematical Modelling and Numerical Analysis*, April 2018.

[NXHN14] H. Nguyen-Xuan, T. Hoang, and V. P. Nguyen. An isogeometric analysis for elliptic homogenization problems. *Computers & Mathematics with Applications*, 67(9):1722–1741, May 2014.

[OFJ+06] J.T. Oden, J. Fish, C. Johnson, A. Laub, D Srolovitz, T. Belytschko, T.J.R. Hughes, D. Keyes, and L. Petzold. *Simulation-based engineering science*. 01 2006.

[PCA10] E. Pruliere, F. Chinesta, and A. Ammar. On the deterministic solution of multidimensional parametric models using the Proper Generalized De-

composition. *Mathematics and Computers in Simulation*, 81(4):791–810, December 2010.

[PCL11] F. Pled, L. Chamoin, and P. Ladevèze. On the techniques for constructing admissible stress fields in model verification: Performances on engineering examples. *International Journal for Numerical Methods in Engineering*, 88(5):409–441, November 2011.

[PDH06] N. Parés, P. Díez, and A. Huerta. Subdomain-based flux-free a posteriori error estimators. *Computer Methods in Applied Mechanics and Engineering*, 195(4):297–323, January 2006.

[PO99] S. Prudhomme and J. T. Oden. On goal-oriented error estimation for elliptic problems: application to the control of pointwise errors. *Computer Methods in Applied Mechanics and Engineering*, 176(1):313–331, July 1999.

[PP97] M. Paraschivoiu and A.T. Peraire, J.and Patera. A posteriori finite element bounds for linear-functional outputs of elliptic partial differential equations. *Computer Methods in Applied Mechanics and Engineering*, 150(1):289–312, December 1997.

[PS47] W. Prager and J. L. Synge. Approximation in elasticity based on the concept of function space. *Quarterly of Applied Mathematics*, 5(3):241–269, 1947.

[PT95] L. Piegl and W. Tiller. *The NURBS Book*. Monographs in Visual Communication. Springer-Verlag, Berlin Heidelberg, 1995.

[RGR14] V. Rey, P. Gosselet, and C. Rey. Study of the strong prolongation equation for the construction of statically admissible stress fields: Implementation and optimization. *Computer Methods in Applied Mechanics and Engineering*, 268:82–104, January 2014.

[Roz11] G. Rozza. Reduced Basis Approximation and Error Bounds for Potential Flows in Parametrized Geometries. *Communications in Computational Physics*, 9(1):1–48, January 2011.

[SBTR12] R. N. Simpson, S. P. A. Bordas, J. Trevelyan, and T. Rabczuk. A two-dimensional Isogeometric Boundary Element Method for elastostatic

analysis. *Computer Methods in Applied Mechanics and Engineering*, 209-212:87–100, February 2012.

[SDS+12] D. Schillinger, L. Dedè, M.A. Scott, J.A. Evans, M.J. Borden, E. Rank, and T.J.R. Hughes. An isogeometric design-through-analysis methodology based on adaptive hierarchical refinement of NURBS, immersed boundary methods, and T-spline CAD surfaces. *Computer Methods in Applied Mechanics and Engineering*, 249-252:116–150, December 2012.

[SFH11] R. Sevilla, S. Fernández-Méndez, and A. Huerta. 3d NURBS-enhanced finite element method (NEFEM). *International Journal for Numerical Methods in Engineering*, 88(2):103–125, October 2011.

[SK07] A. Sobester and A.J. Keane. Airfoil design via cubic splines - Ferguson's curves revisited. pages 1–15, May 2007.

[SKY10] Y-D. Seo, H-J. Kim, and S-K. Youn. Shape optimization and its extension to topological design based on isogeometric analysis. *International Journal of Solids and Structures*, 47(11):1618 – 1640, 2010.

[SSE+13] M. A. Scott, R. N. Simpson, J. A. Evans, S. Lipton, S. P. A. Bordas, T. J. R. Hughes, and T. W. Sederberg. Isogeometric boundary element analysis using unstructured T-splines. *Computer Methods in Applied Mechanics and Engineering*, 254:197 – 221, 2013.

[SZD17] M. Signorini, S. Zlotnik, and P. Díez. Proper generalized decomposition solution of the parameterized Helmholtz problem: application to inverse geophysical problems. *International Journal for Numerical Methods in Engineering*, 109(8):1085–1102, February 2017.

[TCHM18] H.P. Thai, L. Chamoin, and C. Ha Minh. Robust a posteriori error estimation in isogeometric analysis using the concept of constitutive relation error. *Computer Methods in Applied Mechanics and Engineering,submitted*, 2018.

[TWH11] İ. Temizer, P. Wriggers, and T. J. R. Hughes. Contact treatment in isogeometric analysis with NURBS. *Computer Methods in Applied Mechanics and Engineering*, 200(9):1100–1112, February 2011.

[Ver94] R Verfürth. A review of a posteriori error estimation adaptive mesh-refinement techniques. *Journal of Computational and Applied Mathematics*, 50:67–83, 05 1994.

[VGJS11] A. V. Vuong, C. Giannelli, B. Jüttler, and B. Simeon. A hierarchical approach to adaptive local refinement in isogeometric analysis. *Computer Methods in Applied Mechanics and Engineering*, 200(49):3554–3567, December 2011.

[WC12] J. Waeytens and P. Chamoin, L.and Ladevéze. Guaranteed error bounds on pointwise quantities of interest for transient viscodynamics problems. *Computational Mechanics*, 49(3):291–307, March 2012.

[WCLZ16] L. Wang, L. Chamoin, P. Ladevèze, and H. Zhong. Computable upper and lower bounds on eigenfrequencies. *Computer Methods in Applied Mechanics and Engineering*, 302:27–43, April 2016.

[WFC08] W.A. Wall, M.A. Frenzel, and C. Cyron. Isogeometric structural shape optimization. *Computer Methods in Applied Mechanics and Engineering*, 197(33):2976–2988, June 2008.

[WXWQ18] C. Wang, S. Xia, X. Wang, and X. Qian. Isogeometric shape optimization on triangulations. *Computer Methods in Applied Mechanics and Engineering*, 331:585–622, April 2018.

[XMDG11] G. Xu, B. Mourrain, R. Duvigneau, and A. Galligo. Parametrization of computational domain in isogeometric analysis: methods and comparison. *Computer Methods in Applied Mechanics and Engineering*, 200(23-24):2021–2031, April 2011.

[XMDG12] G. Xu, B. Mourrain, R. Duvigneau, and A. Galligo. A New Error Assessment Method in Isogeometric Analysis of 2d Heat Conduction Problems. *Advanced Science Letters*, 10(1):508–512, May 2012.

[ZCDA18] X. Zou, M. Conti, P. Díez, and F. Auricchio. A nonintrusive proper generalized decomposition scheme with application in biomechanics. *International Journal for Numerical Methods in Engineering*, 113(2):230–251, January 2018.

[ZDMH15] S. Zlotnik, P. Díez, D. Modesto, and A. Huerta. Proper generalized decomposition of a geometrically parametrized heat problem with geo-

physical applications. *International Journal for Numerical Methods in Engineering*, 103(10):737–758, September 2015.

[ZDQ17] S. Zhu, L. Dedè, and A. Quarteroni. Isogeometric analysis and proper orthogonal decomposition for the acoustic wave equation. *ESAIM: Mathematical Modelling and Numerical Analysis*, 51(4):1197–1221, July 2017.

[Zie01] O. C. Zienkiewicz. Displacement and equilibrium models in the finite element method by B. Fraeijs de Veubeke, Chapter 9, Pages 145–197 of Stress Analysis, Edited by O. C. Zienkiewicz and G. S. Holister, Published by John Wiley & Sons, 1965. *International Journal for Numerical Methods in Engineering*, 52(3):287–342, September 2001.